UNIVERSIDADE DE SÃO PAULO
INSTITUTO DE FÍSICA DE SÃO CARLOS

Florent André Julien Cottier

Light-atom interaction: mean-field approach and intensity fluctuations

São Carlos

2018

Florent André Julien Cottier

Light-atom interaction: mean-field approach and intensity fluctuations

Thesis presented to the Graduate Program in Physics at the Instituto de Física de São Carlos, Universidade de São Paulo and The Institut de Physique de Nice, Université Côte d'Azur, France, to obtain the double degree of Doctor in Science.

Concentration area: Theoretical Physics

Advisor: Dr. Romain Bachelard
Advisor: Dr. Robin Kaiser

Corrected version
(Original version available on the Program Unit)

São Carlos
2018

Cottier, Florent Andre Julien
Light-atom interaction: mean-field approach and intensity fluctuations / Florent Andre Julien Cottier; advisor Romain Pierre Bachelard - revised version -- São Carlos 2018.
147 p.

Thesis (Doctorate - Graduate Program in Física Básica) -- Instituto de Física de São Carlos, Universidade de São Paulo - Brasil Institut de Physique de Nice, 2018.

1. Cold atoms. 2. Cooperative effects. 3. Super-and subradiance. 4. Anderson localization. I. Bachelard, Romain Pierre, advisor. II. Title.

Florent André Julien Cottier

Interaction lumière-atomes : approche de champ moyen et fluctuations d'intensité

Thèse présentée au Programme Doctoral de l'Instituto de Física de São Carlos, Universidade de São Paulo et de l'Institut de Physique de Nice, Université Côte d'Azur, France, pour obtenir le double diplôme de Docteur en Sciences.

Discipline Physique Théorique

Directeur de Thèse : Dr. Romain Bachelard
Directeur de Thèse : Dr. Robin Kaiser

Version Corrigée

(Version original disponible sur le programme de l'unité)

São Carlos

2018

Cottier, Florent André Julien
Interaction lumière-atomes: approache de champ moyen et fluctuations d´intensité / Florent André Julien Cottier; advisor Romain Bachelard; Robin Kaiser - revised version -- SÃ£o Carlos/Nice, France 2018.
147 p.

Thesis (Doctorate with double degree - Graduate Program in Física Básica) -- Instituto de Física de São Carlos, Universidade de São Paulo - Brasil and L´Institute de Physique de Nice - Nice, France, 2018.

1. Atomes froids. 2. Effets coopératifs. 3. Super-et sousradiance. 4. Localisation d´Anderson. I. Bachelard, Romain, II. Kaiser, Robin, advisor. III. Title.

To the enriched personalities I met.

ACKNOWLEDGEMENTS

I would like to thank my two advisers; it has been a real pleasure to work with you. Dr. Romain Bachelard welcomed me in São Carlos and was an example of integration for me as a foreigner. I have learnt from him much more than only science. I will not forget the time he has spent on my cotutelle project. I spent the second part of my project in Sophia Antipolis, France, working with Dr. Robin Kaiser, head of the most stimulating research group I have worked with. His passion for science was communicative and all those discussions we had about physics are the reason I enjoyed so much doing science. I want to thank both of you for making this cotutelle thesis much more than a research project.

I am grateful to Nathalie Hamel, Isabelle Larochette, the EDSFA, USPSC's administration, Robin Kaiser and Romain Bachelard for their work to make my cotutelle possible. I also want to thanks the informatics service of USPSC.

I started my project in São Carlos, Brazil, three years ago without knowing a word of Portuguese. It started with my first, but not last, churrasco at Dr. Philippe Courteille and Marilde Courteille's place.
I am sincerely happy about the two years I spent in Brazil mainly thanks to all the diverse peoples I have been in contact with. The first people I met when I arrived are particularly important to me as this experience in Brazil is intrinsically related to them: Dalila, Michal and Diego. One coffee break in front of USP will not be enough to say everything. She trained me to hug, he was a fellow traveller and he never stopped laughing. To complete the group, this experience was worth nothing but meeting Claudia. Later on, Hans naturally joined us and it had been a pleasure to welcome you in Rennes. There is a list of people that I want to mention: Isotilia with your unexpected stories, Dave for founding the hiking group and visiting me in Antibes, Marios for the rooftop churrascos, Manuela for the running races, the Colombian football team, the mathematician's team that I wish I would have met you earlier, Carlos, my officemates, Mariane that welcomed us in Campo Grande and much more.

I spent the second part of my thesis in the institute INPHYNI in Sophia Antipolis. I want to thank all the members of this institute, researchers, students, administrative, as it has been a real pleasure to work in such a stimulating and friendly environment. First, I want to thank, the experimentalist Aurélien, Patricia, Ana, Michelle and William I had enriching discussions with. Those exchanges were important to me and brought another dimension to my project. Then I want to thank the postdoctoral and PhD students with whom I enjoyed our long discussions about physics as much as those unexpected moments, Antonin for you good mood, the squash team Aurélien, Patrice and Jean (also for the

table tennis games), Ana for this nice collaboration, Marius for those matlab running breaks and for your help, Axel, Vittorio, Juan and Anis.

Finally, I want to thank my parents for crossing the Atlantic and visiting me in Brazil and Kevin for our trips in South America.

Do not ask yourself a question you are not ready to answer yet.

ABSTRACT

COTTIER, F. **Light-atom interaction: mean-field approach and intensity fluctuations**. 2018. 147p. Thesis (Doctor in Science) - Instituto de Física de São Carlos, Universidade de São Paulo, São Carlos, 2018.

In this thesis, we investigate the coherent scattering of light propagating in a random medium. We are interested in phenomena like the super- and subradiance and Anderson localization that are related to waves interferences and spatial disorder. However, the fundamental difference between subradiance and Anderson localization still needs to be clarified. This thesis gives new elements for the understanding of these phenomena and we present a new method to observe Anderson localization. A mean-field model that does not contain disorder is developed, and we show that super- and subradiance do not require disorder whereas Anderson localization does. In this theoretical work, the coupling between the light and many atoms is reduced to a coupling matrix between the atoms by tracing over the degrees of freedom of the light, which results in a linear problem for the atomic dipoles. The study of the eigenvalues and eigenmodes of this matrix then allows to determine the super- and subradiant modes, and to probe the Anderson localization phase transition with a scaling analysis. Furthermore, the link to the experiment is realized by showing that the intensity fluctuations present an increase at the localization transition. The system is studied in the steady-state regime when the medium is continuously charged by a laser until reaches a stationary regime, and the decay dynamics, when the laser is switched off, so the cloud releases the energy stored. Finally, we present a preliminary work that shows that the diagonal disorder might be a good strategy to reach Anderson localization.

Keywords: Cold atoms. Cooperative effects. Super- and subradiance. Anderson localization.

RESUMO

COTTIER, F. **Interação luz-átomo: abordagem de campo médio e flutuações de intensidade**. 2018. 147p. (Doutorado em Ciências) - Instituto de Física de São Carlos, Universidade de São Paulo, São Carlos, 2018.

Nesta tese, investigamos o espalhamento coerente de luz propagando em um meio aleatório. Estamos interessados em fenômenos como superradiância, subradiância e localização de Anderson, os quais estão relacionados com interferências de ondas e desordem espacial. No entanto, as diferenças fundamentais entre subradiância e localização de Anderson ainda precisam ser esclarecidas. Esta tese traz novos elementos na compreensão destes fenômenos e apresentamos um novo método para observar a localização de Anderson. Neste trabalho teórico, estudamos os autovalores e os automodos de uma matriz de acoplamento que permite extrair modos super- e subradiantes, e exibem uma transição de fase de localização de Anderson através de uma análise de escalamento. Além disso, a conexão com o experimento é feita através da intensidade irradiada pela nuvem em todas as direções. Distinguimos dois casos: o regime de estado estacionário, quando o meio é continuamente excitado por um laser e alcança um regime estacionário; e o caso dinâmico, onde o laser é desligado e a nuvem libera a energia armazenada. Desenvolvemos um modelo de campo médio que não inclui desordem, e mostramos que super- e subradiância não precisam da desordem para existir, ao contrário da localização de Anderson. Mostramos também que podemos observar uma transição de fase de localização de Anderson na estatística da intensidade. Finalmente, apresentamos um trabalho preliminar que mostra que a desordem diagonal pode ser uma boa estratégia para alcançar a localização de Anderson.

Palavras-chaves: Átomos frios. Efeitos cooperativos. Super- e subradiância. Localização de Anderson.

RÉSUMÉ

COTTIER, F. **Interaction lumière-atomes : approche du champ moyen et fluctuations d'intensité**. 2018. 147p. (Docteur en Sciences) - Instituto de Física de São Carlos, Universidade de São Paulo, São Carlos, 2018.

Dans cette thèse, nous étudions la diffusion cohérente de la lumière se propageant dans un milieu désordonné. Nous nous intéressons à des phénomènes tels que la super- et sousradiance et la localisation d'Anderson qui sont liées aux interférences et au désordre spatial. Cependant, la différence fondamentale entre la sousradiance et la localisation d'Anderson doit encore être clarifiée. Cette thèse donne de nouvelles idées pour la compréhension de ces phénomènes et nous présentons une nouvelle méthode pour observer la localisation d'Anderson. On développe un modèle à champ moyen qui ne contient pas de désordre, et nous montrons que super- et sousradiance ne nécessitent pas de désordre contrairement à la localisation d'Anderson. Dans ce travail théorique, le couplage entre la lumière et les atomes est réduit à une matrice de couplage entre les atomes en calculant la trace sur les degrés de liberté de la lumière, ce qui nous amène à un problème linéaire pour les dipôles atomiques. L'étude des valeurs propres et des modes propres de cette matrice permet de déterminer des modes super- et sousradiant, et de sonder la transition de phase de localisation avec une *scaling analysis*. De plus, le lien avec l'expérience est fait en montrant que les fluctuations de l'intensité augmentent à travers la transition de localisation. Le système est étudié en régime stationnaire, quand le milieu est continûment chargé par un laser et que celui-ci atteint l'équilibre, et en dynamique, quand le laser est éteint et que le milieu se décharge de l'énergie stockée. Enfin, nous présentons un travail préliminaire qui montre que le désordre diagonal peut être une bonne stratégie pour atteindre la localisation d'Anderson.

Keywords : Atomes froids. Effets coopératifs. Super- et sousradiance. Localisation d'Anderson.

LIST OF FIGURES

LIST OF SYMBOLS

ω_a	Atom transition frequency.
λ_a	Atom wavelength.
Γ	Atom transition linewidth.
N	Number of atoms.
$\rho\lambda^3$	Normalized atomic density.
$\mathbf{r}_j$	Position of atom j.
ω	Laser frequency.
W_0	Waist of the Gaussian laser.
$\mathbf{k}$	Laser wavevector.
Δ	Detuning between the atomic transition and the laser frequency.
δ	Detuning.
Ω	Rabi-frequency.
σ_{sc}	Cross section.
l_{sc}	Mean free path.
σ_{sc}	Cross section.
σ_0	Resonant cross section.
R	Radius of the spherical atomic cloud.
L	Side length of the spherical atomic cloud.
b	Optical thickness.
b_0	Resonant optical thickness.
$\beta_j(t)$	Atomic dipole function of atom j.
D	Coupled matrix.
λ_n	Coupled matrix eigenvalues.
γ_n	Real part of the eigenvalues of the coupled matrix.

ω_n	Imaginary part of the eigenvalues of the coupled matrix.
G	Green function.
h	Spatial grid step.
H	Number of grid steps.
$j_n(r)$	First kind of Bessel function.
$h_n(r)$	Hankel function.
PR_n	Participation ratio of mode n.
σ_n^2	Size of mode n.
$I(t)$	Intensity radiated in a given direction when the laser is switched off at $t = 0$.
Γ_N	Superradiant decay rate.
τ_{sub}	Subradiant slope.
g	Thouless number, dimensionless number or conductance.
Γ	Atom transition linewidth.
σ_{sc}	Cross section.
$P(I)$	PDF of variable I.
$\langle I \rangle$	Mean of variable I.
$\tilde{I} = I/\langle I \rangle$	Normalized intensity.
$var(\tilde{I}) = \sigma_{\tilde{I}}^2$	variance of variable $\tilde{I}$.
r, θ, ϕ	Spherical coordinates.
r_o	Distance of computation of the intensity.
$g^{(2)}(0)$	Autocorrelation function.
W	Diagonal disorder or strength of the diagonal disorder.

CONTENTS

Part I

General introduction

The light-matter interaction and the propagation of light in a disordered medium is an active topic of research but also manifests in everyday life. Technical progresses such as the invention of the laser[1,2] and theoretical advances on the wave behaviour of the light and the understanding of interferences allowed for a broad series of comparisons between theories and experiments.[3–6] Hence, a fundamental experiment that matches theoretical predictions validates the theory whereas a contradiction leads to more details theoretical work. So, the light-matter interaction is challenging experimentally as well as a theoretically. Indeed, depending on the characteristics of the wave (coherent or incoherent for instance) and the medium (density, disordered or ordered, linear or not, size of the scatterers ...), it gives rise to different physics. For instance, at a macroscopic level, a perfectly transparent and amorphous medium refract the light, and the medium can be described with a refractive index. The light propagates in straight line in the two mediums but the direction of propagation is modified at the interface with an angle depending on the refractive index. We can observe this effect when a pen is in the water or a monochromatic light going through a prism. Thus, the atomic details can be forgotten when studying such a phenomenon.

Yet in some cases, the disorder will play a predominant role. One way to describe the scattering of a particle in a random medium is to imagine a random walk. Hence, the number of scattering of a particle depends on the cross-section of the scatterers.[4] This simple approach already allows explaining many phenomena. For instance, the radiation trapping describes the trapping of a photon in the medium by an increase in the number of scattering while the optical thickness of the medium increases.[7,8] However, when the wave behaviour of the particle is involved, (i.e. wave-particle description of a photon), a more complete approach taking into account interferences is required. Indeed, in this thesis we are interested in interference phenomena that occur in the scattering of a coherent light in a disordered medium, for example, the light propagating in a glass of milk. The interest of cold atoms as a disordered medium is that we can work at resonance, i.e., with an optically thick medium where we are in the multiple scattering regime. Hence, cooperative effects are introduced between dipoles through the scattering of electromagnetic waves. Atoms behave collectively even though they are spatially separated. In the simple picture of a single atom, an electromagnetic wave propagating toward the atom can be re-emitted in another direction, from its original direction where the atom plays the role of the scatterer; it corresponds to a scattering event. In most of this thesis, we consider a scalar description of the light which means that the scattering by the atoms is isotropic, although the global emission diagram of the atomic cloud contains different physics depending on the direction of observation. Moreover, the scattering is elastic if there is no exchange of energy between the wave and the scatterer. Throughout this thesis, we consider a low-intensity pump in order to stay in the linear optical regime, so the scattering by the atoms is elastic, i.e., the wavelength of the light is unaltered during the scattering

process. For instance, the Rayleigh scattering is elastic and the wavelength is preserved. In addition, in this thesis, we stay in the regime where the size of the scatterers is much smaller than the incident wavelength, yet the size of the atomic cloud is much larger. Thus, if the microscopic disorder is neglected, the Mie theory[9] can apply. In this thesis, we are interested in phenomena directly linked to the spatial disorder like Anderson localization. Thus, we use a coupled-dipole model to describe the light-atom interaction as it considers the spatial position of all atoms.

The scattering of the light propagating in a cloud of two-level atoms contains a rich physics and initiated intense interactions between theory and experiment. Two theoretical results, the Dicke subradiance[10] and the Anderson localization,[11] lead to many experiments that searched for their experimental signatures. In order to explain those phenomena, it is important to consider the wave behaviour of the light, the coherence of the light and interferences. On the contrary, the radiative transfer equation (RTE),[4] that does not deal with phases, is a good model to describe the Beer-Lambert law,[12] the incoherent transmission and the radiation trapping but cannot explain localization and super- and subradiance. The RTE takes into account the direction of propagation of the intensity which is more general than a classic diffusion equation that considers the density distribution of the intensity. For those two last phenomena (the Dicke subradiance and the Anderson localization), it is essential to use a more complete theory like the coupled-dipole model that will be presented in Part.II and results from the direct derivation of Maxwell's equations.

If one considers a single excited atom, it will radiate its energy with a characteristic time of $1/\Gamma$ where Γ is the characteristic decay time. When one considers an ensemble of N atoms in a small volume, an accelerated decay rate appears that can be N^2 faster than for a single atom. Originally, superradiance was investigated for a system of N excited atoms in a system of characteristic size $L \ll \lambda$ and where interactions are neglected, yet assuming the system remains in a series of symmetric states.[10] It has been shown that in this case, the maximal decay rate of the system is N^2 times faster than for N independent atoms.[10,13–15] In this thesis, we explore a slightly different system. We consider only the last stage of the radiative decay *i.e.* when the system contains at most one photon (we consider it is weakly driven). Still in the $L \ll \lambda$ regime, the spontaneous decay is $\Gamma_N = N\Gamma$, if polarization effects are neglected.[13] However, we will focus on dilute clouds, with $L \gg \lambda$, for which the superradiant decay rate is[16,17]:

$$\Gamma_N \sim \frac{N}{(k_0 L)^2}\Gamma. \tag{1}$$

We remark that it is the decay rate for the case $L \ll \lambda$ with $(k_0 L)^2$ the number of accessible modes in a system of size L so, there are typically $N/(k_0 L)^2$ atoms per mode. We also notice that $N/(k_0 L)^2$ is the resonant optical thickness of the cloud, b_0. This parameter helps to quantify of the cooperative effects inside the cloud. It is computed by integrating

the atomic density in the direction of the laser's propagation inside the cloud times the resonant scattering cross section. The superradiance is interpreted as the synchronization of dipoles that radiate coherently, in opposition to the subradiance where dipoles have less homogeneous phase profile. Hence, an ensemble of N atoms can couple through the electromagnetic field which gives rise to cooperative effects.

Cooperative effects in an atomic cloud are responsible for the increase of the radiative decay rate. It is thus natural to study an opposite consequence that is the *trapping* of the light inside the medium. There are three kinds of trapping: radiation trapping (random walk), subradiance and Anderson localization (interferences). The radiation trapping is the most intuitive phenomena as it describes the increase of the number of scattering events inside the medium with the increase of the optical thickness of the cloud. The radiation transfer equation (RTE) does not include interferences, is a suitable model to explain it. The first of the two phenomena we are interested in this thesis is the subradiance, which can be explained by interferences like superradiance. The study of subradiance is more recent than the one of superradiance due to the experimental challenge it represents, detecting the late-time cloud decay and coupling to subradiant modes. However, the first measurement of subradiance for dilute clouds was recently achieved in Nice.[18] Moreover, in the search of Anderson localization the interest for subradiance is renewed as both phenomena have been associated. Indeed, the long lifetime decay of the energy charged into a cloud of atoms was thought to be a signature of localization of the light.[19] In Part.III, we show that they are not straightforwardly connected.

Another rich topic of research is the Anderson localization introduced in 1958 by P.W. Anderson.[11] It originally came with the study of the trapping of electrons in disordered potentials and it was later shown to be more generally a wave phenomenon. Hence, the localization of light became of interest and cold atoms are an interesting medium to experimentally look for it since there are no interactions between photons or the absorption is negligeable. In electronic transport, the transition between a conductor to an insulator is reached by increasing the strength of the disorder. In the case of localization of light by cold atoms, the incident wave is a low-intensity laser and the disordered medium is an atomic cloud with tunable density. The disorder has been historically associated with the density, so we expect that the transition between the two regimes appears at a given density threshold. This approach is used in Part.III and Part.IV. However, the original idea of P.W. Anderson[11] is to control the disorder with the strength of a random potential for each site of a lattice where electrons are initially located. If we apply this approach to our system, it refers to "diagonal" disorder. The disorder is not related to the positional distribution of the atoms any longer but to the randomness in the shift of resonant energy of each atom. This method for introducing and controlling the disorder is presented and investigated Part.V.

In this thesis, we consider the propagation of a laser in a cloud of two-level atoms and the scattering by every atom is elastic and isotropic. For one atom, the cross-section gives the probability of a wave to be scattered. For an ensemble of atoms, the density plays a role and the relevant parameter is the mean free path that is the inverse of the density times the cross-section and it gives the characteristic distance between two scattering events.

In Part.II of this thesis we address the question of the role of the disorder for super- and subradiance. We present a mean-field model that does not contain disorder and we compare it with the well-known coupled-dipole model that does. First, we present the two models. Then we perform a spectra analysis and we show the existence of super- and subradiant modes in the two models. Finally, we bring our attention to the radiated intensity and the super- and subradiant rates.

In Part.III, we investigate the difference between subradiance and localization through the prism of the disorder by performing a scaling analysis with the mean-field model. We show that the mean-field model does not exhibit Anderson localization (AL) phase transition even if it describes subradiance.

Part.IV and Part.V are dedicated to the search of Anderson localization of light in 3D. The Part.IV is about the density as a way to introduce disorder whereas the Part.V is dedicated to the diagonal disorder. In both of those parts, we investigate the AL phase transition with a detailed study of the statistics of the radiated intensity.

In Part.IV, we first look at the transmitted mean intensity both in the steady-state and dynamically to show that there is no clear evidence of localization in those observables. Then we look at the probability distribution function of the fluctuations of the radiated intensity in the localized and non-localized regime, to show that it can be used as a signature of the localization transition. We turn our attention on the variance of the normalized intensity and the conductance. Finally, we consider the vectorial behaviour of the light and we introduce a strong magnetic field.

Finally, Part.V is dedicated to the introduction of a diagonal disorder as a way to reach the localized regime as it was recently proposed.[20] We apply the same approach as in Part.IV. First, we look at how the spectrum is modified by the diagonal disorder. Then we investigate the transmission and the intensity fluctuations in the stationary regime. Finally, we study the fluctuations of the intensity in time.

Part II

Role of disorder for super- and subradiance

1 MODELING THE LIGHT-ATOM INTERACTION

The interaction between light and a disordered medium can be seen from two sides. Either we take the point of view of the wave which is scattered by the scatterers or we consider that the scatterers are coupled between each other through the light. The first approach leads to studying the wave equation in random media, as presented, for example, in chapter 2 of reference.[21] It is a quite complex study and few analytical solutions exist such as the Mie-scattering theory.[22,23] An important simplification is to use a mean-field approach that averages the field over the disorder as usually done for dielectrics. The interest of this approach is that the medium is described as a continuum, and in the homogeneous case analytical solutions can often be derived. We will develop such approach in Sec.1.2, in the context of subradiance. Another way to deal with the problem leads to scatterers coupled by light and so we have coupled equations for all the scatterers. It is the coupled-dipole model presented Sec.1.1. It focuses on the scatterers and it contains all the physics involved in the system like disorder, dipole-dipole interaction and it allows to compute diffusion and refraction that are wave phenomena. However, the numerical time resolution limits the number of coupled scatterers that can be considered ($\sim 10\,000$). The main interest in comparing those two models is that one contains disorder when the other one does not. Hence, this study will help us to understand the influence of the disorder in phenomenon like super- and subradiance and Anderson localization. Moreover, in this chapter (and in the full thesis) we use a scalar description of the light so polarization and long-range effects are not considered. Nevertheless, in the dilute regimes, when $k_0 r \gg 1$ (r is the distance between two scatterers), the electric field is dominated by its transverse contribution that scales with $1/r$ so the radiative contribution can be neglected as well as long-range interactions. In our work, we impose to stay in a regime where $k_0 r \gg 1$ even when we consider dense regimes.

In the first part of this thesis we investigate both models (coupled-dipole and mean-field models) in order to look for which phenomena are described by only one or both model with the prism of the disorder.

1.1 Microscopic model: Coupled-dipole model

The coupled-dipole model (CDM) was proposed several decades ago[24] and has been intensively used over the past ten years to study the interaction between light and atomic dipoles.[25,26] There has been a renewed interest in this model over the last years due to the increase in computational power available. With existing computation power, it can be reasonably used for up to 10 000 dipoles. Other models like the Radiation Trapping Equation (RTE) can be used to describe for example the radiation trapping, the coherent

and incoherent transmission or the reflection[27] because those are not due to interference effects. However, it cannot explain coherent backscattering (CBS)[6,28] which justifies the development of more complete tools. The CDM gives a microscopic description of the medium and highlights the cooperation of the dipoles as they interact through the vacuum modes as well as the disorder represented by the random position of the atoms and all interferences effects.

1.1.1 Single and two-level atom physics

The structure of a single two-level atom is presented in Fig.1. The atom transition

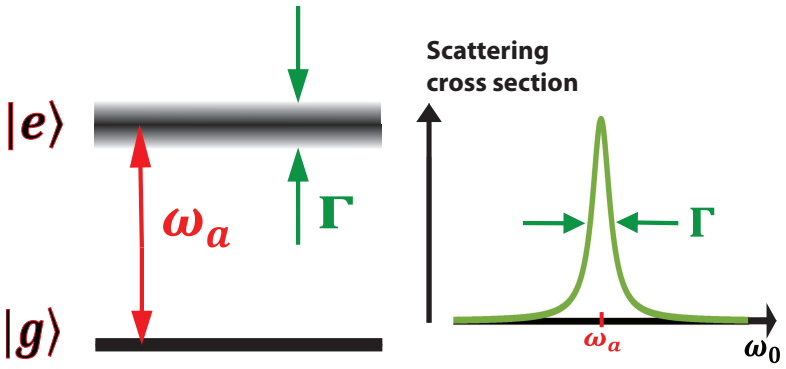

Figure 1 – Energy scheme of a two-level atom

Source: By the author

frequency is ω_a of wavelength λ_a, its linewidth is Γ which corresponds to the decay rate of the atom from the excited state and expresses the characteristic time for spontaneous emission. The scattering cross section follows a Lorentzian $\sigma_{sc} = \sigma_0/(1+4\delta^2)$ and gives the probability for the atom to be excited by an incident photon of frequency $\omega_0 = \omega_a + \Delta$, $\sigma_0 = \lambda^2/2\pi$ is the scattering cross section on resonance for scalar light and the photon detuning from the atomic transition is $\Delta = \delta\Gamma = \omega_0 - \omega_a$.

Let us now consider two identical atoms 1 and 2 with distance r_{12}. Solving (1.2), see Sec.1.1.3, it is easy to show that the associated eigenvalues are:

$$\lambda_{1,2} = (1 - 2\imath\delta) \pm \frac{e^{\imath k_0 r_{12}}}{\imath k_0 r_{12}}. \tag{1.1}$$

As we will show later, the real part of $\lambda_{1,2}$ is associated with the decay rate of the excited atom. The two-atom system is represented in Fig.2. From (1.1), two limit cases can be identified: first, if the atoms are far away from each other, $k_0 r_{ij} \gg 1$, they will behave as independent atoms with the same behaviour as in the previous paragraph as $\lambda_{1,2} \xrightarrow{k_0 r_{1,2} \to \infty} 1 - 2\imath\delta$. Then, if $k_0 r_{ij} < 2\pi$ each atom cannot be seen as isolated and they have to be described by one unique system of two modes. The strong correlations that develop between pairs of atoms closer than a wavelength will hereafter be referred as pair

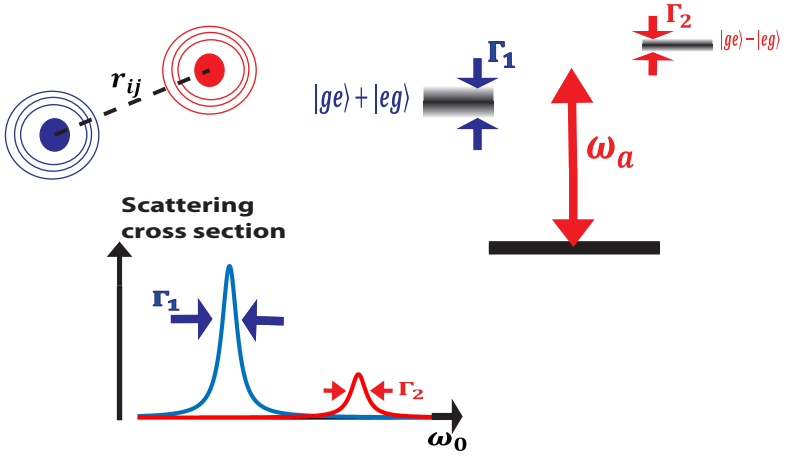

Figure 2 – Scheme for two identical atoms coupled by the dipole-dipole radiation

Source: By the author

physics, oppositely to the long-range effects that prevail for many atoms in a dilute cloud, which is the focus of this thesis. Eigenvalues are therefore $\lambda_{1,2} \sim 1/r$ when $k_0 r_{1,2} \to 0$. We can thus introduce the idea of super- and subradiance: $\Re(\Gamma_1) = 2 > \Gamma$ means that mode one will decay faster than one isolated atom, inversely to mode two ($\Re(\Gamma_2) = 0 < \Gamma$). They are respectively called superradiant and subradiant modes. It has been shown that superradiant mode results in an attractive potential between those pairs.[29,30] We now extend this interpretation for N fixed two-level atoms (dipoles). However, at large density, the probability to have two atoms satisfying $k_0 r_{ij} < 2\pi$ becomes non-negligible and pairs appear. It has been largely studied through the Euclidian non-hermitian random matrix theories[31–33] and their set of eigenvalues distribution in L. Bellando's thesis[25] and reference.[34] For most of the results presented in this thesis we discuss the impact of those pairs by introducing an exclusion volume.[35–38] Indeed, they contain interesting physics but they may hinder long-range effects as they introduce long-lived modes that are related to neither the many-scatterer subradiance nor the scattering of light.

1.1.2 Coupled-dipole equations

We study the interaction between a laser and a cloud of two-level cold atoms. This cloud is modeled as $N \gg 1$ point scatterers at fixed position $\mathbf{r}_j$, randomly distributed with an average density $\rho(\mathbf{r})$, transition linewidth Γ (also called single atom decay rate) and transition frequency ω_a. The pumping laser consists in a monochromatic plane wave $E_0 e^{i\mathbf{k}.\mathbf{r}}$ of wavevector $\mathbf{k} = k\hat{\mathbf{z}}$ ($k = \omega_0/c$), detuned from the atomic transition by $\Delta = \omega_0 - \omega_a$ (the normalized detuning is $\delta = \Delta/\Gamma$) and Rabi-frequency is $\Omega \ll \Gamma$.

We now introduce parameters that are relevant to describe the scattering regime. First, the scattering cross section is given by $\sigma_{sc} = \sigma_0/(1 + 4\delta^2)$ where $\sigma_0 = \lambda^2/\pi$ is the on-resonance cross section for scalar light. It can be seen as the *size* of the atom and it gives

the probability for the atom to be excited by a photon of frequency ω_a. Then, the mean free path is the characteristic distance between two scattering events $l_{sc} = 1/(\rho\sigma_{sc})$. The resonant optical thickness, b_0, is a cooperative effect parameter.[18,35,39] Whereas, the optical thickness $b(\delta)$ quantifies the multiple scattering. It is defined as $b(\delta) = b_0/(1+4\delta^2)$ where $b_0 = \int \rho(0,0,z)\sigma_0 \, dz$ is the on-resonance optical thickness. For instance, $b_0 = 6N/(k_0R)^2$ for a uniform sphere of radius R and with scalar light. b_0 depends on the geometry of the cloud and the interaction with the laser is done by the factor $1/(1+4\delta^2)$. These two last parameters are used to classify two regimes: the single scattering regime where photons cross the medium without interacting with the atoms (or at most once) so the medium is transparent and the multiple scattering regime where photons will scatter many times before escaping the medium. The first one takes place when $b(\delta) \ll 1$ which is equivalent to $l_{sc} > R$ and can be reached for a large detuning. In the other regime, $b(\delta) \gg 1$ which is equivalent to $l_{sc} \ll R$. It is important to remark that the single scattering regime, where the medium seems *transparent* in regards to the incoming photons, is not equivalent to N independent atoms as interference effects like super- and subradiance remain.[18,35,40] This remark is crucial to explain the difference between radiation trapping and subradiance. This will be discussed throughout this part.
Notions like the mean free path or the single and multiple scattering make sense for a random walk description of the propagation of a photon through a disordered medium. Indeed, the photon can be described by consecutive scattering events. However, to discuss phenomena like superradiance or subradiance, this image is not appropriate as the system is described by modes.

We stay in the low-intensity regime to avoid atoms saturation, which experimentally corresponds to the saturation parameter $s(\Delta) = \frac{I_0/I_{sat}}{1+4\delta^2} \ll 1$ (I_0 is the laser intensity and I_{sat} is the saturation intensity). Using the Markov approximation, the resonant dynamics of the atomic dipoles is given by a set of N coupled equations[24,41] for the atomic dipoles β_j:

$$\frac{d\beta_j}{dt} = \left(\imath\Delta - \frac{\Gamma}{2}\right)\beta_j - \frac{\imath\Omega}{2}e^{\imath\mathbf{k}.\mathbf{r}_j} - \frac{\Gamma}{2}\sum_{m\neq j}\frac{\exp(\imath k|\mathbf{r}_j - \mathbf{r}_m|)}{\imath k|\mathbf{r}_j - \mathbf{r}_m|}\beta_m. \tag{1.2}$$

The first right-hand term describes the single atom dynamics, with both spontaneous emission and oscillations due to the detuning, the second term corresponds to the laser and the last one to the radiation from all other atoms.
From the atomic dipole $\beta_i(t)$ we can extract the probability of atom i to be excited at time t by computing $|\beta_i(t)|^2$.

The derivation of (1.2) are presented and extensively discussed in[26,42] from Maxwell equations and from a quantum approach.

1.1.3 Solution of the CD equations

One way to solve (1.2) consists in finding eigenfunctions ψ_n and their related eigenvalues $-\frac{\Gamma}{2}\lambda_n$ of a matrix $-\frac{\Gamma}{2}D$ describing the dynamics of the system. The diagonal elements are $D_{i,j} = (1 - 2\imath\Delta/\Gamma)$ and off-diagonal ones are $D_{i\neq j} = \exp(\imath k|\mathbf{r}_i - \mathbf{r}_j|)/(\imath k|\mathbf{r}_i - \mathbf{r}_j|)$. Matrix D describes the dynamics of the system driven by (1.2). The last term of (1.2) which contains the off-diagonal terms $D_{i\neq j}$ gives rise to cooperative effects through the eigenmodes of the system. Eigenmode n (ψ_n), of matrix D has its p^{th} component denoted ψ_n^p, which thus is the contribution of atom p to mode n. We have changed the basis from the atoms basis to the modes basis. An eigenmode involves, in general, all the atoms, the contribution of each atom to mode n being given by $|\psi_n^p|^2$ so the modes are collective. Those modes are expressed as $\psi_n(t) = \psi_n(0)\exp(-\frac{\Gamma}{2}\lambda_n t)$, so their a probability to be excited decays as:

$$|\psi_n(t)|^2 = |\psi_n(0)|^2 \exp(-\Gamma\gamma_n t), \tag{1.3}$$

where we have defined $\lambda_n = \gamma_n + \imath\omega_n$. With this definition, γ_n and ω_n are respectively the decay rate and the energy shift of mode n.

We can discuss the notion of super- and subradiance from (1.3). We clearly see that if $\gamma_n < 1$, mode n will release his energy slower than one independent atom which is called a *subradiant mode*. On the other hand, if $\gamma_n > 1$, mode n will be called *superradiant*.

1.2 Continuous model: Mean-field approach

From a macroscopic point of view, where atomic details are neglected, a mean-field approach can be used to describe the propagation of light in a disordered medium. A mean-field approach had been introduced to simplify the description of many-body systems where all bodies interact between each other, which results in a set of N coupled equations as presented in the coupled-dipole model Sec.1.1. The interaction of $N-1$ bodies with the $N-th$ last one is replaced by a mean-field generated by all particles. Hence, the many-body system is replaced by a mean-field problem where the choice of the mean-field represents the main difficulty. The mean-field approach represents thus a continuous description of the dipole field.
A dielectric material is globally neutral but composed of positive and negatives particles. Differently from a conductor where charges flow through the material by applying an electric field, in a dielectric, electrons slightly shift from their average position, which breaks locally the charge neutrality and introduces an internal electric field that tends to reduce the overall field. Those fields can be derived from Maxwell equations what lead to the mean-field model that we show Sec.1.2.1.

The derivation presented in Sec.1.2.1 corresponds to a mean-field treatment of the cloud, which is in particular at the basis of the dielectric description of matter. Indeed

in the stationary regime, the dipole field can be shown to obey the Helmholtz equation, so techniques such as Mie scattering can be used to describe the scattering properties of the atomic sample.[9] The study of higher-order terms (in the stationary state) leads to corrections such as the Lorentz–Lorenz equation[43] but also effects related to quantum statistics for degenerate gases.[37,44]

1.2.1 Derivation of the continuous model

We model the N dipoles by N positive charges and negative charges (electron) gravitating around as it is done for dielectrics. This derivation is based on Maxwell's equations and the electric field whereas reference[45] focuses on dipoles. Let us start by deriving the well-known wave equation with an electric current from Maxwell-Ampère and Maxwell-Faraday equations:

$$\nabla \times \mathbf{E} = -\frac{\partial \mathbf{B}}{\partial t}, \qquad \nabla \times \mathbf{B} = \mu_0 \mathbf{j} + \mu_0 \epsilon_0 \frac{\partial \mathbf{E}}{\partial t}, \tag{1.4}$$

where ϵ_0 and μ_0 are respectively the vacuum permittivity and the vacuum permeability. $\mathbf{E}$ and $\mathbf{B}$ are the total electric respectively magnetic field. We note $c^2 = 1/(\epsilon_0 \mu_0)$ the square speed of light, $\mathbf{j}$ is the current density and ∇ the nabla operator. For a medium without free charges (a globally neutral medium), the Maxwell-Gauss equation gives $\nabla.\mathbf{E} = 0$. Using the identity $\nabla \times (\nabla \times \mathbf{E}) = \nabla \cdot (\nabla \cdot \mathbf{E}) - \Delta \mathbf{E}$ we find the wave equation:

$$\Delta \mathbf{E} - \frac{1}{c^2} \frac{\partial^2 \mathbf{E}}{\partial t^2} = \mu_0 \frac{\partial \mathbf{j}}{\partial t}. \tag{1.5}$$

For a discrete description of the medium with N fixed atoms, the electric current results from the sum of the displacement of all the electrons :

$$\mathbf{j}(t, \mathbf{r}) = -e \sum_{i=1}^{N} \frac{d\mathbf{r}_i(t)}{dt} \delta(\mathbf{r} - \mathbf{r}_i), \tag{1.6}$$

$\delta(\mathbf{r})$ is the Dirac function, $\mathbf{r}_i(t)$ is the position of the electron gravitating around atom i. This microscopic approach leads to the coupled-dipole equation and was discussed in the previous section Sec.1.1. The interest of the mean-field approach is to go from a microscopic to a macroscopic description of the medium. So, disorder is lost by replacing the sum over the N particles in (1.6) by a density distribution function of space $\rho(\mathbf{r})$ (independent of time). The current density is thus defined as:

$$\mathbf{j}(\mathbf{r}, t) = -e\rho(\mathbf{r}) \mathbf{v}_e(\mathbf{r}, t), \tag{1.7}$$

with $\mathbf{v}_e(\mathbf{r}, t) = \frac{\partial \mathbf{r}_e(\mathbf{r}, t)}{\partial t}$. The variable $\mathbf{r}_e(\mathbf{r}, t)$ is the displacement of electrons at position $\mathbf{r}$ from their equilibrium position. It results in the differential equation :

$$\frac{\partial^2 \mathbf{r}_e(\mathbf{r}, t)}{\partial t^2} + \omega_a^2 \mathbf{r}_e(\mathbf{r}, t) = -\frac{e}{m} \mathbf{E}(\mathbf{r}_e, t), \tag{1.8}$$

$\mathbf{E}(t, \mathbf{r})$ represents the total field, e the electric charge and m the electron mass. We suppose that all electrons oscillate in the same direction $\hat{\epsilon}$ that is the same direction than the electric field polarization. Moreover, we introduce the slowly-varying variables E and r_e on a time scale of $1/\omega_a$:

$$\mathbf{E}(\mathbf{r}, t) = E(\mathbf{r}, t)e^{-\imath\omega t}\hat{\epsilon}, \tag{1.9}$$

$$\mathbf{r}_e(\mathbf{r}, t) = r_e(\mathbf{r}, t)e^{-\imath\omega t}\hat{\epsilon}, \tag{1.10}$$

which turns (1.5) into:

$$\nabla^2 E + k^2 E = \mu_0 e\omega^2 \rho r_e, \tag{1.11}$$

with $\omega = kc$.
Equation (1.11) is a classic Helmholtz equation with second term and the solution is given in term of the Green function G as:

$$E(\mathbf{r}, t) = -\frac{\imath\mu_0 e\omega^3}{4\pi c}\int \rho(\mathbf{r}')G(\mathbf{r} - \mathbf{r}')r_e(\mathbf{r}', t) \quad d\mathbf{r}', \tag{1.12}$$

$G(\mathbf{r}) = \exp(\imath k|\mathbf{r}|)/(\imath k|\mathbf{r}|)$ is the Green's function.
Deriving (1.12) over time leads to:

$$\frac{E(\mathbf{r}, t)}{\partial t} = -\frac{\imath\mu_0 e\omega^3}{4\pi c}\int \rho(\mathbf{r}')G(\mathbf{r} - \mathbf{r}')\frac{r_e(\mathbf{r}', t)}{\partial t} \quad d\mathbf{r}'. \tag{1.13}$$

Moreover, injecting (1.9) and (1.10) in (1.8) gives a close equation and leads to:

$$\left(\omega^2 - \omega_a^2\right) r_e + 2\imath\omega\frac{\partial r_e}{\partial t} = \frac{e}{m}E. \tag{1.14}$$

We introduce the detuning $\Delta = \omega - \omega_a$ between the driving field and the electronic oscillator frequency and we assume $\Delta \ll \omega_a$. Combining (1.12), (1.13) and (1.14) leads to a self-consistent equation for the electric field[45]:

$$\frac{\partial E(\mathbf{r}, t)}{\partial t} = \imath\Delta E(\mathbf{r}, t) - \frac{\Gamma}{2}\int \rho(\mathbf{r}')G(\mathbf{r} - \mathbf{r}')E(\mathbf{r}', t) \quad d\mathbf{r}', \tag{1.15}$$

with $\Gamma = (\mu_0 e^2\omega_a^2)/(8\pi mc)$. In this semi-classical picture, Γ corresponds to a decay rate for the electric field and can be associated to the decay rate of an atomic transition as introduced in Sec.1.1.

In the linear optics regime the dipole β_j is directly proportional to the local electric field E_j, ($\beta_j = dE_j/\hbar(2\Delta + \imath\Gamma)$), with d the matrix dipole element of the transition, such that $\Omega = dE/\hbar$. Thus, (1.15) is the continuous version of (1.2) where the laser term is added by hand. In the other way round, (1.2) can be seen as the microscopic version of (1.15).
A more straightforward way to come out with (1.15) from the the coupled-dipole equation (1.2) is by replacing $\beta_j(t) \longrightarrow \beta(\mathbf{r}, t)$ and $\sum_j \longrightarrow \int \rho\, d\mathbf{r}$. Or, the other way around, we can go from (1.15) to (1.2) by replacing $\rho(\mathbf{r}) \longrightarrow \sum_{j=1}^{N} \delta(\mathbf{r} - \mathbf{r}_j)$ and $\beta_j \longrightarrow \beta(\mathbf{r}, t)$.

We also notice that the single-atom decay term is included in the integral term at the limit $\mathbf{r} \to \mathbf{r}'$ when we move to the microscopic description $\rho(\mathbf{r}) = \sum_{j=1}^{N} \delta(\mathbf{r} - \mathbf{r}_j)$ and with a proper definition of the Green function, see Sec.1.2.2. Nevertheless, the single atom physics is lost in the mean-field model as we have chosen a smooth density (field approach) rather than point scatterers.

1.2.2 Singularity

The green function is usually defined as $G(r) = \exp(\imath kr)/(\imath kr) = -\imath \cosh(kr) + \sinh(kr)$. From this expression we see that it diverges for $r \to 0$ as the imaginary part goes to the infinity, the real part converges to one. This singularity is related to the Lamb shift, and it can be addressed using renormalization techniques.[46] In the present work, it is put to zero, assuming the shift is already included in the transition frequency. All in all, the three-dimensional integral of G around the origin, for a smooth density ρ and field E, gives a finite contribution, so the divergence is purely local and does not require the introduction of any cut-off when performing numerical integrations. Hence, we use the following definition of the green function:

$$G(r) = \begin{cases} \exp(\imath kr)/(\imath kr) & \text{for } r > 0 \\ 1 & \text{for } r = 0 \end{cases} . \tag{1.16}$$

1.2.3 Analytic resolution

We start the analytical resolution of the mean-field equation (1.15), as far as possible before moving to numerics. First, we re-write the equation in term of atomic dipole $\beta(\mathbf{r}, t)$ and we introduce the laser term (plane wave):

$$\frac{\beta(\mathbf{r}, t)}{\partial t} = \imath \Delta \beta(\mathbf{r}, t) - \frac{\imath \Omega}{2} e^{\imath \mathbf{k}\cdot\mathbf{r}} - \frac{\Gamma}{2} \int \rho(\mathbf{r}') G(\mathbf{r} - \mathbf{r}') \beta(\mathbf{r}', t) \quad d\mathbf{r}'. \tag{1.17}$$

The scattering problem is particularly tractable for spherically symmetric systems,[22,23] and the spherical harmonics $Y_{n,m}$ appears as a natural basis for the angular dependence as the Green function is diagonal in that basis:

$$\begin{aligned} \frac{e^{ik|\mathbf{r}-\mathbf{r}'|}}{\imath k|\mathbf{r} - \mathbf{r}'|} &= 4\pi \sum_{n} \sum_{-n<s<n} Y_{n,s}(\theta, \phi) Y^*_{n,s}(\theta', \phi') \\ &\quad \times \begin{cases} j_n(kr') h_n(kr) & \text{for } r > r' \\ j_n(kr) h_n(kr') & \text{for } r \leq r', \end{cases} \end{aligned} \tag{1.18}$$

where j_n and h_n are respectively the spherical Bessel and Hankel functions, and where the polar angle is chosen with reference to the wavevector $\mathbf{k} = k\hat{\mathbf{z}}$. For simplicity, we focus on spherical symmetric cloud densities $\rho(r)$ to allow the projection on the $(n, m = 0)$ orders

only. Then we decompose the dipole field and the exponential as:

$$\beta(\mathbf{r},t) = \sum_{n,m} \beta_n(r,t) Y_{n,0}(\hat{\mathbf{r}}), \tag{1.19}$$

$$e^{i\mathbf{k}_0.\mathbf{r}} = \sqrt{4\pi} \sum_n \sqrt{2n+1} i^n j_n(kr) Y_{n,0}(\theta,\phi). \tag{1.20}$$

Injecting (1.18) into (1.17) and projecting the result on the $(n, m = 0)$ spherical harmonics provides the dynamical equations for β_n:

$$\begin{aligned} \frac{d\beta_n(r,t)}{dt} &= i\Delta\beta_n(r,t) - E_0\sqrt{4\pi}\sqrt{2n+1} i^n j_n(kr) \\ &\quad -2\pi\Gamma \int_0^R dr' \rho(r') \beta_n(r',t) \times \begin{cases} j_n(kr') h_n(kr) r'^2 & \text{for } r > r' \\ j_n(kr) h_n(kr') r'^2 & \text{for } r \leq r' \end{cases} . \end{aligned} \tag{1.21}$$

The $m \neq 0$ modes will not be populated by the plane wave as the latter does not break the rotational symmetry around the Oz axis. Nonetheless, these modes obey the same equation, so each eigenvalue of (1.21) will be degenerated $(2n+1)$ times. Note that in the microscopic case, no such projection is possible since the disorder breaks the rotational symmetry.

Since Equation (1.21) does not admit an analytic solution, we solve it numerically in Sec.1.2.4.

1.2.4 Numerical resolution

In the present section, we project the radial equation (1.21) on a grid to determine numerically the spectrum and dynamics associated to each spherical harmonics n. While the field (1.17) can be solved explicitly in the stationary regime[9] and gives rise to the Mie theory, the eigenvalues for the dynamical problem $\beta_n(r,t) = \exp(-\lambda t) f_n(r)$ are given by an implicit equation.[45] Furthermore, since it corresponds to eigenvalues for the functions $f : [0; R] \mapsto [0; R]$, the associated spectrum is infinite and continuous. Consequently, finding the eigenvalues by some root algorithm (based on Newton's method for example) will be inefficient as the eigenvalues found may not be representative of the overall spectrum.

To deal with this problem, we solve numerically the problem defined in (1.21) by discretizing the integration window. We define a spatial grid of step h and extension $[0 \;\; R]$ and we note $h = R/H$ where H is the number of integration step in the window $[0 \;\; R]$. However, in our study we focus on Gaussian atomic densities of root mean square σ_r, hence we hereafter use an integration range $R = 3\sigma_r$, i.e., thrice the cloud step radius. Taking this integration range ensures to take into account 95% of the density distribution of the cloud. h is a new free parameter.

This projection on a grid brings us back to a finite matrix, of size $H \times H = (R/h) \times (R/h)$. Indeed, $\forall n$, (1.21) can now be written as H coupled differential equations:

$$\frac{d\hat{\beta}_n(r,t)}{dt} = -\frac{\Gamma}{2}\left(D_c - 2\imath\delta\right)\hat{\beta}_n(r,t) + L, \tag{1.22}$$

where $\hat{\beta}_n(r,t) = [\beta_n(r_1 = 0, t) \cdots \beta_n(r_H = R, t)]$, D_c is the matrix defined below (1.23) and L represents the laser $L_j = E_0\sqrt{4\pi}\sqrt{2n+1}i^n j_n(kr_j)$, $(r_j = jh)$.

Equation (1.22) is solved by numerically diagonalizing the matrix $D = D_c - 2\imath\delta$ to obtain a set of eigenvalues λ_n^j, $j = [1 \dots H]$ for each mode n. The accuracy of this finite spectrum to represent the continuous spectrum is evaluated by decreasing the step h and observing its convergence. The smaller h is, the better the convergence, but the slower the computation. The value of h is chosen in order to optimize numerical speed calculation without significant loss of information in the spectrum.

Let us remind that the imaginary part of the diagonal term of D_c is put to 0 to avoid the divergence due to the interaction of the atom with itself which is discussed Sec.1.2.2.

The matrix describing the coupling dynamics for the mean-field approach for mode n reads:

$$D_c = 4\pi \left[h \begin{pmatrix} j_n^2(k_0h)\rho(h)h^2 & 0 & \cdots & 0 \\ j_n(k_0h)h_n(k_0(2h))\rho(h)h^2 & j_n^2(k_02h)\rho(2h)(2h)^2 & \cdots & 0 \\ \vdots & \vdots & \ddots & \vdots \\ j_n(k_0h)h_n(k_0R)\rho(h)h^2 & j_n(k_02h)h_n(k_0R)\rho(2h)(2h)^2 & \cdots & j_n^2(k_0R)\rho(R)R^2 \end{pmatrix} \right. \tag{1.23}$$

$$\left. + h \begin{pmatrix} 0 & j_n(k_0h)h_n(k_02h)\rho(2h)2h^2 & \cdots & j_n(k_0h)h_n(k_0R)\rho(R)R^2 \\ 0 & 0 & \cdots & j_n(k_02h)h_n(k_0R)\rho(R)R^2 \\ \vdots & \vdots & \ddots & \vdots \\ 0 & 0 & 0 & \end{pmatrix} \right]. \tag{1.24}$$

D_c is hence the equivalent of the matrix D introduced Sec.1.1.3 for the coupled-dipoles model. As well as we defined eigenvalues λ_n^j (same than the ones introduced Sec.1.1.3) we define the associated eigenvectors $\psi_n^j(t) = \psi_n^j(0)e^{-\frac{\Gamma}{2}\lambda_n^j t}$. Going back to the dipole space β from the eigenmodes space ψ, the dipole function $\hat{\beta}_n(r_j, t)$ of mode n at position r_j is a linear combination of exponentials $e^{-\frac{\Gamma}{2}\lambda_n^j t}$ as we have seen with the coupled-dipole model. The final solution has an infinite number of modes according to the condition $n \geq 0$, which raises a new question. Since we cannot numerically compute an infinite solution, how many modes n do we need to compute in order to capture the relevant physics? This question is discussed Sec.2.3.

1.3 Conclusion

We have introduced two models that describe the interaction between light and disordered medium in the low-intensity regime. One is a microscopic description of the

medium and contains the richest physics and the second one is a mean-field approach that does not contain disorder.

A fundamental difference between the microscopic and continuous approach is that the former possesses a finite spectrum, with N eigenvalues, whereas the latter has an infinite (continuous) spectrum, as the field is now represented as a continuous field. Indeed, eigenmodes are defined in Sec.1.1 for $j = [1 \cdots N]$ where N is the number of atoms considered whereas, in the mean-field model Sec.1.2, they are defined for $n \geq 0$, $j = [1 \cdots H]$ and $2n + 1$ times degenerated.

The mean-field approach will be, from now on, called *Continuous model*, *Mean-field model* or *MF model*. The coupled-dipole model will be called *Microscopic model*. They are both linear and can be studied through their eigenfunctions and eigenvalues. In this part we will compare those two models, first by looking at their spectra Chap.2.6 and secondly, by considering the radiated intensity Chap.3.4.

2 SPECTRA ANALYSIS

Since the scattering problem is a linear one, many of its properties can be deduced by studying the spectra using, for instance, a direct diagonalization of the coupling matrix introduced before when we have defined super- and subradiant modes and eigenvalues. In the following chapter, we compare the two models, continuous and microscopic, through their spectra to examine how the super- and subradiant modes and their eigenvalues behave in both models. Many results have already been shown using the CD model like the Anderson localization,[47–50] the coherent backscattering[3,6,28,51,52] (CBS),[53–59] the radiation trapping,[7,60–62] etc. We here compare the microscopic model with the continuous model to see if the second one contains the same kind of properties as the microscopic model keeping in mind that we are interested in super- and subradiance. We first look at the spectra in a complex plane to confirm that super- and subradiant modes are also present in the continuous model. Then we look at the influence of the integration step on the eigenvalue distribution. Finally, we compute the participation ratio and the variance in order to link the temporal description of a mode with its spatial representation.

2.1 Eigenvalues sum convergence

An important property is that the trace of the coupling matrix stays finite for the microscopic model, the trace of D is $\sum_{n=1}^{N} \lambda_n = N\,(1 - 2\imath\delta)$[16,17,45] with the definition of λ_n of (1.3). Hence, for a finite number of particles N the existence of superradiant values, $\Re(\lambda_n) > 1$, comes with the existence of subradiant ones, $\Re(\lambda_n) < 1$.

We now look at the same property for the continuous model whereas it has an infinite number of eigenvalues. Starting from (1.21) without the laser term, the trace is defined for $r = r'$ as:

$$\int \lambda_n(r)\, dr = i\Delta - \frac{\Gamma}{2} 4\pi \int_0^R j_n^2(k_0 r)\rho(r) r^2\, dr. \tag{2.1}$$

As the spectrum is infinite, the first term of (2.1) refers to the infinite sum of eigenvalues for mode n. We have not considered yet the degeneracy due to the spherical harmonics projection. We introduce the expression (2.2),[63]

$$\frac{x^2}{2}\left(\left[J_p(\alpha x)\right]^2 - J_{p-1}(\alpha x) J_{p+1}(\alpha x)\right) = \int x \left[J_p^2(\alpha x)\right]^2 dx, \tag{2.2}$$

in (2.1). For simplicity, we consider a uniform distribution $\rho(r) = \rho_0 = N/V$.

$$\begin{aligned}
\int \lambda_n(r)\, dr - \imath\Delta &= -\frac{\Gamma}{2} 4\pi \int_0^R j_n^2(k_0 r)\rho_0 r^2\, dr, && (2.3)\\
&= -\frac{\Gamma}{2} 4\pi \frac{\pi}{2k_0} \int_0^R J_{n+1/2}^2(k_0 r)\rho_0 r\, dr, && (2.4)\\
&= -\frac{\Gamma}{2} 4\pi \frac{\pi}{2k_0} \rho_0 \frac{R^2}{2} \left(\left[J_{n+1/2}(k_0 R)\right]^2 - J_{n-1/2}(k_0 R) J_{n+3/2}(k_0 R) \right) && (2.5)\\
&= -\frac{\Gamma}{2k_0} \pi^2 \rho_0 R^2 \left(\left[J_{n+1/2}(k_0 R)\right]^2 - J_{n-1/2}(k_0 R) J_{n+3/2}(k_0 R) \right). && (2.6)
\end{aligned}$$

We have hence replaced an integral with a finite sum. We now introduce the $2n+1$ degeneracy, sum over the $n \geq 0$ modes and use $\rho = N/(\frac{4}{3}\pi R^3)$:

$$\sum_{n\geq 0} \int \lambda_n(r)\, dr = -\frac{\Gamma}{2} \sum_{n\leq 0} (2n+1) \left\{ -2\imath\delta + N\frac{3}{2} \left([j_n(k_0 R)]^2 - J_{n-1}(k_0 R) J_{n+1}(k_0 R) \right) \right\} \quad (2.7)$$

The term $2n+1$ refers to the degeneracy of the eigenvalues. Indeed, for a fixed n, every mode (n, m), have the same eigenvalue λ_n for $-n \leq m \leq n$. We see that the imaginary part of the sum given by the $-2\imath\delta$ term diverges. However, we have numerically computed the real part of (2.1) with large enough number of modes N_m with $\sum_{n\geq 0} \int \lambda_n = \sum_{n=0}^{N_m - 1} \sum_{j=1}^{H} \lambda_{n,j}$. After a set of simulations, varying the integration step h and the number of atoms N it appears that the property is conserved: $\sum_n \sum_{j=1}^{H} \Re(\lambda_{n,j}) = N$.

The conservation of the trace of the scattering matrix has an important consequence: in the microscopic model the emergence of short lifetimes ($\lambda > 1$, i.e., superradiance) comes automatically with that of long lifetimes ($\lambda < 1$, also known as subradiance) as the sum over the N eigenvalues must be equal to N (in units of $\Gamma/2$). In the continuous model, the finite trace resulting from the infinite sum over the continuous spectrum means that superradiance is not guaranteed, but rather that there is the series of eigenvalues quickly converges to zero; consequently, there are arbitrarily long lifetimes in the continuous model. Indeed, $\Re(\lambda_{n,j}) \to 0$ for increasing n. If the continuous model is to be thought as an approximation of the microscopic model, this means that the disorder present in the latter will actually limit the part of the spectrum that accurately represents it, and will thus limit the lifetimes present in the system. We see in the next section Sec.2.4 that it is not what happens, indeed, superradiant eigenvalues are also present in the MF model.

2.2 Integration step

The integration step h is a numerical resolution parameter that appears solving the continuous model equation (1.21). Smaller h values mean larger integration time. Fig.3, we represent eigenvalues of the first mode $\lambda_{0,j}$ for three integration steps. We clearly see that after some point smaller values of h does not impact much the superradiant eigenvalues but add more subradiant ones in the tail (see inset). As the numerical resolution is of 10^{-14}, eigenvalues with a decay rate smaller than this threshold cannot be trusted so we

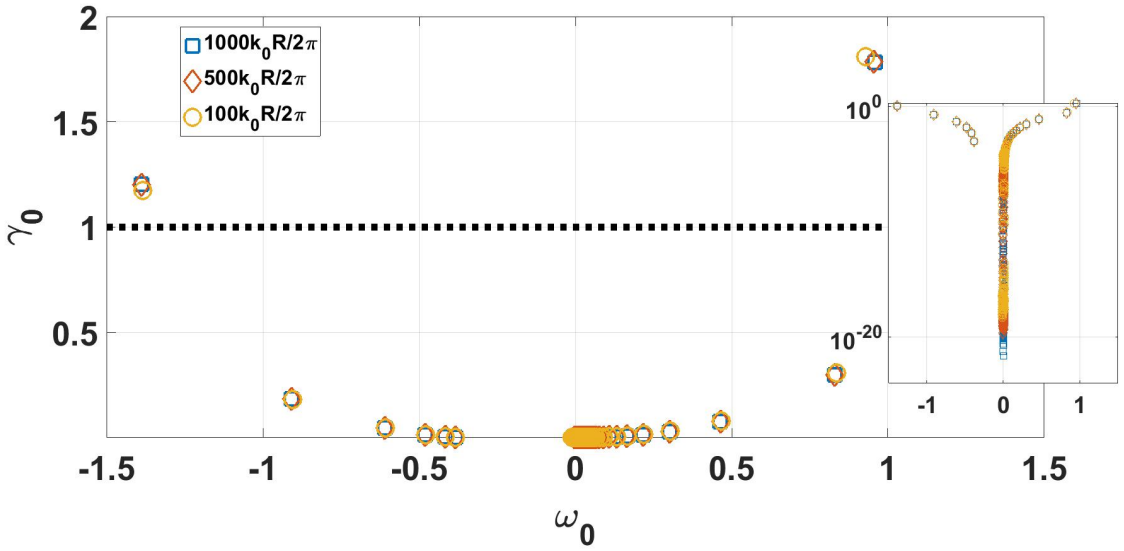

Figure 3 – Eigenvalues λ_n for $n = 0$ represented in the complex plane for three different integration steps. Uniform sphere of radius R, $k_0R = 11.5$, $N = 1000$ atoms, an optical thickness $b_0 = 6N/(k_0R)^2 = 15$ and a density $\rho\lambda^3 = 0.5$.

Source: By the author

will keep a reasonable value of h in order to lower computation time. We have checked that $h = 100k_0R/(2\pi)$ captures well the set of eigenvalues of the system.

2.3 Number of modes computed

Another question raised by the mean-field model is the infinite number of modes as n goes from zero to the infinity. The radial behaviour of the modes is given by Bessel functions as we see in the Mie scattering theory.[23] On the Fig.4, we represent the Bessel functions for different values of n. They oscillate but the global envelop decreases with the increase of the variable r. Moreover, They have the properties $j_{n>0}(r = 0) = 0$ and $j'_n(r = 0) = 0$. And we observe that, close to the origin, as n increases, Bessel functions stay close to the x-axis for further r: it can be mathematicaly formalized by $j''_n(r = 0) \leq j''_{n'}(r = 0)$ for $n' \geq n$. Hence, for a large enough value of the index n_c, $j_{n_c}(r)$ will stay *negligeable* in the interval $[0\ R]$ compare to the Bessel function with index $n > n_c$. When it happens we consider that modes $n \geq n_c$ are not relevant anymore. As it is commun in Mie scattering theory,[23] we consider that the $n_c = 1.5k_0R$ first modes are enough to describe accurately the dynamics, the radial part of mode n corresponding to the $n-$th spherical Bessel function.

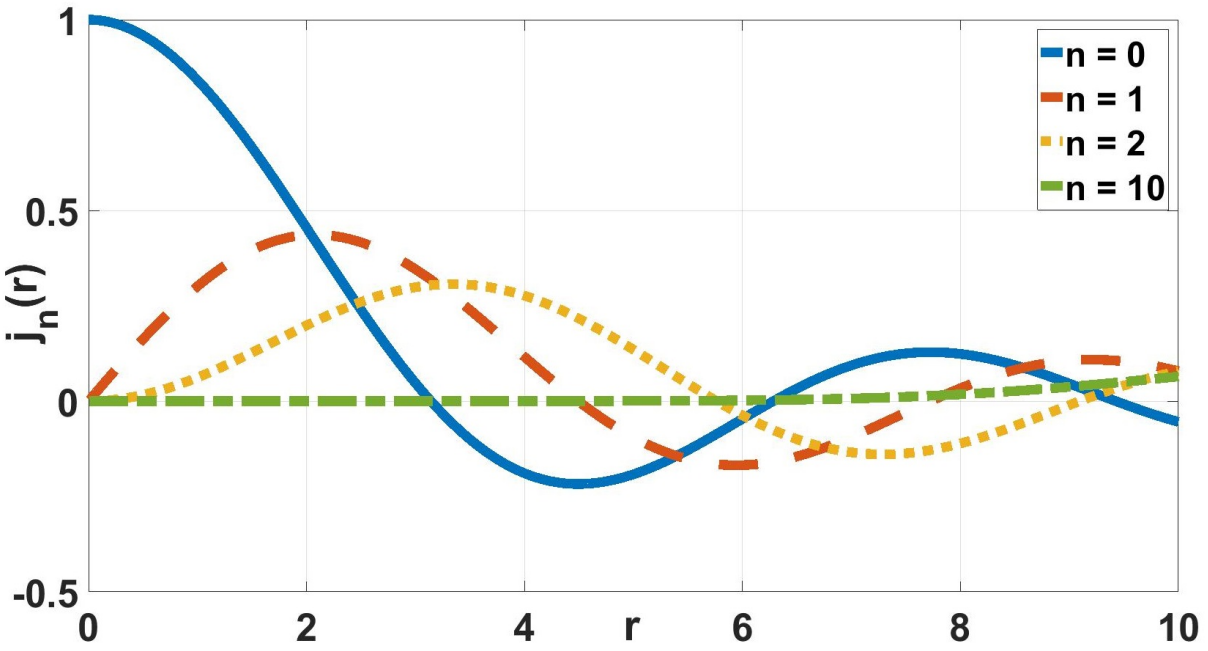

Figure 4 – Spherical Bessel functions of the first kind $j_n(r)$.

Source: By the author

2.4 Spectra: complex plan representation

In this section, we compare the eigenvalues of both models by representing them in the complex plane: the normalized decay rate of the modes in the y-axis and the normalized energy shift in the x-axis. First, as discussed Sec.2.1, we see in Fig.5 that the continuous model contains superradiant eigenvalues.

Then we see that eigenvalues are spread in the shape of a "funnel" for both models. However, we observed that for a uniform density distribution, the eigenvalues of the continuous model would remain on the edge of the "funnel". The spread of the MF model eigenvalues for a Gaussian distribution might be explained by the fact that the Gaussian distribution can be seen as a superposition of uniform spheres of different radius. Hence, the MF model eigenvalue, with a Gaussian distribution of the atoms, are represented over a superposition of "funnel" with different radius. Moreover, if we increase the density, a empty hole of eigenvalues appears in the middle of the "funnel". The Marchenko-Pastur[64] law states that in a dilute regime $\rho\lambda^3 < 1$, where the size of the system is larger than the wavelength $k_0 L > 2\pi$ and for many atoms $N \gg 1$, the eigenvalues represented in a complex plane (linear scale) are contained in a disc of radius $\sqrt{b_0}$. Those effects have been discussed in L.Bellando's thesis[25] as well as the distribution of eigenvalues associated to the pairs of close atoms.[34] Indeed, one superradiant and one subradiant tail would appear in Fig.5 due to the increase of the number of pairs at larger density. It introduces an interesting physics but makes things harder to interpret as they create long-lived modes that are related to

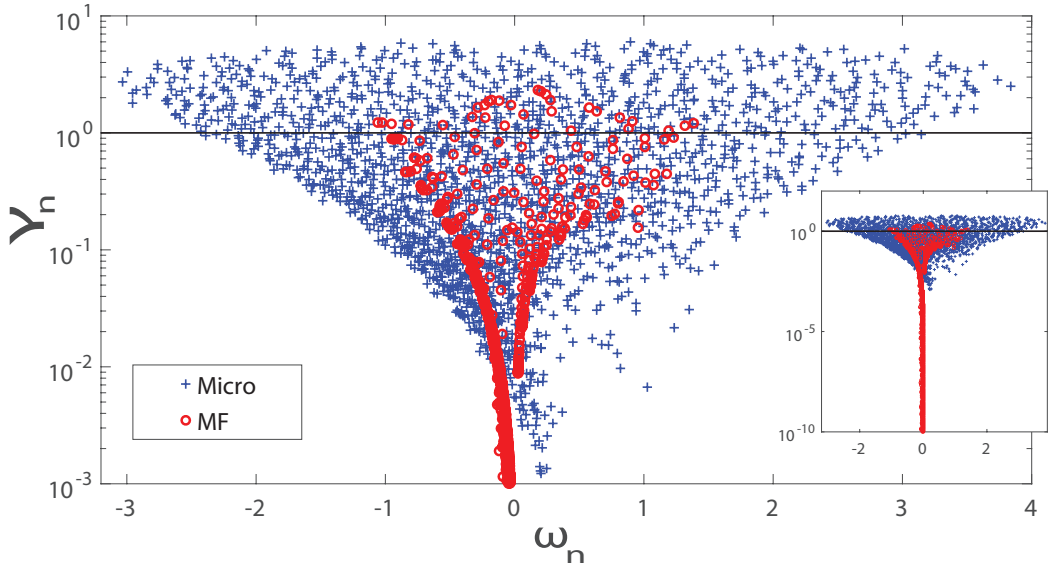

Figure 5 – Eigenvalues in the complex plane $\lambda_n = \gamma_n + i\omega_n$ for the microscopic (blues crosses) and continuous (red circles) models. Simulation realized with a Gaussian cloud of $N = 2000$ particles and a root mean square (rms) of $\sigma \approx 12$ ($b_0 \approx 28.4$), at resonance ($\delta = 0$).

Source: By the author

neither the subradiance nor the diffusion of light.

Interestingly, both models contain super- and subradiant modes as discussed in Sec.2.1. It is not surprising for the microscopic model as it contains a finite number N of eigenvalues λ_n and the sum is finite and equal to N. So, superradiant modes go with the existence of subradiant modes. It is more surprising for the MF model as it has an infinite number of eigenvalues (still with a finite sum). In the inset, we observe that the tail of subradiant eigenvalues for the MF model has arbitrarily small eigenvalues. Hence, the infinite number of eigenvalues for the MF model does not add superradiant eigenvalues but adds subradiant eigenvalues with infinitely long lifetimes (they are here limited by numeric). It also shows that the MF model also presents some subradiance.

Let us comment that throughout this part of the thesis, Part. II, the simulations are realized below the Anderson localization threshold[34,47] ($\rho\lambda^3 \approx 22$), so the subradiant modes observed are not associated with exponentially localized modes but rather to subradiance in dilute systems.[18,65]

In Fig.5 one can observe that the tail of longest lifetimes in the microscopic model presents a shift in energy which is absent from the continuous model. Remark that we here use an exclusion volume (such as the distance between two atoms $k_0 \min(|\mathbf{r}_j - \mathbf{r}_i|) > 3$) to avoid pair effects as discussed in Refs.[18,35–38] In order to understand the origin of this shift, we look at the scaling laws describing it. Practically, we compute the average

energy shift of the 5% most subradiant eigenvalues, and observe that its scales as $N/(kR)^a$ with $a \approx 4 \pm 0.5$, see Fig.6. It is thus different from the scaling of the Lorentz-Lorenz and collective Lamb shift, which scales with the density. Remark that since this shift is associated with the subradiant tail, it may not be visible in the stationary state, but may instead require a study of the late-time discharge dynamics of the cloud.

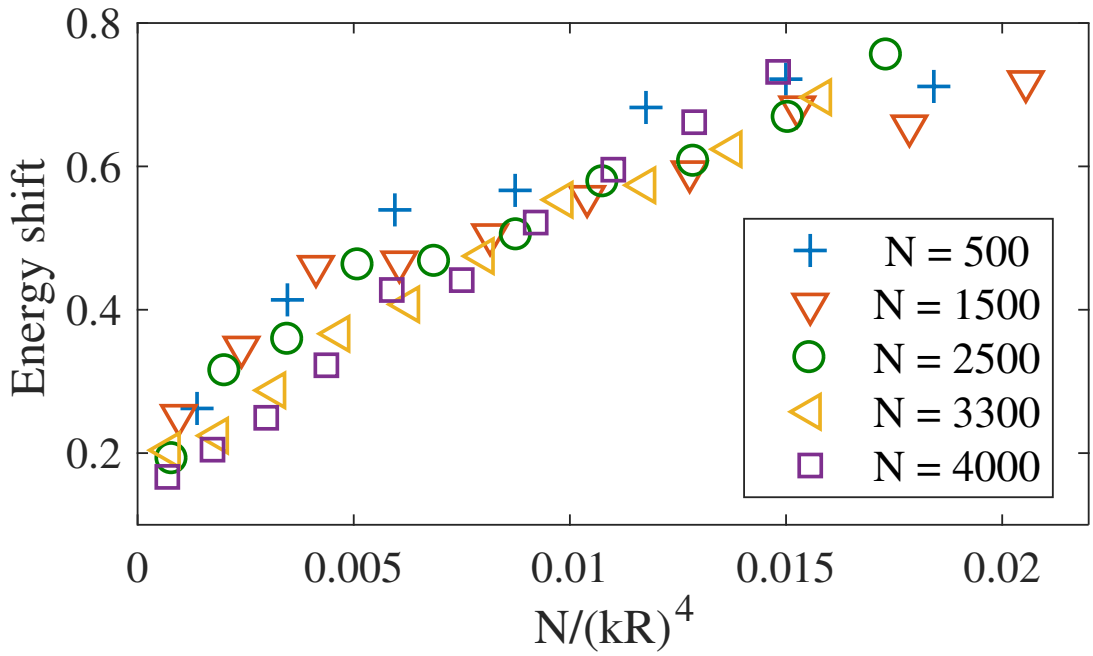

Figure 6 – Average energy shift of 5% most subradiant eigenvalues, for a cloud with Gaussian density and scalar light, illuminated at resonance for the microscopic model.

Source: By the author

2.5 Participation Ratio and mode size

Scattering modes with long lifetimes can be associated with spatial localization, as in the case of Anderson localization or in whispering gallery modes. These latter modes are not present in our system due to the Gaussian density considered: Smooth densities do not allow for surface modes to propagate by internal reflection.[9] As for long lifetimes modes inside the cloud, they have been shown to be responsible, in the microscopic model of scalar light, for a localization transition.[47,66]

Let us first check the connection between the lifetime of the modes and their spatial extension by computing their participation ration (PR), which quantifies the number of atoms participating substantially to it. The PR of mode n is defined in, respectivelly, the

microscopic and MF model as:

$$\mathrm{PR}_n = \frac{\left(\sum_j |\beta_j^n|^2\right)^2}{\sum_j |\beta_j^n|^4}, \tag{2.8}$$

$$\mathrm{PR}_n = \frac{\left(\int \rho(\mathbf{r})|\beta_n(\mathbf{r})|^2 d\mathbf{r}\right)^2}{\int \rho(\mathbf{r})|\beta_n(\mathbf{r})|^4 \, d\mathbf{r}}. \tag{2.9}$$

Fig.7 depicts the PR for both models and the PRs are qualitatively similar: Superradiant modes have a large PR, which correspond to spatially extended modes; longer lifetimes are associated to a lower PR, and thus to a stronger localization in space. Note that, as the mean-field approach contains no disorder, one does not expect a disorder-based localization transition (see Part.III), with the emergence of exponentially localized modes. Hence, Fig.7 has not any localized modes even for really low PRs.

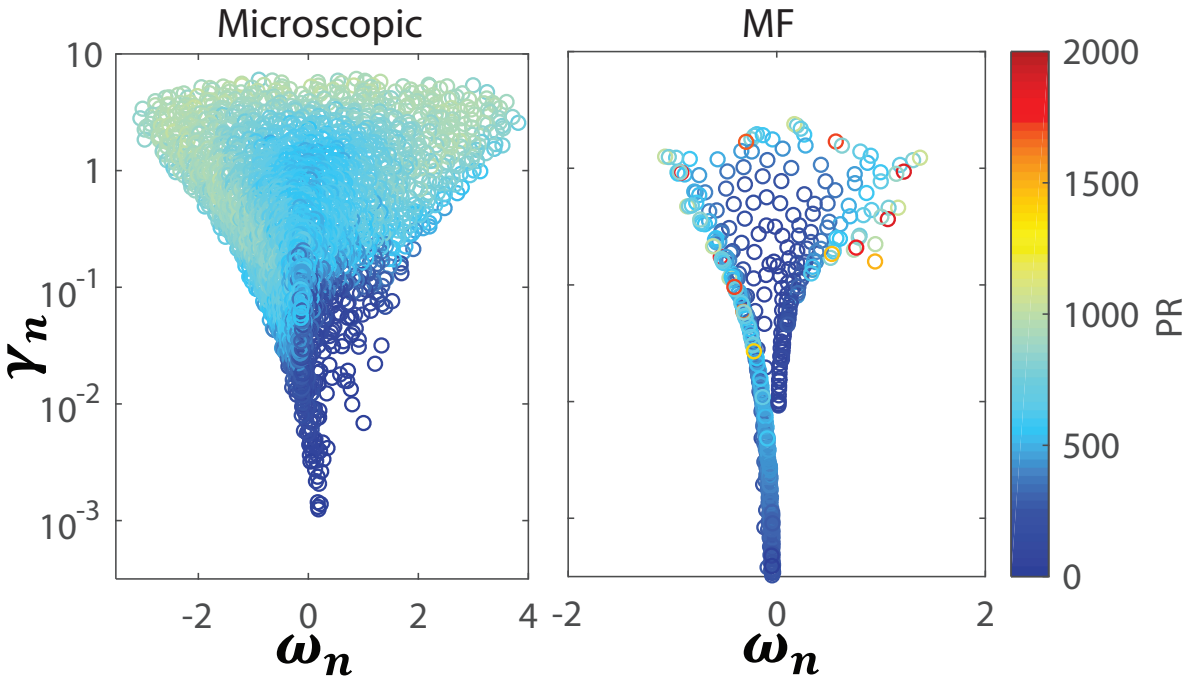

Figure 7 – Participation ratio of the microscopic (left) and MF (right) models for a Gaussian cloud with $N = 2000$ atoms with optical thickness $b_0 \approx 30$, at resonance.

Source: By the author

The participation ratio quantifies how many atoms participate in the mode. It is intuitive to think that atoms composing a mode of low PR are close to each other and localized in space whereas for a large PR atoms would be spread into the cloud. To quantify better how spread are the modes with a large PR, we monitor their second momentum or mode size. This study is done only for the microscopic model. It is given by computing

the average radius of a mode for the microscopic model :

$$\sigma_n^2 = \sum_j |\beta_j^n|^2 ||\mathbf{r_j} - \mathbf{r_n^{CM}}||^2, \tag{2.10}$$

$$\mathbf{r_n^{CM}} = \frac{\sum_j |\beta_j^n|^2 \mathbf{r_j}}{\sum_j |\beta_j^n|^2}. \tag{2.11}$$

It quantifies if one mode is spatially spread or localized. We clearly see in Fig.8 that the most subradiant modes are localized as they have a low σ/R. It seems that it exists superradiant modes that can be both spatially spread or localized.

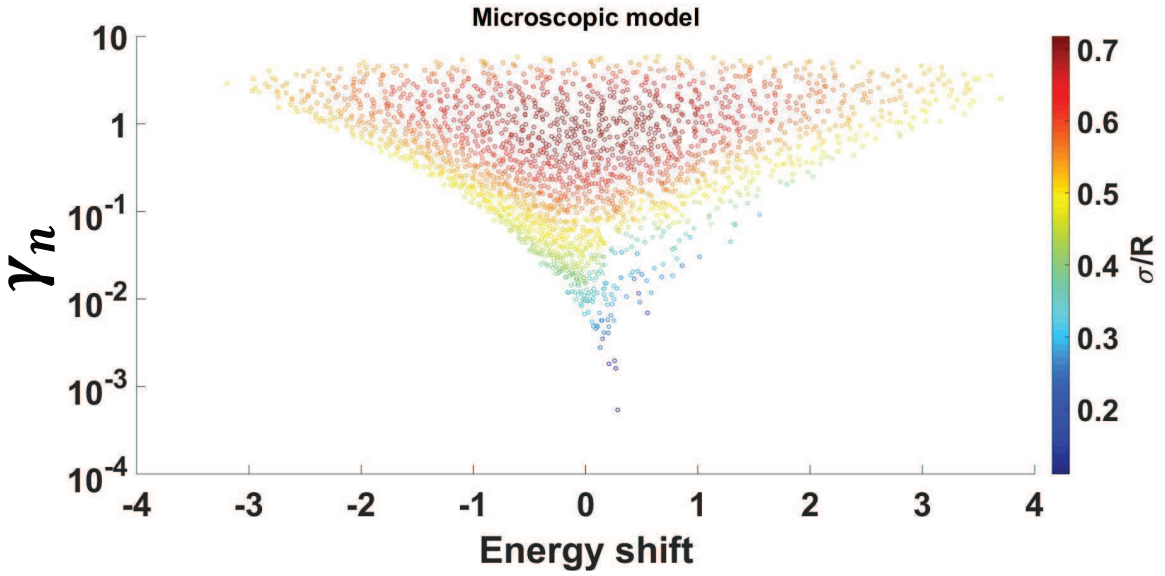

Figure 8 – Mode size with a Gaussian density and scalar light, $N = 2000$ atoms, $b_0 = 27.86$ and at resonance, $\delta = 0$, using microscopic model.

Source: By the author

We conclude from the two previous figures that superradiant modes are more likely delocalized and subradiant modes localized for both models. We show in Fig.9 the spatial representation of one superradiant and one subradiant mode, the size of the markers giving the weight of the given particle into the mode. We clearly see that the superradiant mode is spread through all the cloud and atoms participate more or less equally. On the contrary, the subradiant mode is clearly localized on few particles.

2.6 Conclusion

The main result of this section is that the continuous model has similar properties than the microscopic model on a spectra point of view. More specifically, super- and subradiant modes are present in both models. Moreover, subradiant modes are spatially localized (not Anderson localized neither whispering gallery modes), differently from superradiant modes.

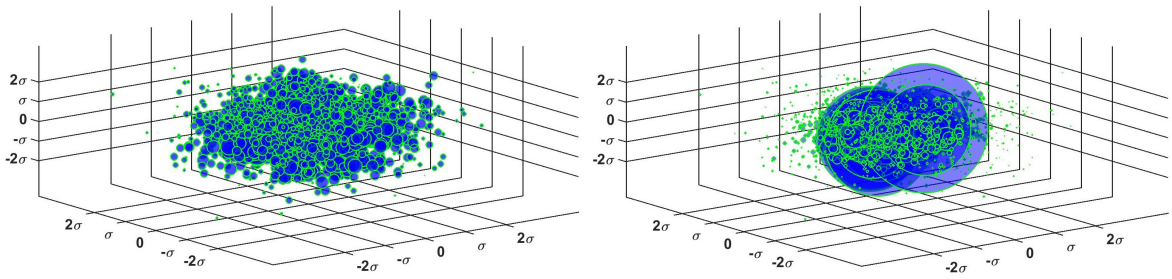

(a) $\gamma_1 = 8.10$ (b) $\gamma_{1805} = 0.0057$

Figure 9 – Mode representation in the xyz plane with a Gaussian density and scalar light (no exclusion volume), $N = 2000$ atoms, $b_0 = 30$ and at resonance $\delta = 0$ using CD model.

Source: By the author

3 RADIATED INTENSITY

We have so far compared the two models through their eigenvalues, eigenvectors and PRs. Those quantities are extracted from the matrix D introduced in Ch.1.3 and results in the geometry of the cloud: disorder, density, size, etc. However, this analysis does not include the incident laser and, more precisely, the coupling between the laser and the modes. Indeed, in the previous section, all modes were treated equally despite they are not populated equally by the laser. Different modes may couple with very different amplitudes to the incident wave, so the eigenvalue analysis reveals only part of the information. In particular, the radiated field may carry the radiation from only a few modes. For instance, superradiant modes are less *important* if they are not populated by the laser, the same holds for subradiant modes. *Important* here means that the non-populated modes do not contribute significantly to the radiated field. Eigenmodes appear to have similar features in the two models but it reveals only part of the information on the cloud radiation as it does not say how a plane wave couples to each mode. The coupling between the laser and the modes is an important question for experiments. For instance, localized or super- and subradiant modes can be observed only if they are populated.

One parameter used, theoretically and experimentally, to control the coupling between the light and the atoms, is the detuning between the atomic frequency transition and the laser frequency $\Delta = \omega_0 - \omega_a$. One of the advantages of working with cold atoms is to be able to work really close to resonance $\Delta = 0$, thanks to the negligible Doppler effect. In a recent work,[67] the role of the laser detuning has been investigated to directly look at the steady-state population of modes. In our work, we do not investigate directly modes population but rather the dynamics of the radiation of the cloud which is a consequence of this population.

The optical thickness is defined as $b(\delta) = b_0/(1+4\Delta^2/\Gamma^2)$ and characterizes the propagation of light through the cloud in the laser direction. It is used to distinguish two regimes: the single scattering regime, $b \ll 1$ and the multiple scattering regime, $b \gg 1$. A remarkable aspect of the coupled-dipole problem is that at large detuning, despite the cloud becomes essentially transparent to the incident light, superradiance and subradiance are still present. Those effects are nonintuitive as one can expect that in the single scattering regime atoms behave independently and cooperative scattering effects vanish. Looking at those effects with the continuous model will help to better understand its origins and for instance the role of disorder. These two phenomena present a scaling with the resonant optical thickness $b_0 = 2N/(k\sigma_r^2)$.[18,35,39,65,68,69] We will discuss this scaling for the continuous model in this section. It is different, for example, from radiation trapping which scales with the optical thickness $b(\delta) = b_0/(1 + 4\Delta^2/\Gamma^2)$ and vanishes in the large detuning limit ($b \to 0$).[7,60,61] Hence, subradiance has to be distinguished from radiation trapping. Radiation trapping

can be described by the radiative transfer equation, that does not include phases and interferences, whereas the subradiance cannot as it is a destructive interference effect. In this thesis, we are focusing on subradiance rather than radiation trapping.

We study the laser-modes coupling by investigating super- and subradiance phenomena with the microscopic and continuous models. To do so, we consider a plane wave as an incident laser that charges the cloud for a long time ($50\Gamma^{-1}$), before being turned off abruptly (at $t = 0$) then we compute the radiated intensity $I(t) \propto |E_{sc}(t)|^2$ that is derived below. The cloud is modelled by a Gaussian sphere distribution of *rms* size σ. For the continuous model, the radius of integration R is taken as $R = 3\sigma$. We also introduce, for the microscopic model, an exclusion radius to exclude pair physics.

3.1 Scattered intensity

The intensity at position $\mathbf{k} = k_0\hat{\mathbf{k}}$, scattered by the cloud, is defined as $I_{sc}(\mathbf{k}) = \frac{1}{2}\epsilon_0 c|E_{sc}(\mathbf{k})|^2$. For the microscopic model the scattered field is:

$$E_{sc}^{M}(\mathbf{r},t) = -\frac{\hbar\Gamma}{2d}\sum_{j=1}^{N}\beta_j(t)\frac{e^{\imath k_0|\mathbf{r}-\mathbf{r_j}|^2}}{k_0|\mathbf{r}-\mathbf{r_j}|^2}, \tag{3.1}$$

with d the matrix dipole element of the transition and β_j are the dipole functions computed from equation (1.2). In the far field limit (Fraunhofer approximation[70]) we have $|\mathbf{r}-\mathbf{r}_j| \approx r - \mathbf{r}\cdot\mathbf{r}_j/r$, then $k_0|\mathbf{r}-\mathbf{r}_j| \approx k_0 r - \mathbf{k}\cdot\mathbf{r}_j$. It allows us to use a simpler expression. Moreover, in all this chapter Ch.3.4 we focus on the normalized intensity *i.e.* $I_{sc}(\mathbf{r},t)/I_{sc}(\mathbf{r},t=0)$ so we do not carry the constants. Finally, the radiated intensity from the cloud, in the far field limit, in direction $\mathbf{n}$ can be expressed for the two models as:

$$I_M(\mathbf{n},t) \propto \left|\sum_{j=1}^{N}\beta_j(t)e^{-\imath k\mathbf{n}.\mathbf{r_j}}\right|^2, \tag{3.2}$$

$$I_C(\mathbf{n},t) \propto \left|\int_V \rho(\mathbf{r})\beta(\mathbf{r},t)e^{-\imath k\mathbf{n}.\mathbf{r}}\,d^3\mathbf{r}\right|^2. \tag{3.3}$$

Dipole functions are computed using (1.2) and (1.21) and finally the radiated intensity is computed using expression (3.2) and (3.3).

In fig.10, we represent an example of the intensity as a function of time for the microscopic and the continuous models, for a cloud with a Gaussian distribution and after the laser was on for $50\Gamma^{-1}$. We see that the emission of the cloud is first characterized by the fast decay associated with the superradiant modes, which dominates the short time dynamics as they initially carry most of the energy. Yet, they quickly lose their population and soon the long-lived emission of the subradiant modes take over. This first observation is a confirmation that both models describe a super- and subradiant dynamics. We precise that superradiance, respectively subradiant, is not characterized by only the most superradiant eigenvalue $\max(\Re(\gamma_n))$, respectively the most subradiant eigenvalue $\min(\Re(\gamma_n))$, but rather

results from the competition between a set of superradiant, respectively subradiant, modes with different energies and populations. Hence, super- and subradiant slope that can be extracted from Fig.10 are not directly related to the decay rate of one specific mode.

The presence of super- and subradiant modes in both models was already shown in Sec.2.6 by looking at the spectra but Fig.10 gives more information about their population. An interesting result is that super- and subradiance remain for large detuning where the single scattering regime is reached ($\delta = -10$ curves, corresponding to an optical thickness of $b \sim 0.07$). It is a nontrivial result as one may expect that in the deep single scattering regime, particles behave independently. It shows that cooperative effects still exist far from resonance. Indeed, several works demonstrated that both the 3D superradiant and subradiant rates in large dilute clouds are characterized by a "cooperativity" parameter, namely the resonant optical thickness $b_0 = 2N/(k\sigma^2)$.[18,35,39,65,69] Finding this scaling with the continuous model will be one objective of Sec.3.2 and Sec.3.3.

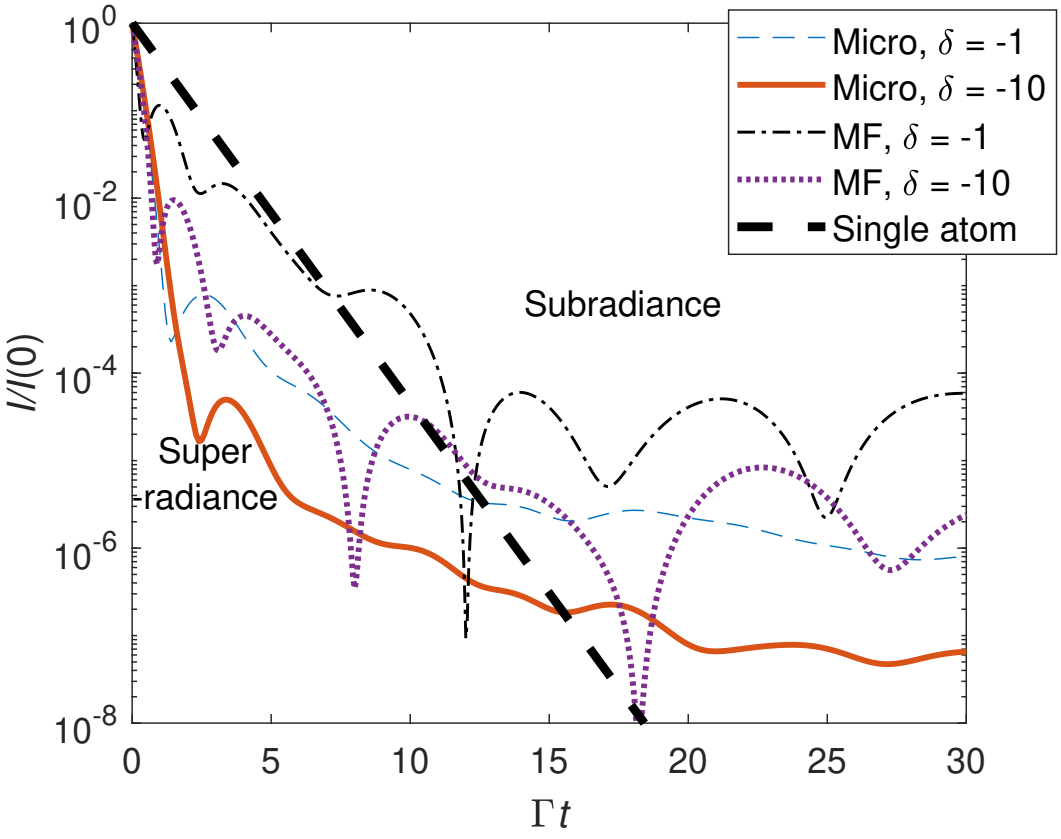

Figure 10 – Emission dynamics of the forward scattered light after the laser is switched off ($t = 0$), for the microscopic and the MF models. Simulations realized for a Gaussian cloud with $b_0 \approx 28$ and $N = 1900$ atoms, close ($\delta = -1$) and far ($\delta = -10$) from resonance. In the forward direction $\theta = 0$.

Source: By the author

The two models also present significant oscillations of the intensity during the decay

dynamics, when many modes with similar energies compete. Those oscillations can be lowered by averaging the intensity over many realizations for the microscopic model,[18,65] yet it is not possible for the MF model as it contains no disorder. It will be a limitation for subradiant investigations, as we will see in Sec.3.3.

We want to illustrate that these oscillations result in the difference of the energy shift between the modes. The imaginary part of the eigenmodes introduce a *competition* between the modes while the intensity is computed. To understand those oscillations, and the idea of *competition* between the energy shift, we take the simple example of the function $I(t) = |e^{-(\gamma_1+\imath\omega)t} + e^{-(\gamma_2-\imath\omega)t}|^2$ that is the module square of two exponential functions. It is supposed to represent the radiated intensity of two identical particles of eigenvalues $\gamma_1 + \imath\omega$ and $\gamma_2 + \imath\omega$ with the property $\gamma_1 + \gamma_2 = 2$. First case: if $\gamma_1 = \gamma_2 = 1$ then the *intensity* is $I(t) = e^{-2t} 4\cos^2(\omega t)$ and follow an exponential with oscillations of frequency of $\omega/2\pi$. If $\gamma \gg \omega$ oscillations of the cosine will not be visible as the intensity will oscillate on a long time compared to the exponential decay. Second case: if $\omega = 0$ and the decay rates differ from more than one decade. Then the curve will be, in semilogarithmic representation, two-lines with two slopes of $1/\gamma_1$ and $1/\gamma_2$, we see on the orange curve in Fig.11 the two asymptote behaviours. Considering the intermediate case, let us take for instance $\gamma_1 = 0.1$ that refers to the long-lifetime and $\gamma_2 = 1.9$ that drives the short times and we represent Fig.11 the *intensity* for different exponents that might model phases. On one hand, when $\omega \ll \gamma_1$ oscillations are larger than the longer lifetime of the exponential. On the other hand, if $\omega \gg \gamma_2$, oscillations represent a wave packet where the *envelop* is the exponentials. This discussion shows that the oscillations in the intensity computed by (3.2) are due to the energy shift difference between modes. Extending this simple two-particles example to an N-body systems leads to the complex situation where we have a competition between many modes between all the modes.

3.2 Superradiant rate

We see in Fig.10 that we can extract a slop at the origin to characterized the short time behaviour of the radiated intensity that is called the superradiance (SR) rate. Theoretical work using the coupled dipoles model[65] and experimental analysis[18,35,35,39,69] showed that the SR rate Γ_N scale with b_0 as $\Gamma_N = (1 + b_0/12)\,\Gamma$. We compare the two models at large detuning when refraction dominates on diffusion in the forward direction. Indeed, the two models describe accurately refraction whereas diffusion is not well-described by the continuous model. A detailed study of the superradiant rate dependency on the cloud characteristics (size and particle number) and on the light-atom coupling (detuning) is shown in Fig.12 in the forward direction. It reveals that just as in the microscopic approach,[35] the relevant scaling parameter at large detuning $\delta > 2$ is the resonant optical thickness as the SR rate scales linearly with b_0. Consequently, the phenomenon is still present in the large detuning limit, only subradiant eigenmodes population decreases as the

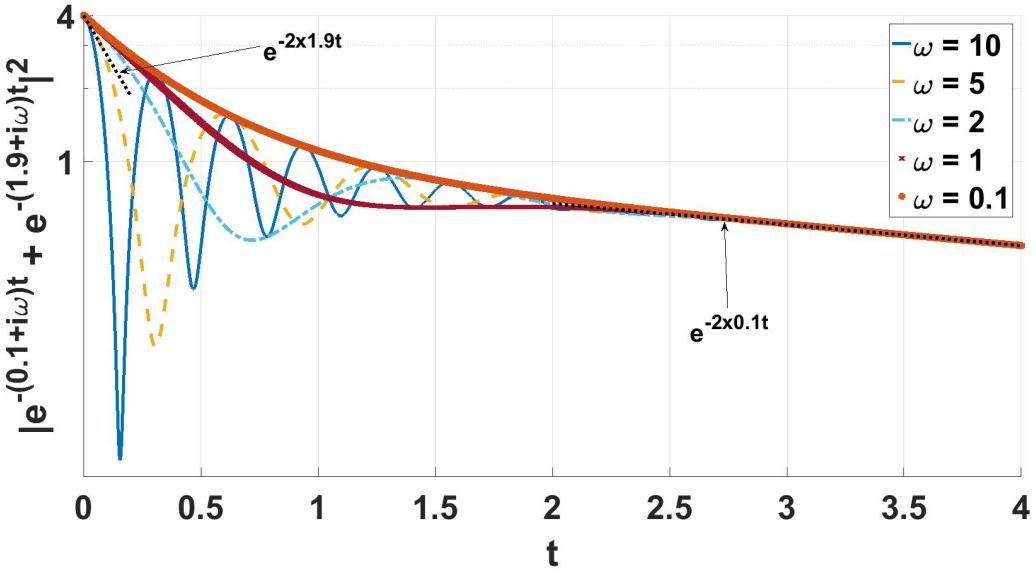

Figure 11 – We plot $\left|e^{-(0.1+i\omega)t}+e^{-(1.9+i\omega)t}\right|^2$ that refers to the radiated intensity of two modes as a function of the time t.

Source: By the author

cloud turns transparent. It means that for a given b_0, the slope at the origin (supperradiant rate) would be the same but the SR regime would be shorter in time as the SR modes are less populated (illustrated in Fig.10).
Moreover, we see an increase in the superradiance close to resonance. In stationary regime (when the laser is kept on), the intensity in the forward direction follows the Mie lobes as illustrated in Fig.14. First, the main lobe decreases with the detuning increases. Then, in the specific forward direction, a significant part of the light is refracted from the border of the cloud in single scattering (due to the Gaussian distribution at the border of the cloud). Those two effects, the decrease of the forward lobe and the presence of the single scattering, explain that the SR rate increases at resonance in the forward direction.

The scaling of the SR rate with b_0 in the MF model shows that it captures well this cooperative phenomenon, despite a discrepancy of a factor ~ 2 between the two models.

Let us now comment about the low-b_0 limit. We see in Fig.13 that the continuous model presents a SR rate of Γ_{SR} that vanish in the low-b_0 limit whereas in the microscopic model the single-atom physics is recovered in the very dilute limit ($\Gamma_{SR} \to \Gamma$). It is consistent with the fact that the continuous approach requires many particles to be a valid approach.
Interestingly, the microscopic model shows an *enhanced* SR rate compared to the continuous model, which suggests disorder is actually favourable to SR.

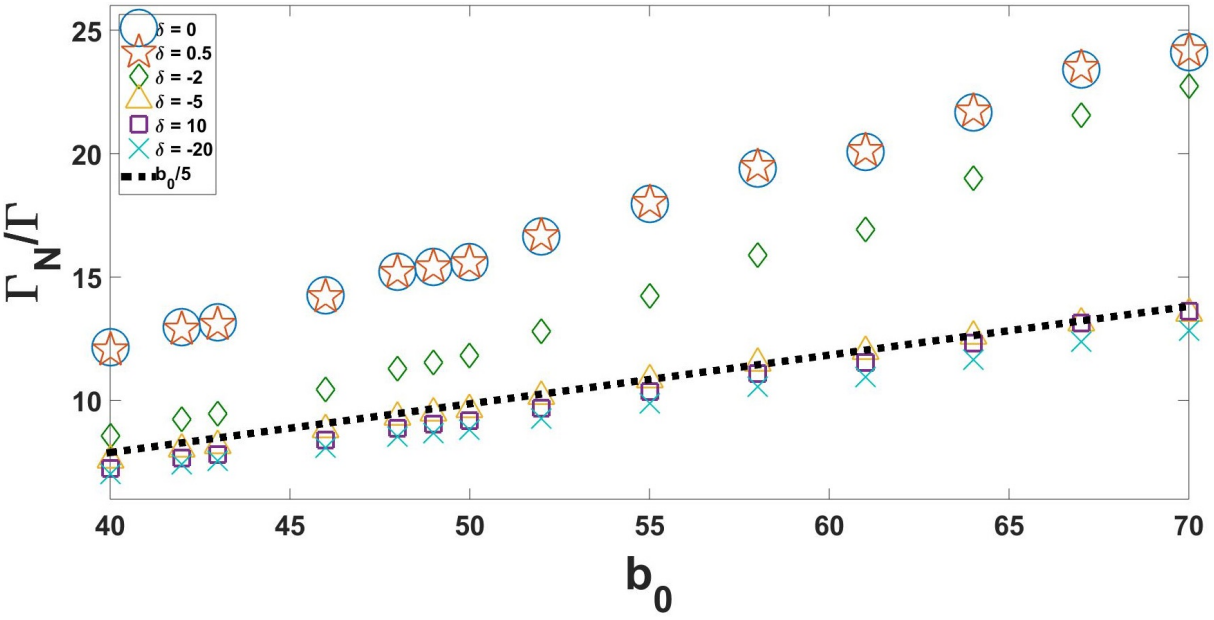

(a) Continuous model

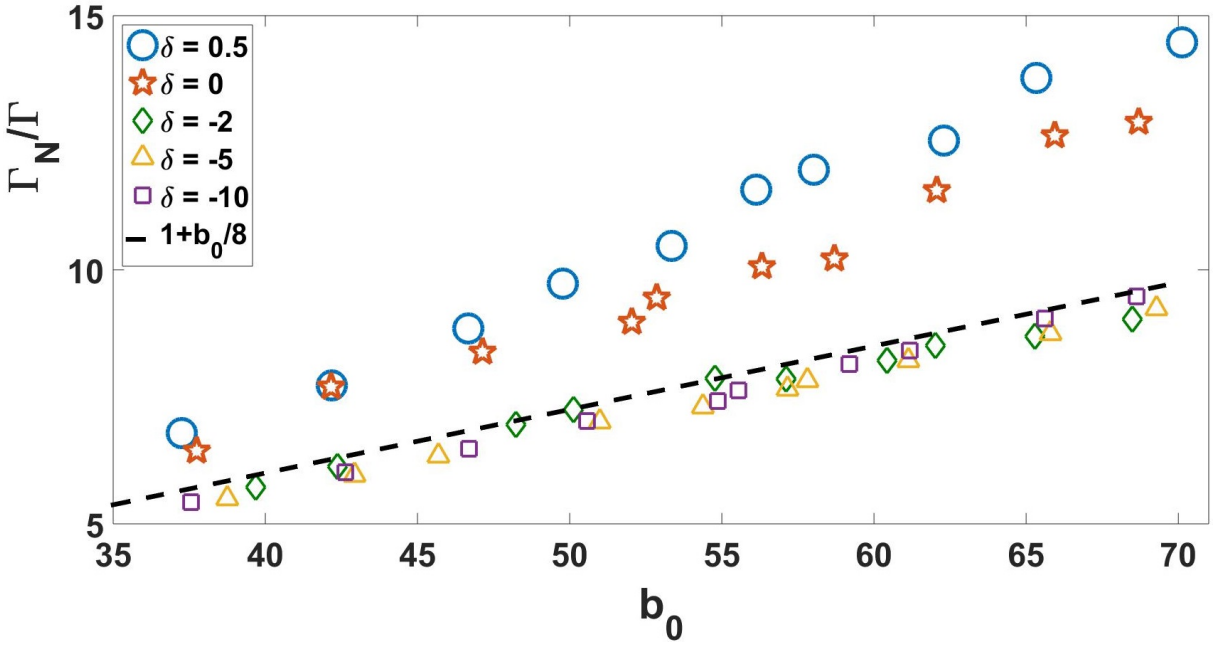

(b) Microscopic model

Figure 12 – Superradiant rate for the continuous (a) and microscopic (a) models at resonance and out of resonance, for different values of the detuning. Simulations realized for a Gaussian cloud of $N = 1000$ atoms in the forward direction $\theta = 0$.

Source: By the author

3.2.1 Angular dependency

Superradiance is usually explained by a coherent emission by in-phase dipoles. This typically leads to look for SR in the direction of the coherent driving, where a coherent

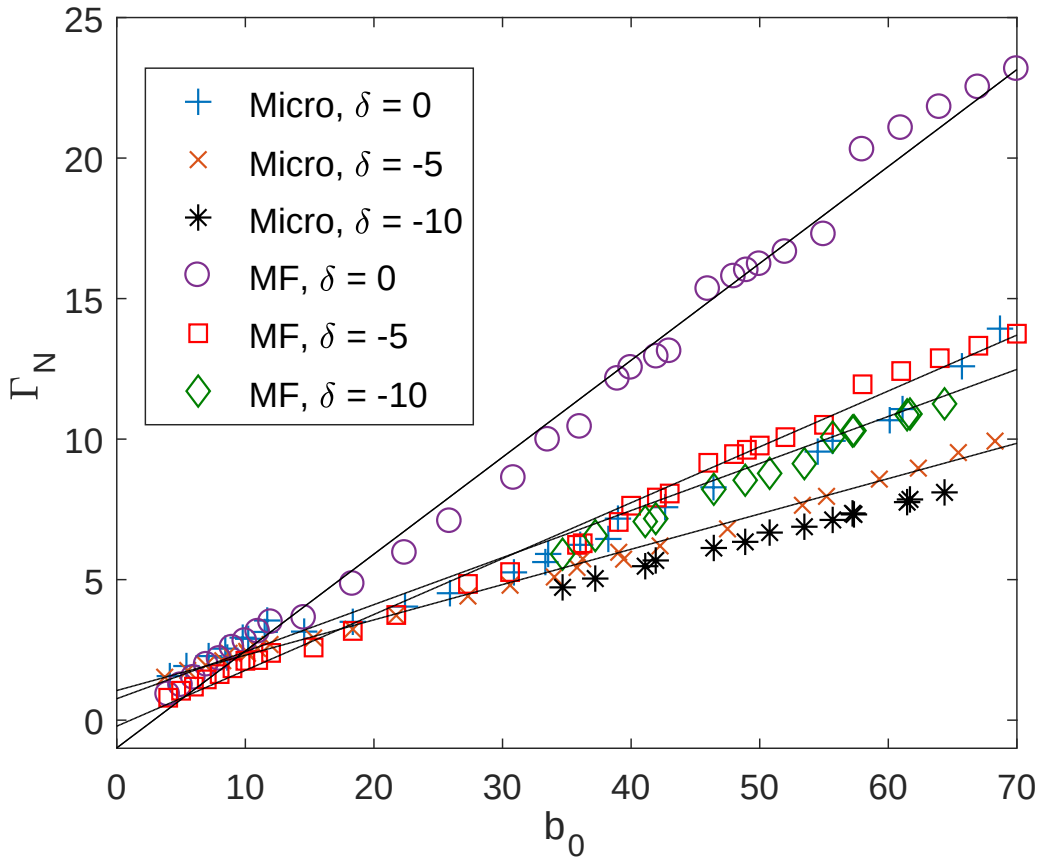

Figure 13 – SR rate in the forward direction ($\theta = 0$) as a function of the resonant optical thickness for the microscopic and mean-field models, at resonance ($\delta = 0$) and out of resonance ($\delta = -5,\ -10$). Simulations realized for a spherical Gaussian cloud of $N = 1000$ atoms.

Source: By the author

phase pattern is imprinted.[15] Yet, it has been shown recently that the off-axis emission was also superradiant[35] despite the atomic dipoles are not expected to exhibit specific phase pattern in the transverse directions, where diffuse light is emitted. It was an unexpected result that we also observe in Fig.14(a) where we represent the angular dependence of the short-time emission rate in the microscopic model and at large detuning. In this regime of large detuning, radiation trapping is negligible. Despite strong fluctuations due to the atomic disorder, it is superradiant in almost all directions. At initial times, superradiant rates appear only in arbitrary directions, depending on the specific realization. As reported previously,[35] SR is slightly weaker in the direction of the driving where more energy is radiated.

Fig.14(b) is the same as Fig.14(a) but for the continuous model. It presents similar features than for the microscopic model: SR rate exists in every direction and is lower in the forward direction. Indeed, Mie scattering lobes match with lower values of Γ_N.

This preservation of the off-axis SR rate in both models is particularly surprising considering

that in these directions, for optically dense clouds the diffuse light dominates in the microscopic model whereas only Mie lobes of coherent scattering are present in the MF model. Hence, we observe two kinds of superradiance: one arises from disorder and so diffusion and the other one from coherent scattering light. The dominance of one superradiance on the other is not studied here. Since the continuous model does not include diffuse light, the superradiance characteristics of the latter, as well as its competition with the off-axis coherent light, cannot be studied.

In addition, we observe that except for the forward direction, the SR rate is relatively constant in all directions as already observed.[35] It has been showed[38] that the subradiance rate is independent of the angle of observation. Hence, at large detuning, radiation trapping is negligible and the relative population of super- and subradiant modes is quite constant.[67] They are just all less populated as δ increases and the cloud become transparent. The picture is the following far from resonance: the laser sees all the modes equally and does not make a difference between modes with small energy shift difference ($\delta \gg \omega_n - \omega_{n+1}$). On the contrary, if δ is on the order of ω_n (see Fig.5) the laser will more likely coupled with some modes.

3.3 Subradiance

Regarding subradiance, the long-lived modes are also present in the MF model, which can be somehow counter-intuitive: SR modes are associated with in-phase dipoles whereas subradiant modes are associated with less regular phase patterns. Thus, the MF model and its macroscopic modes appear as less suitable to support subradiant modes, as compared to the microscopic disordered model. However, higher-order modes in the MF approach (i.e., corresponding to large indexes n) correspond to higher-order spherical harmonics, which precisely present spatial pattern with a large number of oscillations (see Fig.15). This analysis is also consistent with the fact that the large-n limit is associated with deeply subradiant modes (see inset of Fig.5). The picture that out-of-phase modes are responsible for subradiance holds with the MF model. The spatial representation of one subradiant mode shows a localized mode in the center of the cloud (not in the sense of Anderson localization) which is consistent with Fig.9 done for the microscopic model.

Like we did for the SR rate in section Sec.3.2, a more quantitative description of subradiance requires the characterization of the emission rate at late times ($t > 1/\Gamma$). Because of the oscillations of the radiated intensity originating in the interference between several modes with slightly different energy, an averaging procedure is necessary to obtain monotonic decay curves and extract a subradiant rate. Whereas this is performed by averaging over disorder configurations in the microscopic case,[18,65] the intensity in the MF model cannot be averaged, as it contains no disorder. Furthermore, creating different *configurations* by slightly changing the cloud characteristics (size, density, particle number)

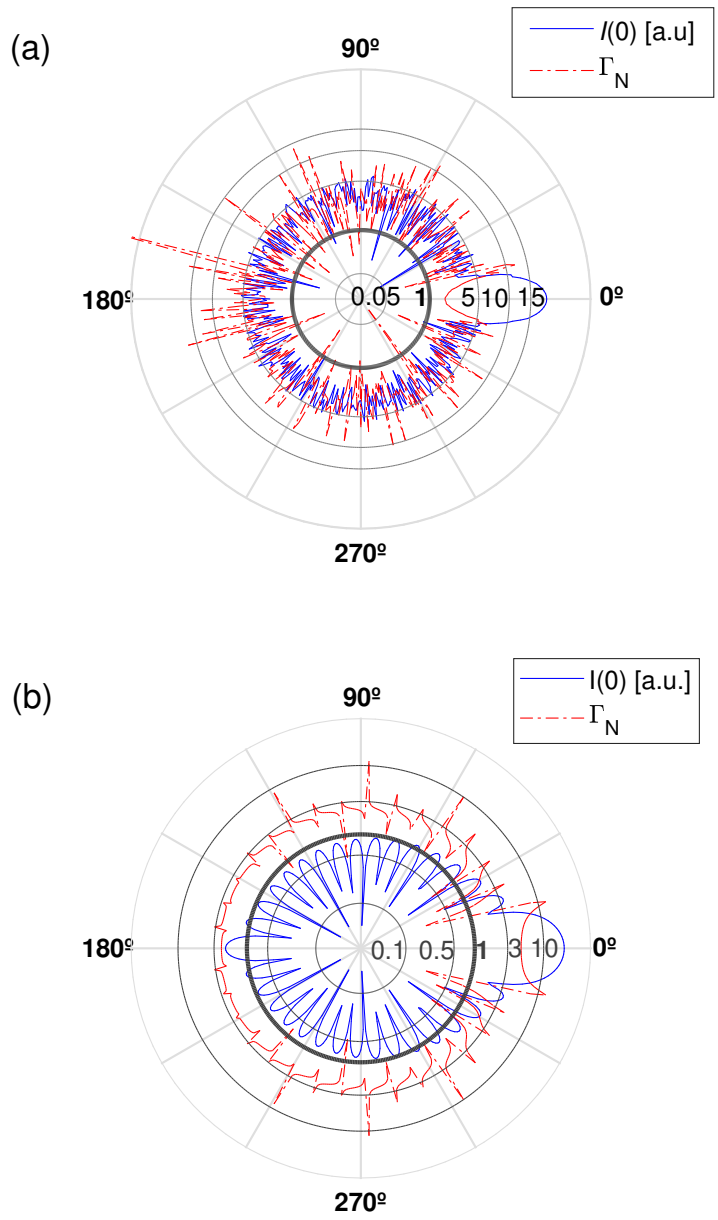

Figure 14 – Angular dependence of the initial radiated intensity $I(0)$ (blue plain line) and SR rate Γ_N (red dash–dotted line) in logscale for the (a) microscopic and (b) mean-field models. The rate is computed over the time window $t \in [0; 0.1]/\Gamma$ for a cloud charged by a plane-wave during a time $50\Gamma^{-1}$ until $t = 0$. Simulations realized for a Gaussian cloud with $b_0 = 28.7$, $\delta = -10$ and $N = 1908$. The gray circles describe the level of the SR rate, the thick one corresponding to the single–atom rate $\Gamma_N = 1$.

Source: By the author

does not allow to smooth efficiently the intensity dynamics as the modes (and their energy) is only slightly affected. Moreover, there is the question of the fitting window for the subradiant rate that is not trivial. Indeed, after the superradiant decay, many different

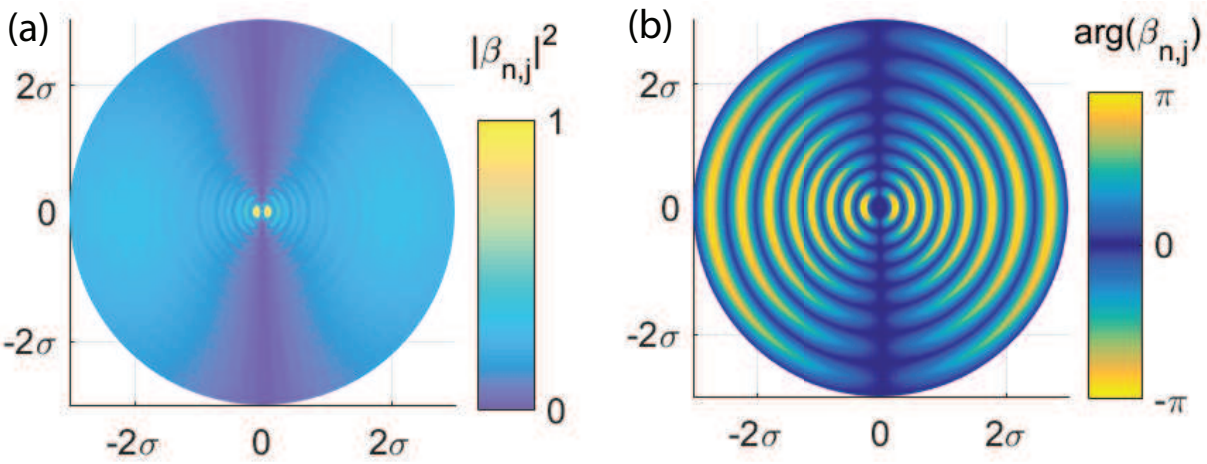

Figure 15 – Spatial (a) intensity and (b) phase profiles of a subradiant mode of the MF model: $\gamma_{n,j} \approx 0.04\Gamma$, corresponding to $(n, j) = (1, 13)$ for a Gaussian cloud with the same parameters as in Fig.5.

Source: By the author

subradiant decay rates may be observed, depending on the temporal window considered. At resonance, the slope might refer to the radiation trapping and not the subradiance. Finally, experimentally the signal that can be detected leads to considering intensities of at least 10^{-6} as compared to the one in the stationary regime. In spite of these limitations, a subradiance rate analysis is done.[38]

Although a quantitative comparison is difficult to obtain, the cooperative nature of the subradiance observed in the MF model, as opposed to the incoherent phenomenon of radiation trapping, can be assessed by studying the decay dynamics in the large-detuning limit, where the cloud optical thickness vanishes. Fig.16 describes the decay dynamics for the two models, for a single realization and for different values of cloud sizes: apart from the qualitative resemblance between the two dynamics, an important point is that in both cases the far-detuned limit does not correspond to single-atom dynamics, i.e., collective modes are still present, associated with decay rates very different from the single atom one. This confirms the existence of subradiance in the MF model, in a regime where radiation trapping is absent.

3.4 Conclusion

In this section, we showed that super- and subradiance is present in both models and even at large detuning, cooperative effects remain. Out-of-resonance, SR scales with b_0 for both models. Subradiance still exists in the single scattering regime. Subradiance can be explained by out-of-phase modes in opposition of in-phase dipoles for superradiance.

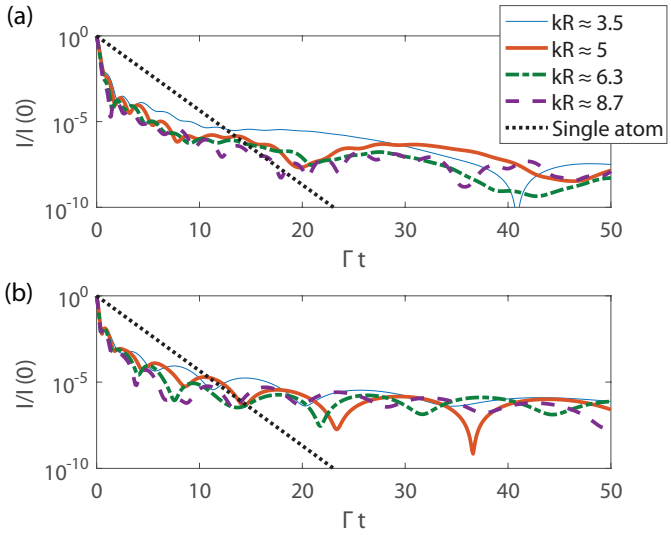

Figure 16 – Far-field intensity radiated in the forward direction, for a Gaussian cloud distribution with $b_0 = 80$ and driven far from resonance ($\delta = -10$). Using the (a) Microscopic and (b) mean-field model.

Source: By the author

Part III

Continuous model for Anderson localization

4 INTRODUCTION TO ANDERSON LOCALIZATION

4.1 Origin of Anderson localization

In his original paper,[11] P.W. Anderson first established that diffusion of an electron in the absence of electron-electron interactions might vanish by increasing the disorder of a random potential. The original idea was to study the probability for one electron to stay on one lattice site or to spread all over the medium. A particle in a random potential can escape and hence diffuse when its energy is greater than the maximal value. On the other hand, the particle can be trapped in a local minimum of the potential. For a quantum particle, the energy needed to make a transition between a localized and diffusive regime is greater than the maximal energy when tunnelling effects appear, the threshold is called the Mobility-edge.

Anderson localization (AL) was much later (the 70's)[71] interpreted as a universal wave phenomenon that brought various communities (Electronics, Optics, Acoustics, Condensed matter, ...) to theoretically and experimentally search for it. Indeed, AL is now interpreted as an interference effect of waves propagating in a disordered media.

Since then, there are many ways to present what is now called AL. One interpretation refers to the exponential decay of the wave function or the exponential localization of the mode that can be understood from a mathematical point of view.[72] If we consider the Hamiltonian $H = T + V$ where V is an infinite disordered potential and T the kinetic energy, and $\psi_n(\mathbf{r})$ is the eigenfunction of mode n, then the AL regime is reached when for all modes n of the system, the wave function is spatially exponentially localized. Eigenmode n is AL localized for a given realization (it means for a random disordered potential but with the same disorder strength) when $|\psi_n(\mathbf{r})| \leq C_n \exp\left(-\frac{|\mathbf{r}-\mathbf{r}_n|}{2\xi}\right)$ where C_n is a constant and ξ is the localization length independent of the realization. The localization length is an important parameter as it tells how wide the mode is. We easily understand that if all eigenmodes are spatially disconnected they cannot interact with each other, and so there is no transport/diffusion/conduction. A localized mode, by definition, does not participate in the transport. An interesting question arises about the percentage of localized mode needed to be an insulator. Or, in the other way around, how many extended modes are needed to support transport. The AL regime is reached when all modes are localized. The AL phase transition is the abrupt transition between a diffusive regime and an insulator when increasing the disorder of the potential. AL can, therefore, be understood from a transport point of view.

4.2 Experiments

As the AL is a universal wave phenomenon; many fields have been looking for it ranging from quantum optics to acoustics. Even though it was first introduced in electronics for electron localization, the experiment is hard to implement as electron-electron interaction is too difficult to handle.

The first ever observation of AL for a wave was performed in 2008[73] for ultrasound in 3D. They measured the time-dependent transmission and showed non-Gaussian statistics that are related to Anderson localization as it was in agreement with the predictions of the self-consistent theory for AL.

Replacing electrons with particles appeared to be an easier way to see AL. Localization of matter in a BEC was reported recently in the group of A. Aspect in 1D[74] and in Florence,[75] in 3D. In the first experiment, they measured the density profile of the BEC and showed an exponential decay which is a direct measure of the Anderson localization. In the second one, they produced a random potential with two speckle fields, and they measured the energy distribution by measuring the speed of the freely expanding particles after the driving field is turned off. They also managed to measure the mobility edge for the 3D AL of matter waves.

Ten years ago, Anderson localization was reported[76] for microwaves in a quasi-1D system by looking at the statistics of the transmitted intensity. To do so, they managed to distinguish absorption from actual localization.

Since the 90's, the search of Anderson localization of *light* in 3D is a lifetime quest for the experimentalist. Many groups have claimed to observe AL of light.[19,77–80] The most recent one[19] measured the stationary transmitted intensity and showed an exponential decay with the sample size. However, it was later disapproved as the localization was explained by a small residue of absorption. In another experiment,[19,80] they measured the temporal decay of the intensity in transmission and observed a deviation from the classical diffusion what they interpreted as Anderson localization but it was later corrected. In one of the first experiments, they did observe that the transmission in time became very long. This was interpreted as an indication that the mean free path was very small, which would mean that the light was close to localization. It turned out, however, that the long transmission times were due to the light's spending much time inside the scatterers. This meant that the Anderson localization was still out of reach.[81]

We see from this list of experiments that the experimental search of Anderson localization is rich. A diversity of waves are involved (microwave, acoustic wave, matter wave or light) from 1D to 3D. Various methods and observables have been used to observe Anderson localization: direct measurement of the density profile, intensity transmission in time and in the steady-state, statistics on the transmitted intensity, etc. In the specific

case of the localization of light in cold atoms, a debate is still on about existence of a signature of the AL in the mean transmitted intensity, in time or in the stationary regime. Indeed, one important advantage of cold atoms is that they are not subject to absorption but complex physics is introduced due to collective effects.

4.3 Two Criterion for phase transition

4.3.1 Ioffe-Regel criterion

AL is a wave phenomenon. In a dilute regime, a wave propagates between two scatter events without losses and it is well-described by the diffusion equation. This simple picture breaks down when the mean free path (average distance between two scatter events) is on the order of the wave wavelength $\ell \sim \lambda$ and interferences that occur during the scattering process matter. The wave is hence localized in a small region of space. The transition between these two regimes refers to the mobility edge. It turns out that in one and two dimensions, waves are always localized, so the Ioffe-Regel criterion makes sense only for the 3D case. It can be expressed as $k\ell \gg 1$ in the dilute regime and $k\ell \leq 1$ in the localized regime (k is the wavevector). It was introduced in the work of A. F. Ioffe and A. R. Regel in 1960[82] for infinite mediums.

According to the Ioffe-Regel criterion (1960), the diffusion constant tends to zero in the limit of a very strong scattering regime ($\ell \sim \lambda$). The Anderson localized regime can appear at a finite scattering strength, where the diffusion constant becomes zero. It can be explained by the existence of scattering paths that follow a loop and return to the same scatterer. Those loops are more likely to appear in the strong scattering regime which is where diffusion constant is reduced.

4.3.2 Thouless criterion

An important step was done by Thouless, 1974, 1977 and Wegner, 1976, when they looked at the Anderson localization scaling with the sample size L whereas the Ioffe-Regel model holds for an infinite medium. The *Thouless number*, introduced in,[83] is a dimensionless number defined as $g(L) = \frac{\Delta E(L)}{dE(L)/dN}$. It is important to understand that even if the *Thouless number* is usually called dimensionless conductance, it is not directly related to the conductance. The scaling theory of localization developed by Abrahams, Licciardello and Ramakrishnan (1979) showed that near the localization, the dimensionless conductance g is the only important parameter. They showed that in one and two dimensions there is no phase transition as the system is always localized, whereas in three dimensions there exists one transition.

4.4 Theoretical work

Here we present some recent theoretical results on the localization of light. The oldest method to study AL is based on the scaling analysis introduced in.[84–86] A fundamental breakthrough was done in 1979[83] when the link between a dimensionless parameter (called Thouless number) and the energy levels was explained. This relation is really useful when applied to the coupled-dipole equations, what gave rich results in the past decade. The scaling analysis has been refined by focussing on the subradiant modes as the long lifetime modes have been shown to be more likely localized.[47] It has been shown that a phase transition between a diffusive to a localized regime exists when a scalar model of light is considered[34,40,47,48,66] whereas it disappears when the vectorial behaviour of the light is taken into account.[34,47] Moreover, introducing an intense magnetic field allows reaching a localized regime.[49,87] Until this year, it was thought that the AL phase transition might exclusively be a density effect but then an asymmetry between red and blue detuning was observed.[48,49]

5 ANDERSON LOCALIZATION WITH CONTINUOUS MODEL

We here perform a scaling analysis using both the microscopic and the continuous model. It will give us more elements to understand the role of the disorder and the subradiance on the Anderson Localization. We have shown in the previous Part.II that the continuous model describes subradiance even-though it does not contain disorder. However, it has been shown that localization comes from long lifetime modes.[88] The question is: do those long lifetime modes that are localized are subradiant modes or are they independent? The MF model is appropriate to answer this question as it does not contain disorder so we do not expect localization. It would mean that the localization is due to long lifetime modes independent than the subradiant ones.

5.1 Thouless number and scaling function for localization of light

The Thouless number was originally introduced in electronic,[83,86] for a conductor cube of size L, in a uniform potential with sufficient irregularity to describe a bulk metal and at zero temperature with the expression:

$$g = \frac{\Delta E(L)}{dE(L)/dN} \quad \left(= \frac{G(L)}{e^2/\hbar}\right), \tag{5.1}$$

g is the Thouless number, also called dimensionless conductance or normalized conductance, $\Delta E(L)$ is the geometric average of the fluctuation in energy levels caused by non-periodic boundaries and $dE(L)/dN$ is the average spacing between energy levels. L is the side length of the cube, e the electric charge and $\hbar$ the normalized Plank constant. The fundamental result of Thouless and al[83] is the link made between the energy levels and the electric conductance $G(L)$. Unfortunately, such a relation does not exist for light propagation through a 3D disorder medium as the conductance is not defined. In one and quasi-one dimension, the conductance can be linked to the average transmission through the channels.[76,89–94] Anderson localization, from its most fundamental aspect, is a wave phenomena and has strong similarities between electrons and photons. Hence, the Thouless number is usually interpreted by the community as a normalized conductance even for light. From (5.1) we observe that the Thouless number is a function of the system size L what allows to define the scaling function $\beta(g(L)) = \frac{\partial \ln(g(L))}{\partial \ln(L)}$. This function is fundamental and it is used to distinguish the localized regime $\beta < 0$ from the dilute regime $\beta > 0$ in the thermodynamic limit. It is illustrated in Fig.17 extracted from[83] where we see that in dimension strictly lower than two, the system is always localized where, in 3D a phase transition exists. Another representation of the scaling function is shown in Fig.20a for β as a function of $\log(g)$. The scaling function and the Thouless number serve as a basis for several theoretical works on Anderson localization.[34,66,83]

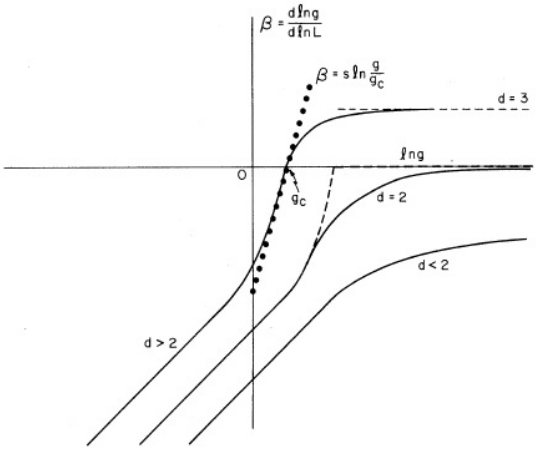

FIG. 1. Plot of $\beta(g)$ vs $\ln g$ for $d>2$, $d=2$, $d<2$. $g(L)$ is the normalized "local conductance." The approximation $\beta = s\ln(g/g_c)$ is shown for $g>2$ as the solid-circled line; this unphysical behavior necessary for a conductance jump in $d=2$ is shown dashed.

Figure 17 – Scaling function plotted vs the logarithm of the normalized conductance.

Source: Adapted from ABRAHAMS et al.[83]

Let us now present the Thouless number as it is defined in the localization of light community[34,66]

$$g = \frac{\delta\omega}{\Delta\omega}. \tag{5.2}$$

We have defined the average lifetime as $\delta\omega^{-1} = \langle 1/\gamma_n \rangle$ and the average spacing of nearest eigenfrequencies as $\Delta\omega = \langle \omega_{n-1} - \omega_n \rangle$ ($\langle \cdots \rangle$ corresponding to the average over the modes n). We remind that eigenvalues are defined as $\lambda_n = \gamma_n + \imath\omega_n$, see Ch.1.3, where ω_n is the energy shift of mode n and γ_n is the linewidth of the energy level of mode n, both normalized by $-\Gamma/2$.

The denominator of the Thouless number, $\Delta\omega = \langle \omega_{n+1} - \omega_n \rangle$ is defined as in (5.1), as the mean spacing between energy levels. However, the numerator $\delta\omega^{-1} =< 1/\gamma_n >$ is defined as the inverse of the averaged inverse of its original definition. Indeed, the mean of fluctuation in energy levels might be simply defined as $\Delta E(L) =< \gamma_n >$. The definition used in the optic community gives a strong weight to the subradiant modes, which are expected to be responsible for Anderson localization.[34,66]

The dimensionless conductance is hence the ratio between the average of the inverse decay rates over the mean of the energy shifts spacing. For the microscopic model, this definition is well established as there are a finite number of modes N. However, as mentioned in Sec.2.1, the continuous model has an infinite number of eigenvalues that does not allow the numerical computation of the average. Hence, it is necessary to introduce a selection rule for the eigenvalues. We already argued about this question in Sec.2.3 and showed that as n and j increase, eigenvalue $\lambda_{n,j}$ becomes more and more subradiant and

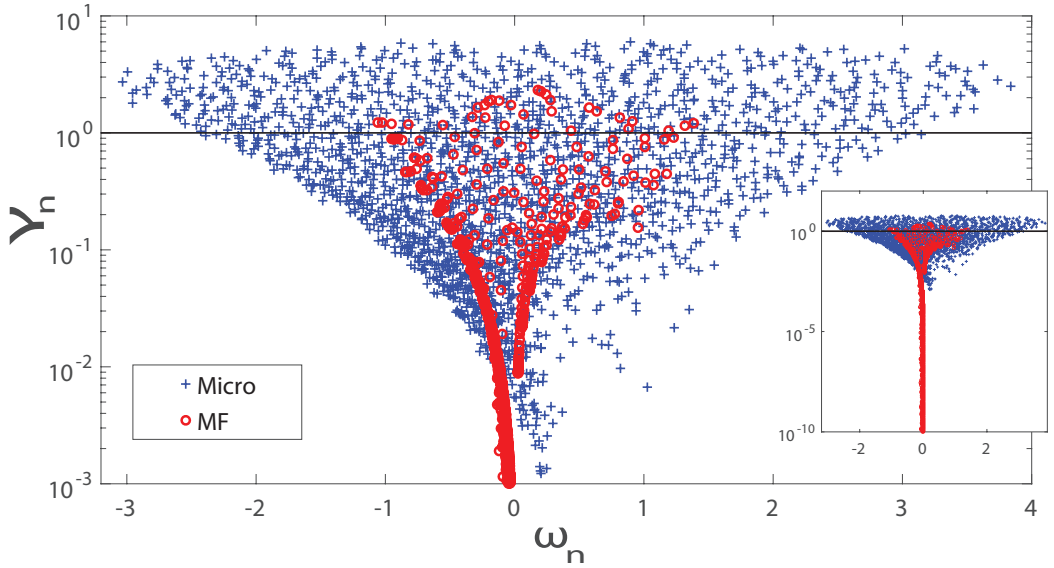

Figure 18 – Eigenvalues in the complex plane $\lambda_n = \gamma_n + \imath\omega_n$ for the microscopic (blues crosses) and continuous (red circles) models. Simulation realized with a Gaussian cloud of $N = 2000$ particles and $\sigma \approx 12$ ($b_0 \approx 28.4$), at resonance ($\delta = 0$).

Source: By the author

the decay rate $\gamma_{n,j}$ goes arbitrarily close to zero, as one can see in the inset of Fig.18. We concluded that selecting modes with $n > 1.5k_0R$ was enough to capture the physics. We need to define here a similar selection rule that does not impact the scaling analysis. First, we consider a fixed integration step h so the range of the index j is fixed, from 1 to H. Then, we introduce a cut-off C on the lifetimes, so that we compute all the eigenvalues that verify $\gamma_{n,j} > C$. Let us define N_m the final total number of eigenvalues selected. The scaling analysis is then realized for a given C.

How g behaves with N_m? First, we look at the denominator, $\Delta\omega$. As we can see in the inset of Fig.18, the quantity $\max(\omega_n) - \min(\omega_n)$ will not be modified by considering higher order modes. Indeed, the maximum and minimum of the energy shift are reached for low values of n (i.e., the modes with large lifetimes have energies close to zero). Finally, the denominator of the Thouless number will decrease inversely with N_m: $\Delta\omega = (\max(\omega_n) - \min(\omega_n))/N_m \propto 1/N_m$. The numerator of g can be developed as $\delta\omega = 1/\langle 1/\gamma_n\rangle = N_m/\sum_{n=0}^{N_m} 1/\gamma_n$. We take a simple example: we add one eigenvalue of decay rate $\gamma_{N_m+1} = 10^{-5}$ in the set of eigenvalues, the numerator of $\delta\omega$ will increase by one whereas the denominator will increase by 10^5. Hence, we clearly see that introducing more subradiant modes will strongly decrease g. To illustrate the above discussion and in order to understand the influence of the eigenvalues selection's rules, we represent, Fig.19, the Thouless number and scaling function for three different selection's rules $C = 10^{-14}$, 10^{-10}, 10^{-5}: we select all the eigenvalues with $\gamma_{n,j} > C$. We see that

decreasing the cut-off, *i.e.* increasing N_m, translates all the curves (as justified above) but does not change the slope of $g(k_0R)$. Hence, it will not change the phase transition limit. So, we can consider an arbitrary value of C keeping in mind that the numerical limitations are of 10^{-14}.

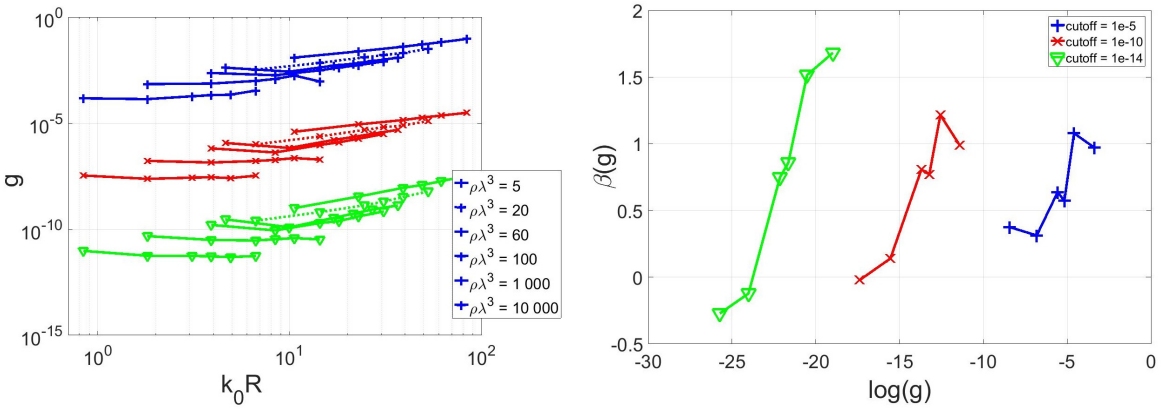

Figure 19 – Scaling function β for the continuous model with a uniform density $\rho = N/V$. Blue crosses : $C = 10^{-5}$, Red crosses: $C = 10^{-10}$, Green diamond : $C = 10^{-14}$. (a) each line represents one fixed density, the dash line is for $\rho\lambda^3 = 20$ where the transition appears for the microscopic model. (b) the scaling function for three values of the cutoff. Simulations realized for a particle numbers $N = [100\ \ 5000]$.

Source: By the author

The physical set-up considered in this part is the same than in Part.II except that we use a uniform density distribution $\rho = N/(\frac{4}{3}\pi R^3)$ where N is the number of atoms and R the radius of the sphere. There is no exclusion volume introduced. The curves $g(k_0R)$ are realized by fixing the number of atoms N and by varying the radius of the cloud R.

5.2 Comparison of the two models

In the literature, several studies have been done using the Thouless number and the scaling function using the microscopic model, showing that it exhibits a phase transition for scalar light ($\rho\lambda^3 \sim 22$) and no phase transition with vectorial light.[34,47,66] First, we reproduce in Fig.20a the results found in the literature[34] where, for $\rho\lambda^3 \sim 22$ and a scalar light model, the slope of $g(k_0R)$ was shown to change sign, it is equivalent to β crossing zero, which is a signature of a localization transition. A similar analysis for the continuous model and a cut-off of $C = 10^{-10}$ is presented in Fig.20b. The scaling function $\beta(g)$ stays greater than one for all the densities except for two values $\rho\lambda^3 = 5.10^4,\ 10^5$ where the slope of $g(k_0R)$ becomes negative. However, this regime is not relevant for our study: it corresponds to very small clouds, much smaller than a wavelength $k_0R \ll 1$, so it cannot be used to study the thermodynamic regime. We can conclude from Fig.20 that

the microscopic approach contains a phase transition whereas the continuous approach does not, in a scalar light approximation. The main difference between the two models is that the microscopic approach contains disorder where the continuous one does not. Those results are expected since the disorder is at the origin of the Anderson localization phase transition.

Moreover, an important point is that the continuous model does not describe Anderson localization even though it contains subradiance, as we showed in the previous Part.II. In particular, we have shown that very long lifetime does not imply localization as it was thought by the community not so long ago. It is an interesting result as it definitely shows that the long lifetime modes that are responsible for localization are different modes than the subradiant ones. It is thus important to distinguish the localized modes from the subradiant modes what is a new concept in the community. In other words, temporal signatures do not appear to be a proper observable to detect light localization. In the next

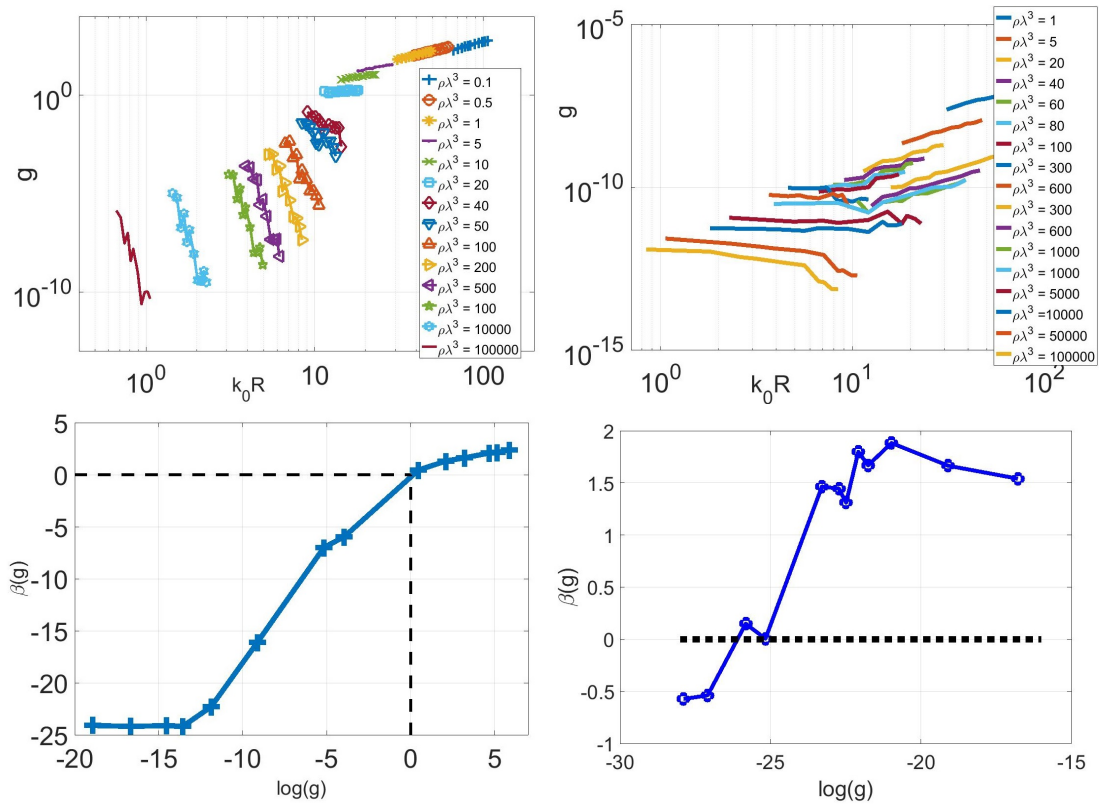

(a) Microscopic (b) Continuous, $C = 10^{-14}$

Figure 20 – g on the two figures above and $\beta(g)$ on the two figures below. The microscopic model on the left (a) and the continuous one on the right (b) with a $C = 10^{-14}$. I have used a Scalar light and uniform distribution so $b_0 = 3N/(k_0R)^2$, $C = 10^{-14}$ for the continuous model.

Source: By the author

part Part.IV we will however show that fluctuations may be a good observable to probe

the Anderson localization phase transition.

5.3 Exclusion volume

In this section, we investigate the impact of an exclusion volume on localization in the microscopic model. Indeed, localization is reached at large densities when pair-physic mode appear. We want to understand if those pair-physics modes are responsible to the localization. Moreover, introducing an exclusion volume decreases the disorder of the system as we introduce more constraints. An exclusion volume $\frac{4}{3}\pi d^3$ is introduced by implementing the following condition

$$\forall(i,j) \;\; k_0 r_{i,j} > d, \tag{5.3}$$

where $r_{i,j} = |r_j - r_i|$ is the distance between atom i and atom j. It minimizes, in particular, the presence of pairs physics.

We present in Fig.21, the results of simulations realized for a uniform spherical cloud of radius R, in the localized regime $\rho\lambda^3 = 40$ (or $\rho/k_0^3 = 0.16$). Fig.21a represents the spectrum $\lambda_n = \gamma_n + \imath\omega_n$ for $k_0 R = 6.67$, using four values of the exclusion distance $d = 0, \;\; 1, \;\; 1.3, \;\; 1.5$, and for 50 realizations. We observe that increasing the exclusion volume removes the subradiant eigenvalues in the right tail and the superradiant modes with negative energy shifts. An interesting observation is that a gap in energy shift (for subradiant eigenmodes) appears. It is so far only observations and they are not properly understood.

Then, we do a scaling analysis, Fig.21b, where we represent the Thouless number $g(k_0 R)$ as a function of the cloud size for four values of the exclusion volume. We clearly see that the slope of g increases as d increases. It can be interpreted as a decrease in the strength of localization. For large d ($d = 1.3$ and $d = 1.5$), the slope of $g(k_0 R)$ stay at zero and do not become positive. Indeed, for large enough exclusion volume, localized modes cannot survive as particles in a *small* volume cannot exist. It is also interesting that decreasing localization by increasing the exclusion volume makes the slope of $g(k_0 R)$ fall on zero whereas it has been shown above that it becomes positive by decreasing the density.

5.4 Phase Transition Exponent

We have seen in Sec.5.2 the existence of a phase transition in the microscopic approach for a scalar light model. Now, we are going to characterize this transition by computing the phase transition exponent as done by Skipetrov et al.[66] It is important to classify the phase transition critical exponents.

We perform the same analysis as in Fig.20a, but focused around the phase transition $\rho\lambda^3 \sim 22$ and we show the scaling function Fig.22. The phase transition exponent is

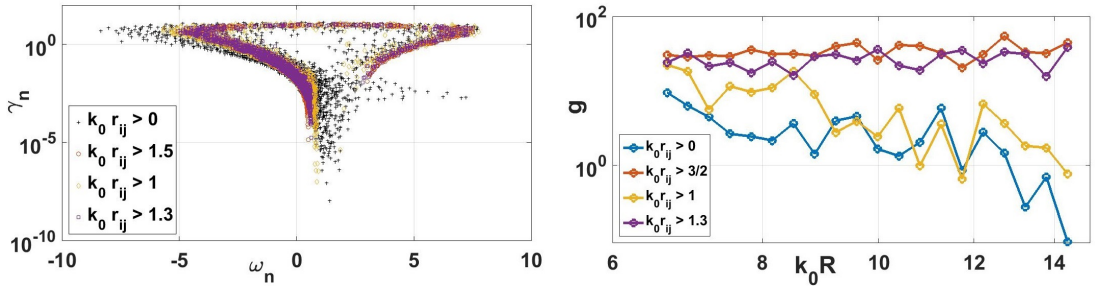

(a) Spectra for $k_0 R = 6.67$. 50 realizations. (b) Thouless number g as a function of $k_0 R$.

Figure 21 – Uniform sphere of radius R and density $\rho\lambda^3 = 40$. Four values of the exclusion volume is represented: $k_0 r_{i,j} > d$ with $d = 0,\ \ 1,\ \ 1.3,\ \ 1.5$.

Source: By the author

extracted as follow: we fit the curve $\beta(\log(g))$ of Fig.22 with a function $\beta(x) = A(x - x_c) + B(x - x_c)^2$ where x_c is the phase transition point defined by $\beta(x_c) = 0$. Then the critical exponent is defined as $\nu = 1/A$. We obtain $\nu = 0.95$ which is different from the values found in[66] where $\nu \in [1.52, 1.72]$. This exponent is useful to classify the kind of phase transition. As we can see on the figure, the curve is not perfectly smooth, and it has

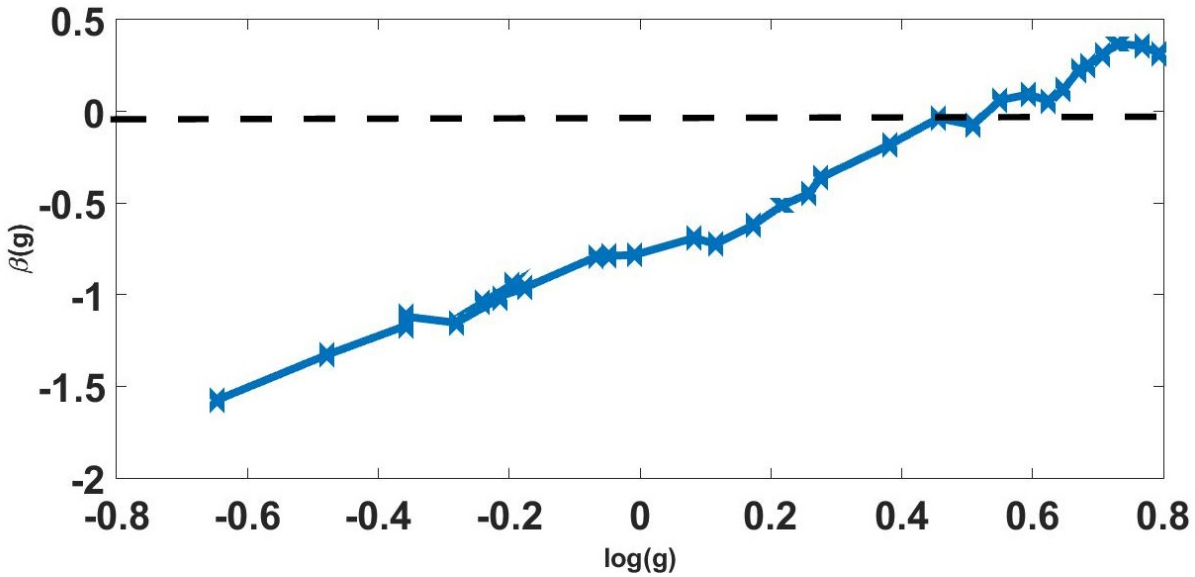

Figure 22 – Scaling function zoomed on the transition.

Source: By the author

been realized with a low number of realizations (~ 10) so the errorbar are really important. It explains the discrepancy with the other value present in the literature. We would need better statistics to go further in this direction.

5.5 Conclusion

We have here presented a preliminary work on the Anderson localization phase transition for light in 3D in atomic media by performing a scaling analysis. We have recovered the results of the literature showing that there is a localization of light phase transition for the scalar description of the light. Moreover, we confirmed that the continuous approach, despite it contains long lifetimes, does not exhibit such a transition as it does not contain disorder which shows that subradiance is not automatically associated with localization.

Part IV

Intensity fluctuations for Anderson localization

6 INTRODUCTION

In the previous chapter, as several theoretical works before,[34,47,48,66] we studied the Anderson localization by performing a scaling analysis,[84–86] i.e., we study the eigenvalues of a coupling matrix (or eigenvalues of a Hamiltonian). It gave interesting contributions like the absence of localization for a vectorial light model,[34,47] the existence of an Anderson localization for a scalar light[34,40,66] and a vectorial light with an intense magnetic field[87] and the existence of a phase transition in the $(\rho\lambda^3, \delta)$-plane.[48,49] Unfortunately, the scaling function, as well as the participation ratios, are not physical observables so the associated results cannot be checked. In this part, we show that the intensity fluctuations are an observable that exhibits the same transition than the AL phase transition.

The light emitted by a random media shined by a laser is a bright subject of research as the cooperativity gives rise to interesting physics. In the steady-state regime,[15,95,96] the incoherent (off-axis) and coherent (forward direction) transmission are modelled, in absence of localization, by respectively Ohm's law for photons and Beer-Lambert law.[27,39,62] Ohm's law for photons describes the scattering of the light propagating through a random medium and it is well-described by the radiative transfer equation (RTE)[27] in the low-density regime. Divergence from this law can occur for dense clouds as discussed in Sec.8.1. In the single scattering regime ($b(\delta) < 1$) the incoherent transmission linearly scales with b, whereas in the multiple scattering regime ($b(\delta) > 1$), it follows a Lorentzian function in δ.[27] Beer-Lambert law rather describes the diffraction of light by a continuous index distribution, and is well-described by the continuous model introduced in the first chapter of this thesis.[40] Another manifestation of interferences is observable in the backscattering direction, where a narrow cone with a maximum intensity, two times greater than the background appears and it is called CBS (coherent backscattering) or weak localization. It is a signature of interferences between reciprocal trajectories, which the RTE is not able to explain as it does not account for interferences, yet the couple-dipole model is. This cone is stronger in the multi-scattering regime where reciprocal trajectories are more probable to appear.[27,51,97]

Yet these static phenomena did not present signatures of Anderson localization. The community has also been interested in the dynamical case, *i.e.*, the diffuse intensity in time once the driving laser is switched off, that also reveals interesting physics like radiation trapping and super- and subradiance. This procedure has been theoretically[40] and experimentally used in the dilute regime.[7,18,35] Subradiance is related to long lifetime mode what was first thought to be a signature of localized modes.[19,80] It has been shown that it is, in fact, an interference effect not related to disorder.[40] Despite it has been a very active field, there is no clear measurement of Anderson localization of light up to date. In

the Ch.8, we discuss open questions about the observation of AL in the mean intensity. First, we consider the steady-state regime that contains not understood observations. Then we discuss a recent theoretical work about long lifetimes in the radiated intensity.[88]

The most practical step to observe AL in 3D scattering systems is to look at the mean of the radiated intensity as it was done[19,80] as it is the most accessible experimental observable. However, the transition reported in previous experiments have not convinced the community as they might be explained by absorption. Finally, so far, none of those experiments or theoretical works allow concluding on the existence of an AL phase transition in the mean intensity. It is thus natural to go one step ahead and to investigate the fluctuations of the intensity. It is an approach equivalent to looking at the first and second moment of a statistical variable, where the variable is here the far field intensity in the speckle field. The speckle pattern is produced by the interferences between coherent waves crossing a disordered medium. It has been investigated since Newton but attracted again some attention with the invention of the laser. One important result is that the probability distribution function (PDF) of the speckle follow a Rayleigh law $P(I) = \exp(-I)$ (or Rayleigh distribution), (Goodman, 1975[98]). Later, it was observed a deviation from the Rayleigh law in transmission and for strongly scattering system.[99,100] It led to a competitive theoretical work to explain this non-Rayleigh distribution[101–103] and was later expressed as a function of the normalized conductance g. This interesting result links the intensity statistics to the Thouless number, which is used for the scaling analysis, and therefore to the quantification of AL through the intensity statistics.[90–92]

The aim of this work is to exhibit an Anderson localization phase transition in the statistics of the stationary radiated intensity. We first show that no phase transition is observed in the mean intensity. Then we bring our attention to the intensity fluctuations and especially the variance of the intensity and we compute the conductance. We observe a transition with the detuning-density parameters that we link to an Anderson localization phase transition by comparing it to existing results like the detuning-density dependency of the phase transition, the scaling with the conductance, the scaling of the variance-conductance. Finally, the absence of phase transition for a vectorial light model of the light is also investigated by introducing a magnetic field.

We present Rayleigh statistics in more details in Sec.9.1. Then we illustrate a non-Rayleigh distribution in Sec.9.2 and we link it to an Anderson localized regime by using the parameter g. Finally, we extend this study to a full detuning-density dependence in the scalar light approximation and the vectorial light model.

7 INTENSITY STATISTICS

In order to perform the intensity statistics analysis, we consider the same system as in the previous parts that we solve by using the coupled-dipole model. We study the interaction between a laser and a cloud of two-level cold atoms. Atoms are characterized by $N \gg 1$ point scatterers of fixed position $\mathbf{r}_j$, randomly distributed with density $\rho(\mathbf{r})$, transition linewidth Γ (also called single atom decay rate), the dipole momentum d and the normalized Planck constant $\hbar$. The medium has a characteristic size L (for instance the cube side length). The optical set up is illustrated in Fig.23.

As already showed in Sec.1.1.2, the coupled-dipole equation for the atomic dipoles in the low-intensity regime is:

$$\frac{d\beta_j}{dt} = \left(\imath\Delta - \frac{\Gamma}{2}\right)\beta_j - \imath\frac{d}{2\hbar}E_{laser}(\mathbf{r}_j) - \frac{\Gamma}{2}\sum_{m\neq j}\frac{\exp(\imath k|\mathbf{r}_j - \mathbf{r}_m|)}{\imath k|\mathbf{r}_j - \mathbf{r}_m|}\beta_m. \tag{7.1}$$

The resolution of (7.1) is discussed Sec.1.1.3. In the stationary regime β_j reach a constant values so $\frac{d\beta_j}{dt} = 0$ and the equation (7.1) can be solved by inverting an $N \times N$ matrix what remains time demanding. In order to obtain the best statistics, we perform typically up to 10000 realizations for each set of parameters.

In this chapter, and differently from the plane wave that has been used so far, we use a monochromatic Gaussian beam, as it is illustrated in Fig.23, the electric field of

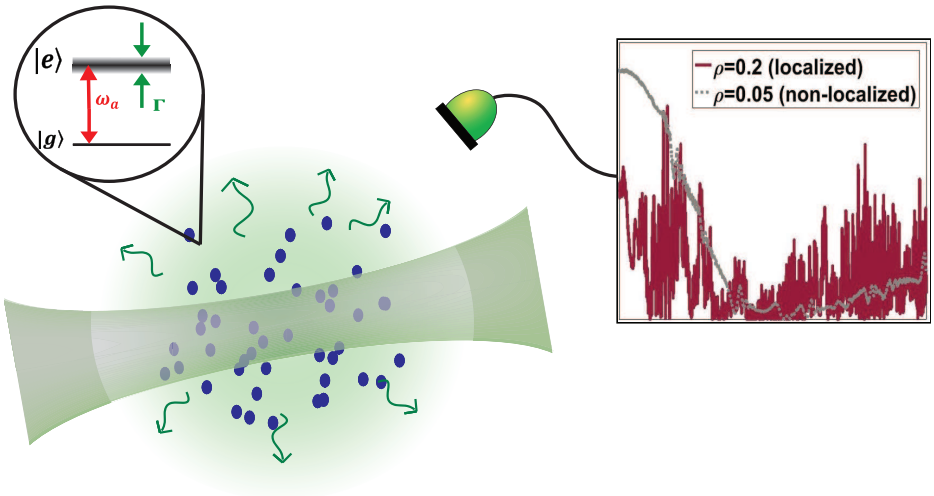

Figure 23 – Set up of the system: Gaussian laser beam (Green), atoms (blue spots), scattered light (green arrows), two-level atoms (in the circle inset) and an example of the measurement of the intensity in time.

Source: By the author

which is:

$$E_{laser}(X,Y,Z) = E_0 \frac{W_0}{W_z} \exp\left(-\frac{X^2+Y^2}{W_z^2}\right) \exp\left(\imath\left(kZ + k_0\frac{X^2+Y^2}{2R_z} - \phi_z\right)\right), \quad (7.2)$$

with E_0 the electric field at the origin, W_0 the waist, $\mathbf{k} = k\hat{\mathbf{z}}$ ($k = 2\pi/\omega_0$) the wavevector, $W_z = W_0\sqrt{1+(Z/z_R)^2}$ the spot size parameter, $R_z = Z(1+(z_R/Z)^2)$ the radius of curvature, $\phi_z = \arctan(Z/z_R)$ the Gouy phase and $z_R = \pi W_0^2/\lambda$ the Rayleigh range. We set a fixed laser field $E_0 = 1$ and we set the laser waist to $W_0 = L/4$. We stay in the linear regime (keeping a saturation parameter $s(\Delta) \ll 1$). The waist is chosen lower than the medium size L in order to have most of the laser intensity passing through it. Thus, we avoid border effects and single scattering introduced on the edge of the medium. Indeed, P.Weiss and al showed[7] that, for a cold atomic cloud, the single scattering ratio is much larger by using a plane wave as a driving laser than a Gaussian beam with a waist much smaller than the typical size of the medium. Indeed, the plane wave populates the single scattering modes that are on the edge of the cloud which a Gaussian beam with $W_0 \ll L$ does not. It explains that the Anderson localization phase transition presented in this part has not been recovered by using a plane wave. Indeed, the modes at the edge of the cloud are not expected to be localized as they exhibit less multiple scattering.
Another element introduced by using a Gaussian beam laser is its divergence angle in the forward and backward propagating direction that is inversely proportional to the waist W_0 and so forth to L. As we will see later, this forward angle is not appropriate to look at statistics of the intensity as in this direction the scattered field is mostly coherent scattering, which suppresses fluctuations. Finally, we have verified that $W_0 = L/4$ is a good compromise between boundary effects and beam diffraction.

We define the intensity at position $\mathbf{r} = (r,\theta,\phi)$, in spherical coordinates, by $I(\mathbf{r}) = \frac{1}{2}\epsilon_0 c|E_{tot}(\mathbf{r})|^2 = \frac{1}{2}\epsilon_0 c|E_{sc}(\mathbf{r}) + E_{laser}(\mathbf{r})|^2$. E_{laser} is the laser field defined in (7.2) and E_{sc} is the scattered field in the far field limit defined in Sec.3.1.

$$E_{sc}(\mathbf{r}) = -\frac{\hbar\Gamma}{2d}\frac{e^{\imath kr}}{kr}\sum_{j=1}^{N} e^{-\imath k\hat{\mathbf{r}}.\mathbf{r}_j}\beta_j, \quad (7.3)$$

with $\hat{\mathbf{r}} = \mathbf{r}/|\mathbf{r}|$ and $\hbar$ is the normalized Plank constant and d the transition dipole moment. Note that in the backward direction ($\theta > \pi/2$), the Gaussian beam is not considered when computing the radiated field, as it propagates in the opposite direction. So, we set $E_{laser}(\theta \subset [\pi/2\ 3\pi/2]) = 0$ in the reflection plane. Moreover, we stay in the far field regime by computing the intensity at the distance of observation $r_o = 250L$.

We consider as *statistic variable* the normalized intensity (*i.e.* divided by its average) $\tilde{I} = I/\langle I\rangle$ where $\langle\ldots\rangle$ stands for the average over many *realizations*. In order to produce different *realizations* we compute the intensity for either different *disorder realizations* or for different values of the azimuthal angle ϕ. We call *disorder realization* the measure of the intensity with a different spatial distribution of the atoms in the cloud and we call

realization, one measure of the intensity. The physics like multiple or single scattering depend on θ so we work at a fixed polar angle. Hence, realizations can be performed over the disorder and/or over the azimuthal angle ϕ, which will be discussed in Sec.9.6.

8 MEAN INTENSITY

Before moving to the intensity statistics study, we here look at the mean intensity. If the mean intensity contains signs of localization it might not be necessary to look at the fluctuations as the mean intensity is easier to experimentally measure. We presented in the introduction of this part the experiments that searched, without success, for AL through the mean intensity. A recent theoretical work[88] suggests that we can monitor the trapping of light by observing the long-time decay of the fluorescence. This result is discussed in Sec.8.2. In Sec.8.1, we comment on divergence from Ohm's law at high densities.

8.1 Stationary regime

Let us first look at the incoherent transmitted intensity. In the thesis of T. Rouabah[42] and Ref.,[39] the transmission through a uniformly distributed sphere illuminated by a Gaussian laser was studied numerically. It was shown that Ohm's law is well-described by the RTE or a random walk model that ignore coherences and interferences. However, when using the coupled-dipole model, a divergence from the Ohm's law was observed at large densities. It is not explained but the relative increase of the diffuse transmission as compared to Ohm's law is not consistent with a decrease of the diffusion coefficient as would be expected from Anderson localization. We have recovered the same kind of behaviour for a cubic cloud, see in Fig.24. In our simulations as well as in T. Rouabah's, this effect appears independently on the detuning and also on resonance, which suggests that it is not an AL effect.

8.2 Subradiance rate

A recent theoretical work[88] showed a different behaviour of the long lifetime of the intensity in the two regimes (localized and non-localized), which was explained as light trapping. However, the authors do not work at a fixed resonant optical thickness so this effect might be explained by subradiance[7,40] that linearly scales with b_0,[18] rather than localization. In order to go further in this discussion, we look at the behaviour of the mean intensity in time $\langle I(t)\rangle/\langle I(t)\rangle_{t=0}$ as a function of the density. The mean is here performed by computing $I(t)$ for different disorder realizations, so $\langle I(t)\rangle$ is a function of time. We charge the system by turning on the laser for a long time ($50\Gamma^{-1}$), and we monitor the diffuse intensity when the laser is switched off at $t = 0$. It is the same procedure as in Part.II that has been intensively studied in the dilute regime. In Fig.25, we plot the subradiant rate τ_{sub} computed by fitting the curve $\log\left(\langle I(t)\rangle/\langle I(t)\rangle_{t=0}\right) = A_0 - (1/\tau_{sub})t\Gamma$ on a time-window that refers to $\langle I(t)\rangle/\langle I(t)\rangle_{t=0} \in [10^{-2}\ 10^{-4}]$. Despite large fluctuations, we recover that the subradiant rate remains constant for fixed b_0 and such for the two

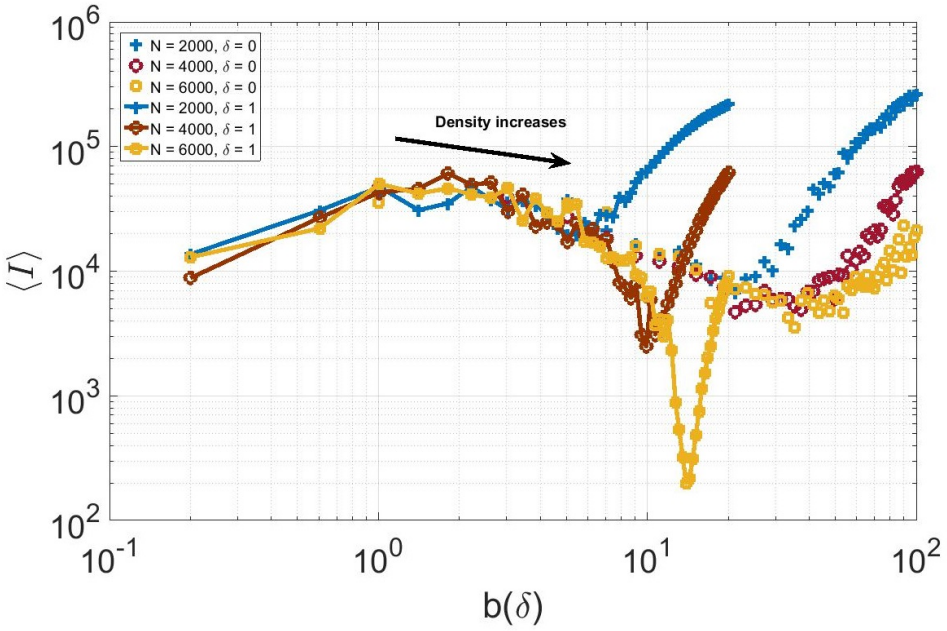

Figure 24 – Mean transmitted intensity in the stationary regime as a function of the optical thickness, for different number of atoms N and detuning δ. The arrow indicates the direction where the density increases while staying on the same curve. The geometry of the cloud is a uniform cube of side length L driven by a Gaussian laser with waist $W_0 = L/4$. The intensity $I = |E_{sc} + E_{laser}|^2$ is computed in direction $(r_o = 250L, \theta = \pi/6)$ and averaged over 40 realizations.

Source: By the author

regimes: non-localized (low density) and localized (large density). Moreover, the value at the origin of the linear regression A_0 is constant, whereas the variance increases. It shows that looking at the long lifetime behaviour of the radiated intensity is not enough to exhibit a transition.

8.3 Conclusion

In this chapter, we have focused our attention on the subradiant rate in order to show that there is, so far, no proof of an AL phase transition in the mean intensity. It justifies going further in the statistical study of the intensity which means looking at the fluctuations.

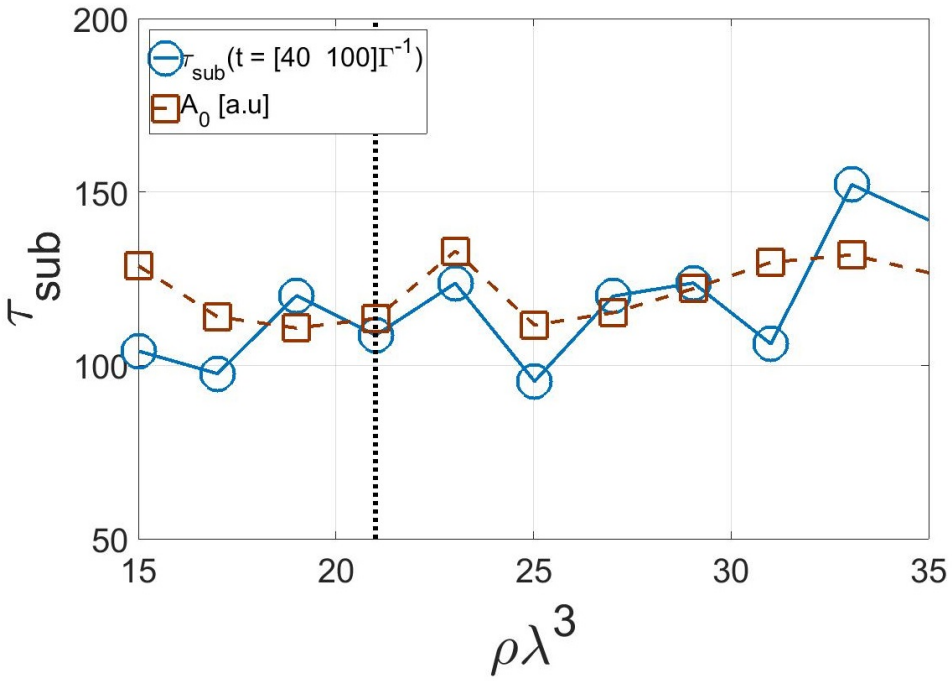

Figure 25 – Subradiant slope fitting as a function of the density. Atoms are uniformly distributed in a cube of side length L. Intensity is computed over 100 realizations in direction $\mathbf{r_o}$ where $r_o = 250L$, $\theta_o = 75°$ and $\phi = 0$. We use a Gaussian laser with waist $W_0 = L/4$ and detuning $\delta = 0.83$ and the optical thickness is fixed at $b_0 = 20$. A_0 (red squares dashed line) is shown in arbitrary units and the subradiant rate (blue circles and full line) is computed for $t = [40\ \ 100]\Gamma^{-1}$.

Source: By the author

9 INTENSITY FLUCTUATIONS

We saw in the previous chapter Ch.8 that no signature of phase transition related to Anderson localization has been found in the mean intensity. Hence, one may choose to study the intensity fluctuations, where the first moment would correspond to the variance. The variance measures how far a statistical variable spreads out from its average values. In our case, the variable is the steady-state diffused intensity and the variance describes its fluctuations from one realization to the other. The intensity fluctuations have been and still are a subject of interest. It is mainly studied, experimentally, through which is called the speckle that can, for instance, provide information about the nature of the light source (spatial and temporal coherence) by computing the autocorrelation function. In this chapter, we study the statistical properties (PDF, variance) of the far-field intensity in order to exhibit a transition. Then we relate this transition to the Anderson localization phase transition by comparing it with already published results.

First, we present the Rayleigh distribution of the speckle statistics and we present theoretical work about the non-Rayleigh statistics done in the 90's. We discuss the PDF of the intensity in the three regimes: the dilute, the localized and the deeply localized regime, and we extract the conductance from those PDFs. Then we investigate the best θ-direction (transmission, reflection) to observe non-Rayleigh statistics. We perform a 2D $(\delta, \rho\lambda^3)$ mapping of the phase transition. We look at the scaling of this transition, we investigate the influence of the azimuthal angle and we use a vectorial model of the light to study the influence of a magnetic field.

9.1 Speckle: Rayleigh and non-Rayleigh statistics

9.1.1 Normal Speckle

When one shines at fixed disordered media like paint with a coherent source, the diffused light draws a random pattern as shown in Fig.26. This pattern is a consequence of the disorder inside the media. It is a result of interferences between all possible paths of the light through it. For instance, the speckle pattern has a characteristic grain size that is related to the characteristic size of the medium L. A statistical analysis of the speckle pattern can be performed in space by integrating the total diffused intensity over all directions or in time by measuring $I(t)$ in one direction. It is subject to theoretical and experimental work[94,98,104–106] and allows to predict the intensity probability distribution and the autocorrelation function. It has been established that the intensity statistics follow a Rayleigh distribution[107] of the form $P(I) = \frac{1}{\langle I \rangle} e^{(-I/\langle I \rangle)}$ that was experimentally observed.[90,99,108] This result can be mathematically derived by considering all the possible paths that a photon can take inside a random medium between an incoming and outgoing

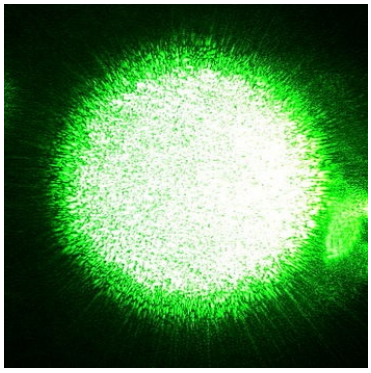

Figure 26 – Speckle pattern.

Source: Available from: <https://en.wikipedia.org/wiki/Speckle_pattern>. Accessible at: 14 March 2019.

direction and by doing the following hypothesis:

- Phases are uniformly distributed in $[-\pi\ \pi]$.
- For a given path, phases and amplitudes are unrelated random variables.
- For two different paths, phases and amplitudes are independent random variables.

and using statistical properties such as the central limit theorem. One example of the Rayleigh distribution is illustrated in Fig.27 for the normalized intensity $\tilde{I} = I/\langle I\rangle$. In the semilog representation, we clearly recover the exponential distribution, as the parameters are chosen in the dilute regime, $\rho\lambda^3 = 5 < 20$.

Those properties for a *normal* speckle (for independent scatterers, for example) are well established, theoretically and experimentally[94,98] in the regime where $g \to \infty$ where there are no correlations between intensities. The parameter g is the dimensionless conductance.[83,85,86] Multiple scattering is thus not essential. The statistical study of the intensity is performed by looking at the first and second moments. The first moment is simply the mean intensity $\langle I\rangle$ that has been investigated in the previous section, Sec.8. Then our attention goes to the second moment, that is, the variance of the normalized intensity $var(\tilde{I}) = \sigma_{\tilde{I}}^2 = \langle\left(\tilde{I} - \langle\tilde{I}\rangle\right)^2\rangle = \langle I^2\rangle/\langle I\rangle^2 - 1 \quad (= g^{(2)}(0) - 1)$[83] where $\tilde{I} = I/\langle I\rangle$. The relation between the variance and the autocorrelation function $g^{(2)}(0)$ is interesting from an experimental point of view as it can be measured experimentally.[109] We remark that for a normalized exponential probability distribution the variance is one. Thus, one signature of the divergence from Rayleigh statistics is the variance deviating from unity. Indeed, if the variance diverges from one it means that the PDF of the intensity is not exponential. The variance may describe the fluctuations of the intensity which we expect to increase at the phase transition due to the appearance of localized modes. Even though it allows to distinguish Rayleigh from non-Rayleigh statistics, the variance does not describe

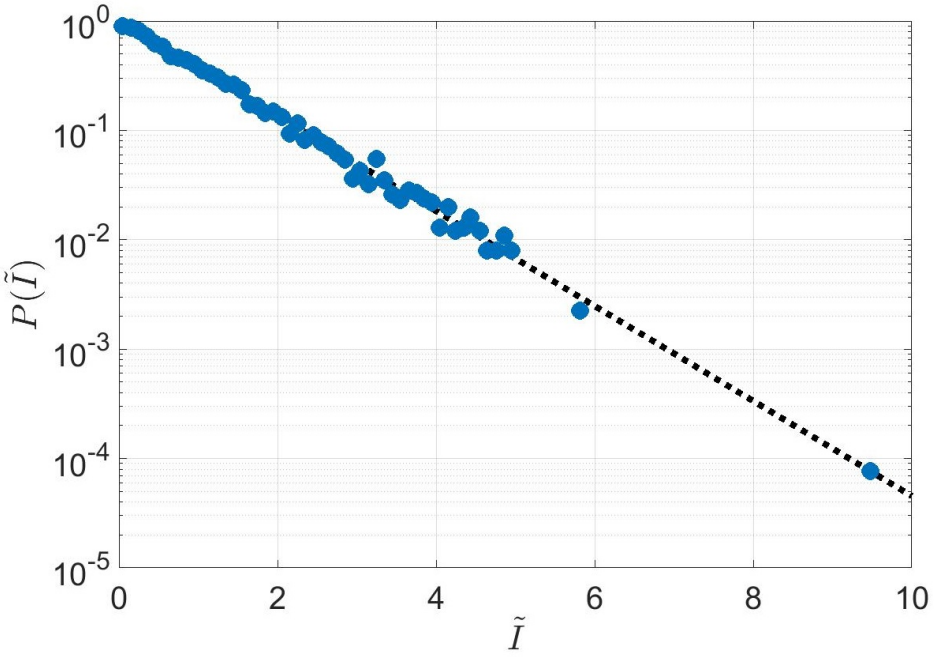

Figure 27 – PDF of the radiated normalized intensity of $N = 684$ atoms uniformly distributed in a cube of side length L with a density $\rho\lambda^3 = 5$, $b_0 = 8.2$ and $\delta = 0$. Intensity is computed in direction $\mathbf{r_o}$ where $r_o = 250L$, $\theta_o = 75°$ and $\phi = 0$. We use a Gaussian laser with waist $W_0 = L/4$. Statistics are done over 10 000 realizations. Blue filled circles are for simulations and the black dashed line refers to an exponential distribution.

Source: By the author

all the information contained in the pdf. The aim of this part is to study how the Rayleigh distribution is modified through the Anderson localization phase transition.

9.1.2 Non-Rayleigh statistics

In a series of papers[76,83,89–94,99,110] , an approach was proposed to show how intensity statistics can deviate from Rayleigh's law. It consists of considering the Feynman trajectories to compute all the moments $\langle I^n \rangle$ and thus recover the PDF. Hence, the Rayleigh law is obtained with the ladder diagrams[111] by summing the contributions of all the non-correlated paths of a wave propagating in a disordered medium and $\langle I^n \rangle = n! \langle I \rangle^n$. However, there are other additional terms that are more difficult to observe and that take into account trajectories with one or more crossings. The probability of higher-order crossings have a no-negligible contribution and $\langle I^n \rangle = f(n) \langle I \rangle^n$ where the function f is discussed in reference.[101] This approach has been intensively studied in the 90's theoretically, numerically and experimentally, after the observation of a non-Rayleigh distribution in 1989.[99] An intense analytical work tried to model this observation. Computing the moment distribution of the intensity probability distribution of the transmitted waves propagating in a disordered medium was first introduced by Shnerb et al. in 1991.[101] He

distinguised bettween the transmission and the reflection and gave an analytical expression of the PDF of the transmitted intensity that depends on the conductance g and the transmission coefficient T in the regime where multiply-crossing Feynman trajectories can be neglected (only one crossing is considered). This initial work was followed by intense discussions[76,83,89–94,99,110] and lead to the general expression of (9.1) that is valid for all values of g.

$$p(\tilde{I}) = \int_{-\imath\infty}^{\imath\infty} \frac{d\,x}{\pi\imath} K_0(2\sqrt{-\tilde{I}x}) \exp(-\Phi_{con}(x))], \tag{9.1}$$

K_0 is the modified Bessel function and the function Φ_{con} has a different expression depending on the beam profile, plane wave or Gaussian beam. For a Gaussian beam:

$$\Phi_{con}(x) = g \int_0^1 \frac{d\,y}{y} \log\left(\sqrt{1+\frac{xy}{g}} + \sqrt{\frac{xy}{g}}\right), \tag{9.2}$$

where g is the dimensionless conductance.[83,85,86] In the large g and low $\tilde{I}$ approximation, and for a plane wave, the equation (9.1) leads to the following expression: (9.3), which will be used only for specific cases mentioned later.

$$p(\tilde{I}) = e^{-\tilde{I}}\left[1 + \frac{1}{3g}\left(\tilde{I}^2 - 4\tilde{I} + 2\right)\right]. \tag{9.3}$$

It shows that the intensity distribution in any direction depends only on one parameter g. g is inversely proportional to the crossing probability of two Feynman trajectories for transmission and to the probability to return to the same channel in reflection. $1/g$ can also be interpreted as the probability for two channels to interfere. Close to Anderson localization g approaches unity and fluctuations increase. Fitting the PDF with expression (9.3) gives access to the value of g. This approach is quite interesting since the conductance is usually used to distinguish the localized from the dilute regime and to exhibit a phase transition by performing a scaling analysis, as was done in Part.III. Indeed, in 3D, the non-localized regime refers to $g \to \infty$, and the localized regime refers to $g \to 0$.

Finally, performing the study of the intensity statistics allows us to compute the variance and the conductance, which are two parameters issued from different approaches that we will use to study the Anderson localization phase transition.

9.2 Phase transition histograms

In the previous section, we saw that the variance is a good parameter to study the intensity statistics and we know[99,100] that a non-Rayleigh distribution can appear in the multiple scattering regime. In order to go further in the understanding of the intensity statistics at the phase transition, we illustrate in Fig.28 the PDF of the intensity. As expected, the PDF (blue points) diverges from an exponential distribution (black dashed line), and it is characterized by a variance much greater than one: $\sigma_{\tilde{I}}^2 = 6.85$. The conductance is computing by fitting the filled blue dots with (9.1) and (9.2) and provides

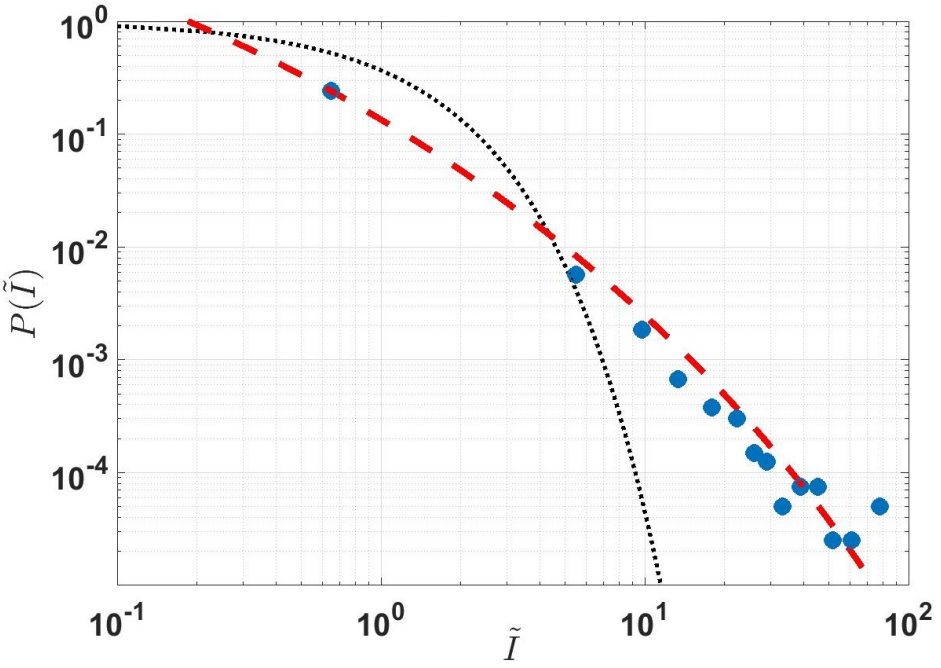

Figure 28 – PDF of the radiated normalized intensity of $N = 6066$ atoms uniformly distributed in a cube of side length L with detuning $\delta = 1$, density $\rho\lambda^3 = 44$. Intensity is computed in direction $\mathbf{r_o}$ where $r_o = 250L$, $\phi = 0$ and $\theta = 75°$. We use a Gaussian laser with waist $W_0 = L/4$. Statistics is done over 10 000 realizations. Blues points represent the PDF for the data, black dash lines is the PDF for an exponential distribution and the long-dashed line is a fitting of (9.3). $\sigma_{\tilde{I}}^2 = 6.85$ and $g = 0.058$ and errorbar of [0.0578, 0.0583] with a binning of 20.

Source: By the author

the value $g = 0.058$ (and 95% confidence of [0.0578, 0.0583]). Note that the histogram depends on the binning and so it impacts the computation of the variance by a fit.

We now consider a system *more localized*, i.e., with a larger density, in order to study how the intensity statistic behaves in the *deep localized regime*. We show in Fig.29, the PDF for a density of $\rho\lambda^3 = 38$ and a detuning of $\delta = 0.5$. The variance is $\sigma_{\tilde{I}}^2 = 1.16$ and the conductance is $g = 12.1$. Surprisingly, those values are similar to those in the non-localized regime. The PDF follows an exponentials law for low intensities $\tilde{I} < 8$ but seems to diverge from it for large values $\tilde{I} > 8$, which is not captured by neither the variance nor the conductance. It is not so surprising that the variance changes of behaviour only at the transition and remains stable in the deep-localized and non-localized regimes. It is a similar behaviour than other phase transitions like the susceptibility in ferromagnetic medium.[112]

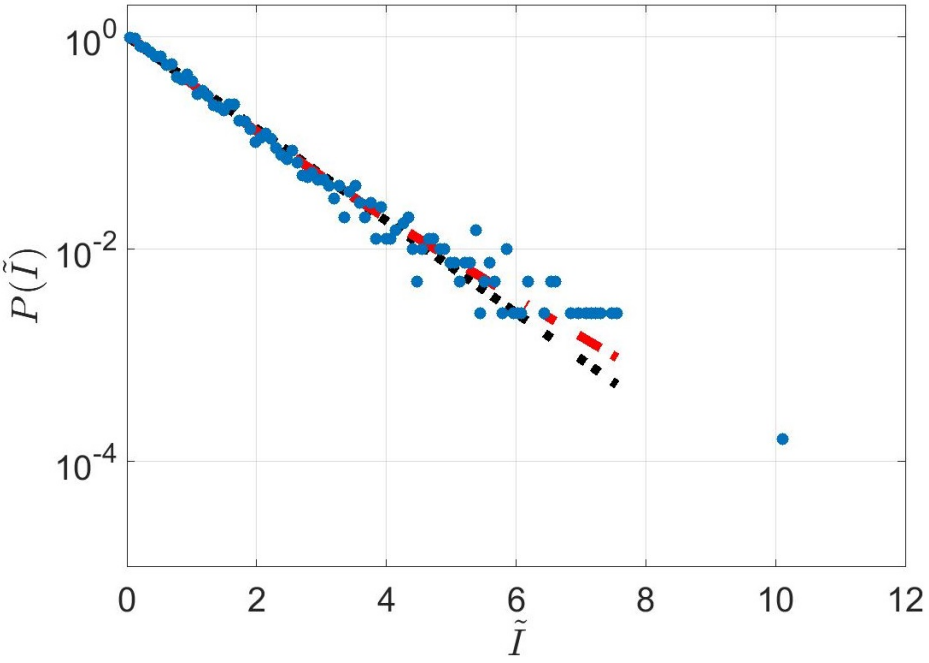

Figure 29 – PDF of the radiated normalized intensity for$N = 5204$ atoms uniformly distributed in a cube of side length L with a detuning $\delta = 0.5$ and $\rho\lambda^3 = 38$. Intensity is computed in direction $\mathbf{r_o}$ where $r_o = 250L$, $\phi = 0$. We use a Gaussian laser with waist $W_0 = L/4$. Statistics are done over 5 000 realizations. Black dash lines is for an exponential distribution and red dash lines is for the fitting with (9.3). Variance is $var = 1.16$ and conductance is $g = 12.0747$ with errorbar of [10.4368, 13.7126].

Source: By the author

9.3 Direction of observation

In this section, we investigate the optima direction to observe the non-Rayleigh distribution. Indeed, (9.1) is independent on the direction. Nevertheless, a wide range of physical phenomena interfere with the interpretations depending on the direction of observation: CBS, Ohm's law, Beer-lambert law, etc. The azimuthal angle ϕ is not treated here and it stays equal to zero but it is discussed in Sec.9.6. We study the intensity statistics in direction $\theta = [0\ \pi]$ for two sets of parameters that refer to the dilute regime, $\rho\lambda^3 = 5$ and the phase transition regime, $\rho\lambda^3 = 44.3$. The phase transition parameters are chosen in accordance with the recent results of reference.[48] In Fig.30, we show the variance as a function of the θ-angle for those two regimes. We remind that the total intensity is computed as $I = \frac{1}{2}\epsilon_0 c|E_{sc}(\mathbf{r}) + E_{laser}(\mathbf{r})|^2$ where E_{laser} is set to zero in reflection and the statistical variable is $\tilde{I} = I/\langle I\rangle$.

First, let us focus on the forward lobe where the variance oscillates ($\theta \approx 0$). In this direction, the intensity is driven by the Mie-scattering theory where the scattered field

synchronizes with the incident laser. While the laser field is constant it explains that the total intensity tends toward a constant and the variance drops to zero. To justify it, we have superposed the variance with the mean intensity (thin lines) to illustrate that the oscillations of the variance perfectly coincide with the oscillations of the mean intensity that have been shown to be the Mie-scattering resonances.[40] The forward lobe is not interesting for our study as it is driven by the Mie scattering theory which is not a disorder effect[40] but due to diffraction. Following the Mie-scattering theory, the forward lobe angle is inversely proportional to the typical size of the cloud ($\propto 1/(k_0 L)$). In order to minimize the forward lobe extension we work with an as large L as possible and we verify, for all results presented here, that we are not in this lobe.

We now turn our attention to the backward lobe where we observe a drop in the variance (it also exists for the blue curve but less significantly what explains that we do not see it on the figure). The abrupt change of density at the surface introduces a change in the refractive index. Due to the change of the index a substantial part of the incoming laser field is reflected. This fraction of the intensity is constant and independent on the disorder realization so it lowers the fluctuations. The larger the change in density, the larger the index change and the more of the field will be reflected. It explains that in Fig.30, the drop of the variance is more important for higher densities. This effect could be minimized by introducing an angle between the laser field propagation direction and the medium surface or by using a curved surface of the medium like a sphere.

If we exclude those two regimes we see that the dilute regime presents a variance equal to one which is a consequence of an exponential probability distribution of the intensity as we see in Fig.27 for the angle $\theta = 75°$. Finally, the interesting part is about the phase transition regime (red dashed lines) where the variance significantly increases in the transmission plane which results from a break of the exponential PDF of the intensity. It is an important result as it shows that the apparition of Anderson localized modes at the phase transition changes the intensity statistics. As the intensity is relatively accessible experimentally, this result shows that doing statistics of the intensity over many disorder realizations may be an effective way to experimental observe the Anderson localization transition of light in a disordered medium. Mapping the variance as a function of the density and the detuning is done in Sec.9.4 and allows to exhibit a phase transition between a dilute and a localized regime. An interesting question is how the variance (and the conductance) behaves through the transition and it scales. Finally, we see that the variance in the reflection plane is one and the PDF of the intensity is an exponential even in the localized regime. Indeed, the reflected intensity is more sensitive to surface modes that are single scattering modes so they are less probably localized. It is an equivalent discussion than the one done in the introduction about the difference between a plane wave and a Gaussian laser.[7] As the results of this discussion, in the following of this part, we use the variance (and the conductance) to study intensity distribution and we look in the

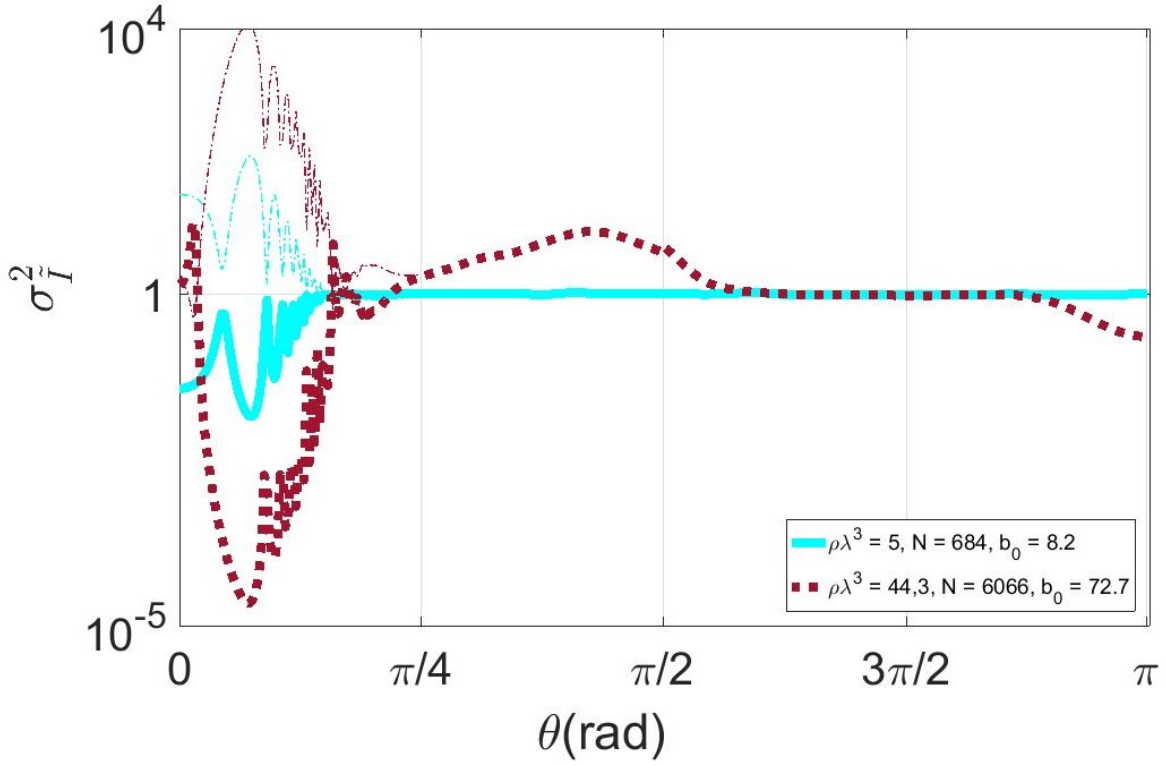

Figure 30 – Variance as a function of the angle θ for atoms uniformly distributed in a cube of side length L with a detuning $\delta = 1$. Blue curves are for a density $\rho\lambda^3 = 5$, $N = 684$ atoms and the red curves are for a density $\rho\lambda^3 = 44$, $N = 6066$ atoms. Intensity is computed in direction $\mathbf{r_o}$ where $r_o = 250L$, $\phi = 0$ and the laser field is set to zero in the reflection plane. We use a Gaussian laser with waist $W_0 = L/4$. Statistics are done over 10 000 realizations. Dash lines are for the mean intensity $\langle I \rangle$.

Source: By the author

transmission plane outside the forward lobe (usually $\theta = 75°$).

9.4 Phase transition mapping

Since the localized modes typically have their energy in a given range, it is interesting to study the dependence of the variance on both density and laser detuning. We perform this study for two cases: a uniformly distributed cube of fixed side length $k_0 L = 32.4$ (Fig.31a) and a uniformly distributed cylinder with a fixed number of atoms $N = 2000$ (Fig.31b). We clearly observe a phase transition that divides two regimes: the dilute regime where $\sigma_{\tilde{I}}^2 = 1$ and $g \to \infty$ and the localized regime where the variance increases and the conductance falls to one. The signatures of localization rise in the same area for the four figures ($\delta \approx 1, \rho\lambda^3 \approx 20$). It is realized for two different geometries and setups (N or $k_0 L$ fixed) but they show the same results, which suggests that this transition is a universal density-detuning effect.[48] Then finding the same phase transition using two

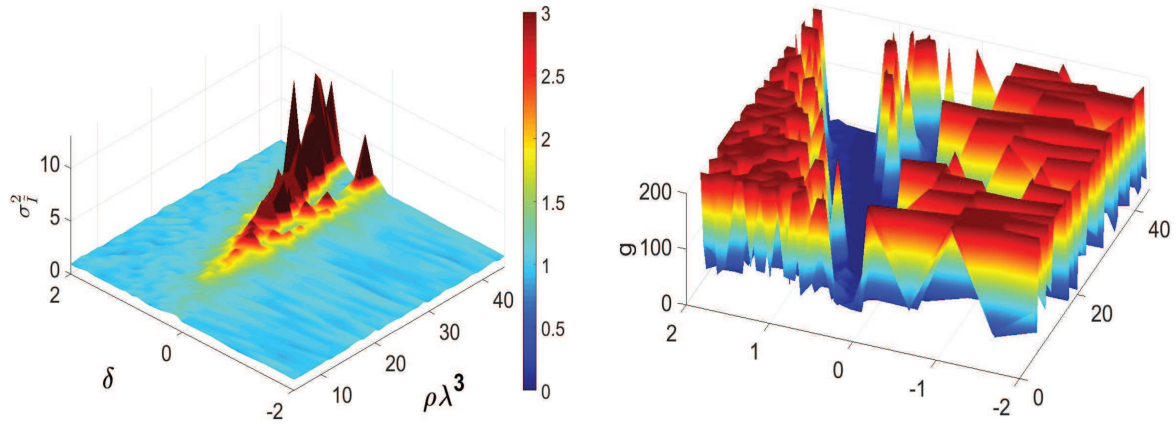

(a) Atoms are distributed in a cube of fixed side length $k_0 L = 32.4$. Statistics are done over 800 realizations.

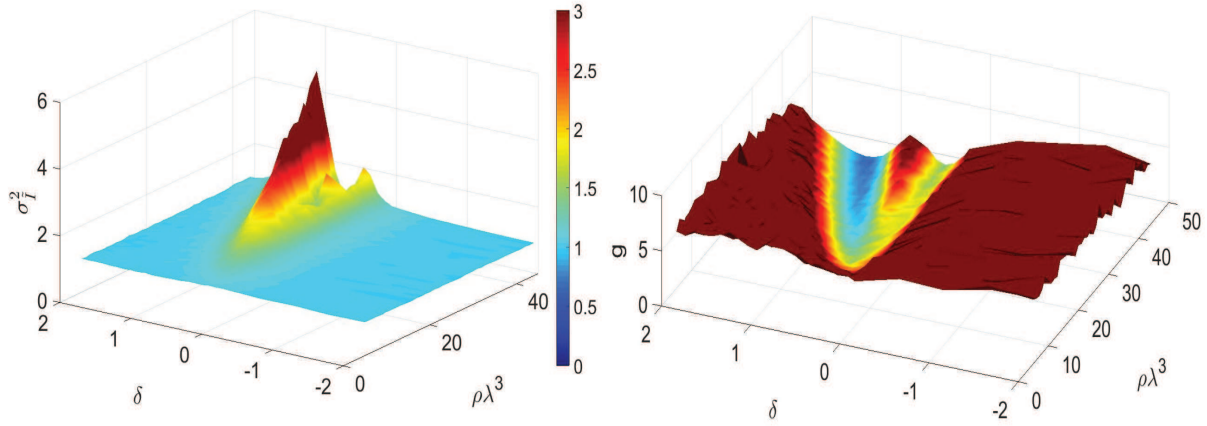

(b) The cloud is a cylinder of radius L and length L with a fixed $N = 2000$. Statistics are done over 1000 realizations and 360 values of ϕ uniformly distributed between 0 and 2π.

Figure 31 – Variance and conductance as a function of the density and the detuning. Atoms are uniformly distributed. Intensity is computed in direction $\mathbf{r_o}$ where $r_o = 250L$, $\theta_o = 75°$. We use a Gaussian laser with waist $W_0 = L/4$.

Source: By the author

different approaches (variance and conductance) is a strong argument to validate these results, and once more points at the conductance being a suitable signature of localization. Finally, the two regimes area are consistent with existing results that showed that the AL phase transition is a density effect that rises at $\rho\lambda^3 \sim 22$[66] and it fits recent work that pointed out that the AL phase transition is asymmetric in δ[48] and does not appear for negative detuning.

This work allows finding the phase transition between the dilute and the localized regimes but not to identify whether a specific set of parameter $(\delta, \rho\lambda^3)$ corresponds to a localized one since in the deep localized regime the variance and the conductance present

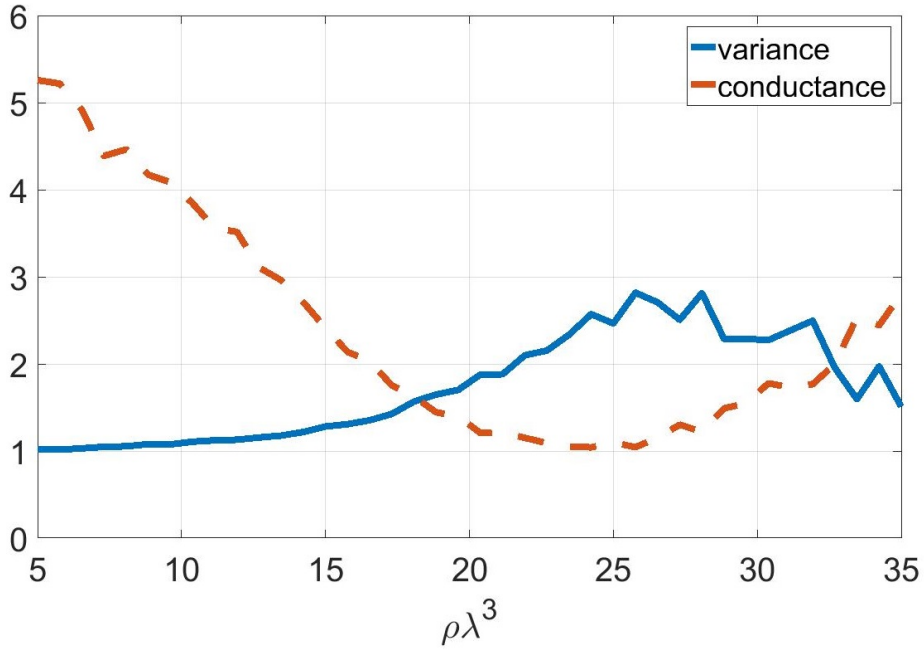

Figure 32 – Variance and conductance as a function of the density. Atoms are uniformly distributed in a cylinder of radius and length L. We use a Gaussian laser with waist $W_0 = L/4$. Intensity is computed in direction (r_o, θ, ϕ) where $r_o = 250L$ and $\theta_o = 75°$. The detuning is $\delta = 0.6$ and we consider $N = 3000$ atoms so the density is $\rho = N/(\pi/4L^3)$. Statistics are done over 3600 values of ϕ that are uniformly distributed in $[0\ 2\pi]$ and 1 000 realization over the disorder.

Source: By the author

similar values as in the dilute regime.

9.5 Phase transition scaling

Since we have identified a phase transition using the variance and the conductance, we here characterise the scaling of those parameters through the transition. To do so, we perform a cut at constant detuning $\delta = 0.5$ for a cylinder of radius $R = L/2$ and length L, using a Gaussian incident beam with waist $W_0 = L/4$ and observing in direction $\mathbf{r_o}$ with $r_o = 250L$ and $\theta = 75°$. We draw in Fig.32 the variance and the conductance as a function of the density. We observe, as expected from the previous section, that the divergence from one of the variance coincide with a drop of the conductance. It has been shown[21] (p446) that the variance and the conductance are linked, in a wave-guide of M channels, by $\sigma_I^2 - 1 = 1/M^2 + 4/(3Mg) + 2/(15g^2)$. In the regime where $g \gg 1$ this expression is simplified by $\log(\sigma_I^2 - 1) \propto -2\log(g)$. We apply this formula to our system by representing in Fig.33 the variance as a function of the conductance in loglog scale. We see that the scaling is well reproduced, which allows to confirm the behaviour of the conductance at the transition. It is another interesting results as it is consistent with the scaling admitted

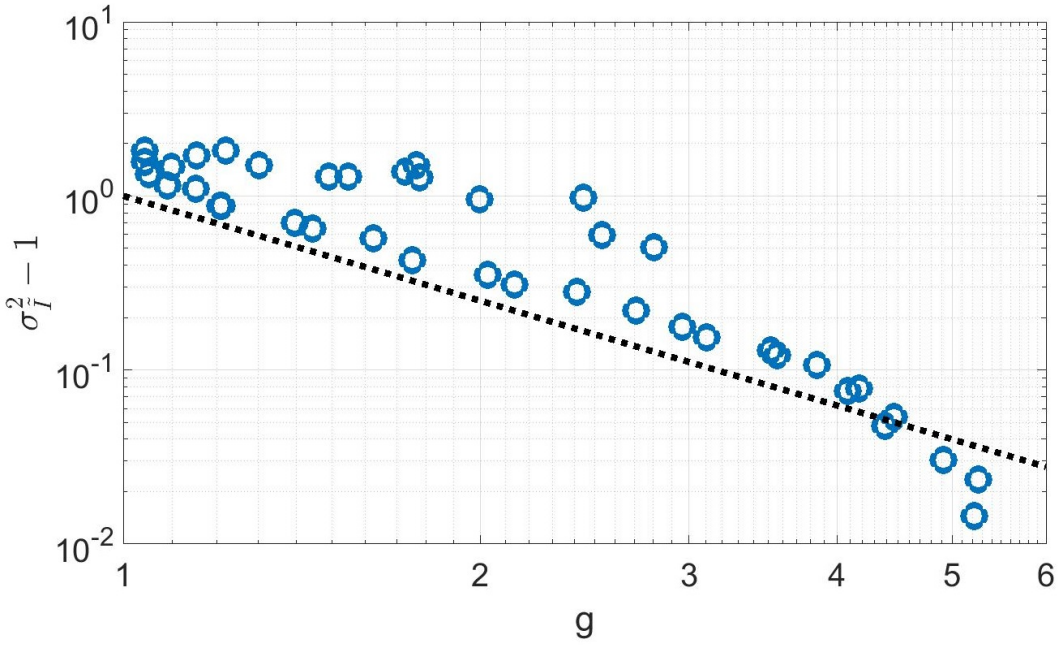

Figure 33 – Variance as function of the conductance. Figure realized with data of Fig.32, The black dashed line represent $\log\left(\sigma_I^2 - 1\right) = -2\log(g)$.

Source: By the author

by the community.

The results presented Sec.9.4 about the $\delta - \rho\lambda^3$ dependence of the transition and the scaling of the variance as a function of the conductance are two strong arguments to justify that the transition observed in the is related to the Anderson localization phase transition.

9.6 Azimuthal angle

In this section, we discuss the role of the azimuthal angle ϕ on the intensity statistics. The two questions we address are: does the variance depends on ϕ for a z-axis symmetric cloud? Can we observe the Anderson localization on only one disorder realization, using the fluctuations in the ϕ-direction? Due to the z-axis symmetry of the cloud, we expect that the azimuthal angle is not relevant for the statistics. The second question will give us information about the nature of the observable that is the intensity, i.e., we will learn about, for instance, whether it is a self-averaging variable.

In order to work with a cloud with a rotational symmetry around the z-axis, we consider a cylinder of radius $R = L/2$ and length L. As usual, we use a Gaussian incident beam with waist $W_0 = L/4$, we observe at a distance $r_o = 250L$ and an angle $\theta = 75°$ as justified above. We use the same data as in Fig.32. We remind that we call *disorder realization* the measure of the intensity for the same parameters but a different spatial

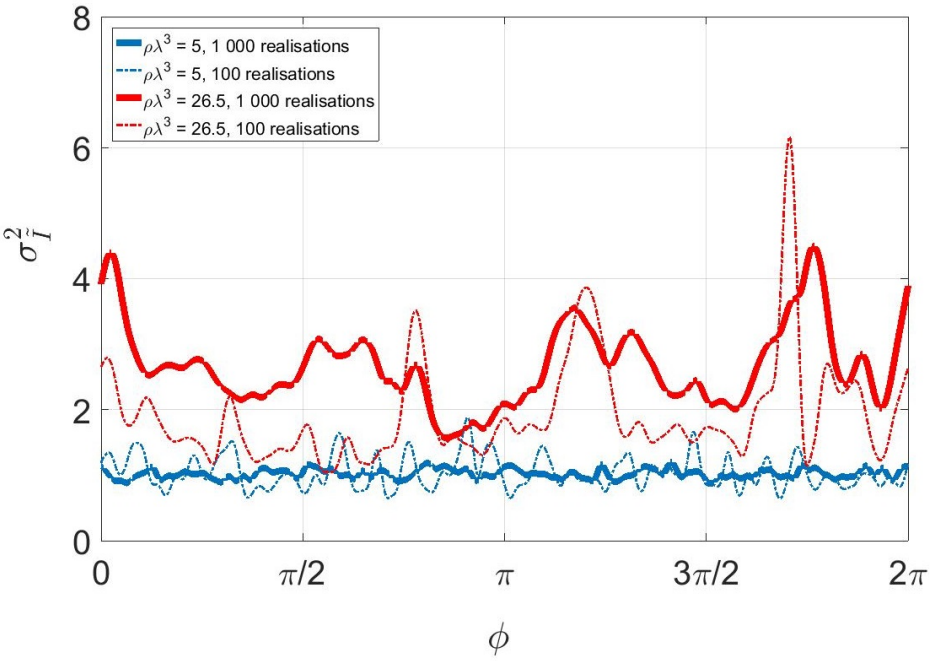

Figure 34 – Variance as a function of the azimuthal angle. Atoms are uniformly distributed in a cylinder of radius and length L. We use a Gaussian laser with waist $W_0 = L/4$. Intensity is computed in direction (r_o, θ, ϕ) where $r_o = 250L$ and $\theta_o = 75°$. The detuning is $\delta = 0.6$ and we consider $N = 3000$ atoms so the density is $\rho = N/(\pi/4L^3)$. Statistics are done over 1000 realizations for the lines and 100 realizations for dashed lines. Blue curves refer to the dilute regime of density $\rho\lambda^3 = 5$ and red curves refer to the phase transition regime of density $\rho\lambda^3 = 26.5$.

Source: By the author

distribution of the atoms in the cloud.

Let us answer the first question. As the cloud is z-axis symmetric, we do not expect a change of the intensity statistics behaviour at fixed (r_o,θ) by changing the azimuthal angle. To illustrate this point, we plot in Fig.34 the variance in direction ($\theta = 75°$, $r_o = 250L$) as a function of the azimuthal angle ϕ and for one localized and one dilute regime. The most intuitive remark is that for both densities, the localized regime stays localized ($\sigma_{\tilde{I}}^2 \gg 1$) and the dilute regime stays non-localized ($\sigma_{\tilde{I}}^2 \approx 1$) independently of ϕ despite small fluctuations. Moreover, increasing the statistics by increasing the number of disorder realizations decreases the height of the fluctuations but does not change the number of oscillations in the interval $[0,\ 2\pi]$. The number of peaks is more or less the number of non-redundant ϕ-values that we can be used to improve the statistics for a unique disorder realization. This number is limited by the speckle grain size and is proportional to $k_0 L$. The next question is: is this number large enough to produce good statistics and to observe a transition?

In order to answer the second question, we compute the intensity for one disorder realization, in direction (r_o, θ), and for a set of values of $\phi \subset [0,\ 2\pi]$. Still, the number of ϕ that is physically relevant is limited by the speckle grain size that is on the order of the normalized cloud size $k_0 L$. So, in order to extract the maximum of information, it is important to choose more than $k_0 L$ values of ϕ that are uniformly distributed in the interval $[0\ 2\pi]$. It is clear that choosing much more values of ϕ than needed will not change the statistic study. This constraint is a limitation at large densities where the cloud size decreases and so does the number of speckle grains. One solution we here apply is to average the variance over many disorder realizations. We proceed as follow: intensity is computed for a single disorder realization but using many values of ϕ, then the variance is computed from these data. Then we repeat this procedure for many disorder realizations and we average the variance computed. The final variance is obtained through statistics on ϕ and not on the disorder. The result is depicted in Fig.35a the variance as a function of the density where the variance is computed with the above procedure for two cases: one and 1 000 disorder realizations. For the red curve, we have limited statistics and the results are unclear. But, the blue dashed curve shows a smooth increase of the variance at the phase transition which is confirmed in Fig.35b where we rescale and superpose it to the variance computed with two other methods. The red dash line of Fig.35b refers to the usual variance computed in direction $\phi = 0$ and over disorder realizations. The yellow line is a combination of the two other methods.

The generalization of the above discussion and specifically the Fig.35b is shown in Fig.36 where the equivalent of Fig31a is shown but computing the variance with statistics on ϕ. We clearly see that it exhibits the same phase transition as in Sec.9.4. The important result of this section is that the phase transition can be observed using a single disorder realization.

9.7 Vectorial description of light

One more study that can be done to confirm that the transition shown by the intensity statistics is an Anderson localization phase transition is to perform the same work as in Sec.9.4 using a vectorial description of the light. Theoretical results showed that the vectorial behaviour of light, and the near-field terms that come with it, suppresses localization.[47] In Fig.37, we show the equivalent of that in Fig.31a but for vectorial light and introducing a strong magnetic field, $\Delta_B = \mu_B g m B/\hbar$ is the frequency shift due to applied magnetic field where μ_B is the Bohr magneton, g the Lande factor, m the Zeeman substate and B a magnetic field. First, we see that, as expected, no transition appears in Fig.37a as the vectorial behaviour of light is considered and no magnetic field is apply which has already been shown through a scaling analysis.[47] However, when a large magnetic field is apply, a phase transition exists on the $m = \pm 1$ Zeeman levels[49,87] what we see in

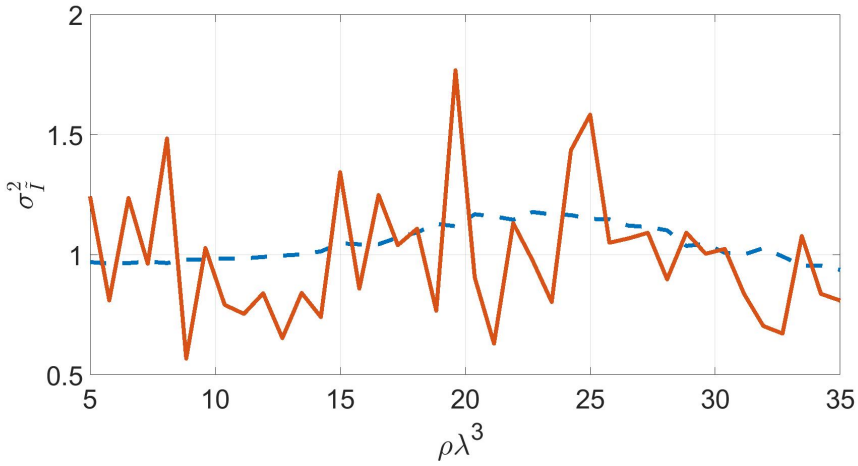

(a) Variance computed with 3600 values of ϕ that are uniformly distributed in $[0\ \pi]$ and for one disorder realization, red line. For the blue dashed line, the variance is then averaged over 1 000 disorder realizations.

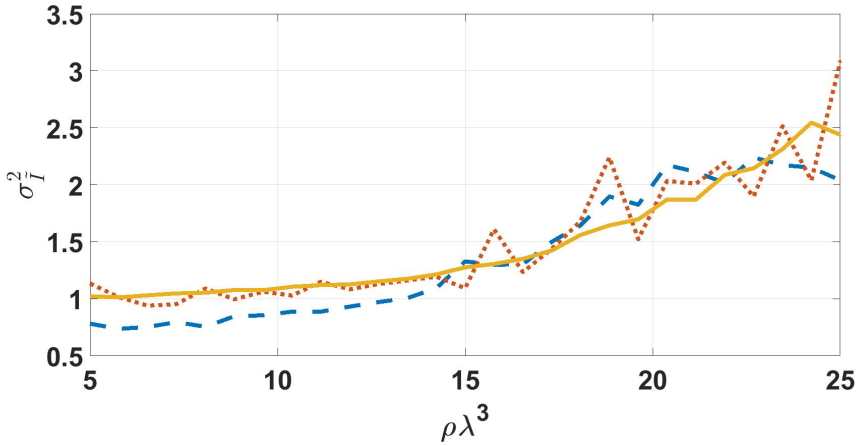

(b) The blue dashed curve is the same as the blue dashed line of Fig.35a [a.u], the red dashed line is for the variance computed for 1000 disorder realizations at $\phi = 0$ and the yellow line is the same as the red dashed line but averaged over 3600 values of ϕ.

Figure 35 – Variance as a function of the density for a cloud of atoms uniformly distributed in a cylinder of radius and length L. We use a Gaussian laser with waist $W_0 = L/4$. Intensity is computed in direction (r_o, θ, ϕ) where $r_o = 250L$ and $\theta_o = 75°$. The detuning is $\delta = 0.6$ and we consider $N = 3000$ atoms so the density is $\rho = N/(\pi/4L^3)$. We use 3600 values of ϕ that are uniformly distributed in $[0\ 2\pi]$ and 1 000 realizations over the disorder.

Source: By the author

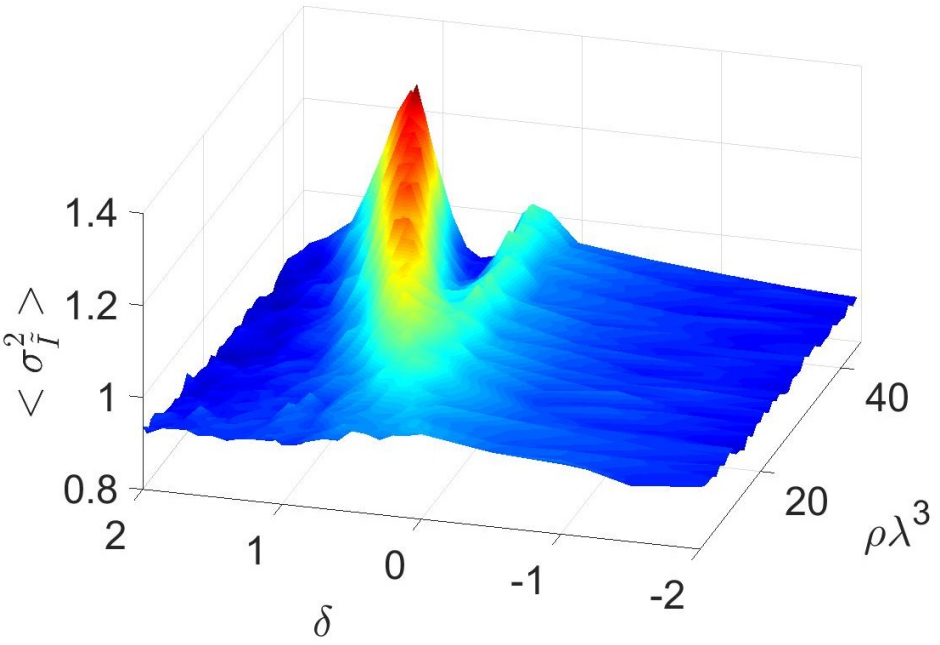

Figure 36 – 3D representation of the variance as a function of the density and the detuning for a cloud of a fixed number of atom $N = 2000$ uniformly distributed in a cylinder of radius L and length L. Statistics of the intensity are computed in direction $\mathbf{r_o}$ where $r_o = 250L$, $\theta_o = 75°$ for 1000 realizations and 360 values of ϕ uniformly distributed between 0 and 2π. We use a Gaussian laser with waist $W_0 = L/4$. For each realization, a variance is computed with the 360 values of ϕ then the final variance is computed by the average of the 1000 previously computed variances.

Source: By the author

Fig.37c and Fig.37d. It is one more argument that linked the transition we observe through the intensity fluctuations to the AL phase transition of the scaling analysis. We have found the same results for simulations at fixed number of atoms. The figures presented in this section have been done by the PhD student Ana Cipriš.

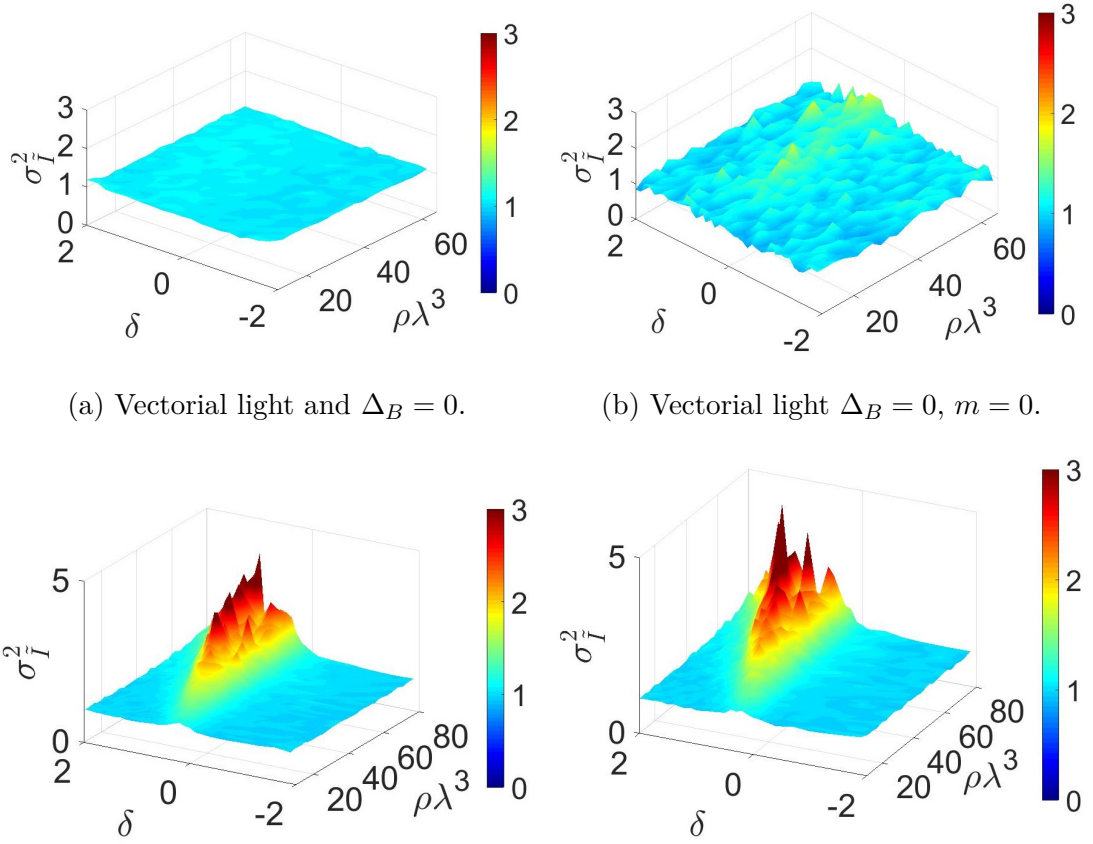

(a) Vectorial light and $\Delta_B = 0$.

(b) Vectorial light $\Delta_B = 0$, $m = 0$.

(c) Vectorial light $\Delta_B = 1000\Gamma$ and $m = -1$.

(d) Vectorial light $\Delta_B = 1000\Gamma$ and $m = +1$.

Figure 37 – 3D representation of the variance as a function of the density and the detuning for a cloud of atoms uniformly distributed in a cylinder of side length L and radius $L/2$ with a fixed $k_0 L = 21.5$. Intensity is computed in directions $\mathbf{r_o}$ where $r_o = 250L$, $\theta = 75°$. We use a Gaussian laser with waist $W_0 = L/4$. Statistics are done over 400 realizations and 51 values of ϕ. The full vectorial model is considered (a) in absence of magnetic field, and (b–d) with a strong magnetic field $\mathbf{B} = B\hat{z}$. The energy shift between the sublevels is $\Delta_B = 1000\Gamma$.

Source: Provided by Ana Cipriš.

10 CONCLUSION

We have first shown that the incoherent transmitted intensity in the steady-state and the subradiant rate do not change at the Anderson localization phase transition, so they are not proper observables to detect the localization transition. Then we have shown that a non-Rayleigh distribution of the incoherent transmitted intensity rises at the Anderson localized phase transition by looking at the PDF of the intensity, the variance and the conductance. In order to link this observation to an effective signature of an Anderson localization phase transition, we compared it with existing results on the subject. First, we saw a clear transition on the variance that depends on the density and the detuning. This transition line is in agreement with recent results of[48] obtained by a scaling analysis. We also showed that the localized regime exhibited by the study of the variance coincides with a conductance falling to zero whereas the dilute regime area has a conductance going to infinity, which matches with the interpretation of the conductance.[83] We also recover the scaling of the variance as a function of the conductance. The last test consisted in considering a vectorial model of light. We recovered that there is no phase transition with the vectorial light in absence of magnetic field, as shown in.[87] Finally, we found that introducing a strong magnetic field makes the phase transition re-appear again in the same $(\delta, \rho\lambda^3)$-range as published in reference.[49] All those tests confirm that the transition observed in the study of the incoherent transmitted intensity fluctuations is an Anderson localization phase transition. It is an interesting result as it provides an experimental observable to detect the Anderson localization of light in 3D.

Experimentally, the intensity can be continuously measured while the atoms are moving due to the finite temperature of the cloud. Two measurements of the intensity at a large time difference can be considered as two independent realizations because the atoms have moved enough. Thus measuring experimentally the autocorrelation function $g^{(2)}(\tau)$ from the detection of the intensity $I(t)$ over a long time will provide the variance. Indeed, the autocorrelation function at $\tau = 0$ can be linked to the variance with $g^{(2)}(0) = \sigma_I^2 - 1$. This relation is interesting as it makes the connection between the full study done in this part with the variance and an experimental observable.[109] In Fig.38, we present a curve $g^{(2)}(0)$ as a function of the detuning for a dense cloud and a scalar description of the light, obtained from numerical simulations of a cloud with atoms in motion. The realization of this figure took 10 days of simulations and we would need more time to get better statistics. The main message of this figure is that for a negative detuning $g^{(2)}(0) \approx 2$ whereas the fluctuations significantly increase for a positive detuning. It is a similar transition than what was observed in Fig.31b.

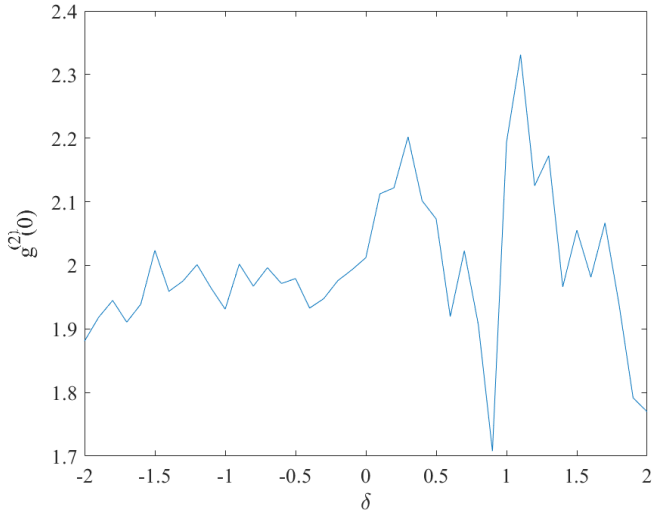

Figure 38 – Autocorrelation function with the detuning for an atomic cloud of $N = 500$ particles with a density of $\rho\lambda^3 = 49.61$ and a temperature of $T = 10^{-8}K$. Intensity is computed for 2.10^{-3} seconds and the autocorrelation function $g^{(2)}(0)$ is computed for a time step of $dt = 4.10^{-8}$ seconds.

Source: By Dr. Romain Bachelard

Another method to introduced disorder in the system has been recently proposed[20] and is based on the original work of P.W.Anderson that consists in considering a diagonal disorder. Preliminary work is presented in the following Part.V where we use an approach similar to that developed in this Part.IV.

Part V

Diagonal disorder for Anderson localization

11 INTRODUCTION

We explored in Part.IV and Ch.5.5 the Anderson localization transition by tuning the strength of disorder through the density. This approach requires to reach high densities, which is experimentally hard to achieve and where other physical phenomena like collisions are not negligible. Moreover, in the experiment, atoms are not perfect two-levels atoms, and the temperature is not zero. In this part, we investigate another way to introduce disorder in the system. Indeed, in the original work of P.W. Anderson on electronic transport, the disorder was managed by the strength of the random potential applied on each site of a lattice. If we draw a parallel with our system, the propagation of light in a cloud of cold atoms, the random potential refers to diagonal disorder. It consists of adding a random perturbation in the detuning between the atomic transition and the laser frequency. It is equivalent to adding a random term in the diagonal of the coupling matrix D; ergo the name of the diagonal disorder. It opposes the off-diagonal disorder that refers to the disorder resulting from the random distribution of the atoms. One advantage and interest of this method is that one does not need to work at high densities to reach a strongly disordered system. Nevertheless, it modifies the physical interpretation of global parameters such as the mean free path and the optical thickness. Indeed, when introducing a diagonal disorder, every atom detuned differently from the laser and also has a different cross section. An important question is about the physics introduced by the diagonal disorder. Are the effects equivalent to driving the atoms far from resonance? Or can the diagonal disorder lead to Anderson localization?

It has been shown, in 1D and 3D,[113] for an Anderson lattice model coupled to a common decay channel, that, due to diagonal disorder, subradiant states become hybrid, meaning they become localized and extended, whereas superradiant states are extended. It justifies that one looks for Anderson localization in presence of diagonal disorder in the long lifetime modes.[113–116] Another work, recently proposed[20] that increasing the diagonal disorder strength is a way to reach the localized regime even at low densities. The participation ratio (PR) of a precise selection of subradiant modes was studied and an abrupt change of the mean PR was observed at a given diagonal disorder which was explained as a signature of a localization transition. This method to reach the localized regime is not in contradiction with the density approach but it is fundamentally different. The question we try to answer in this part is about the diagonal disorder as a way to reach the localized regime. The parallel between the results of this chapter and the paper[20] should give strong motivations to continue in this direction. Indeed, we observed a similar transition by using two different approaches, a study of the PR and the intensity statistics fluctuations. As we did in the previous Part.IV we investigate the fluctuations of the

transmitted intensity and more precisely, the variance of the normalized radiated intensity while increasing the diagonal disorder. In order to observe the same transition as in,[20] we use the same parameters. *The goal is to see if we recover the same transition as in[20] in the variance of the intensity statistics*, like for instance, the scaling in W/b_0 of the phase transition.

Like in the three previous chapters, we study the interaction between a laser and a cloud of two-level cold atoms. Atoms are characterized by $N \gg 1$ point scatterers of fixed position $\mathbf{r}_j$, randomly distributed with density $\rho(\mathbf{r})$, transition linewidth Γ (also called single atom decay rate) and frequency ω_a and Rabi-frequency is $\Omega \ll \Gamma$. The medium has a characteristic size L (for instance, the cube side length). The laser is a Gaussian beam of waist $W_0 = L/4$ as justified in the previous part, we use the coupled-dipole model, and the intensity is defined as in the previous part. The optical setup is illustrated in Fig.23. Concretely, the diagonal disorder is introduced as follows: for every atom a of the cloud, the detuning of this atom $\delta_a = (\omega_0 - \omega_a)\,\Gamma$ is replaced by $\delta_a + W_a$ where W_a is a random number in $[-W/2,\ +W_2]$ and W is the strength of the diagonal disorder and can simply be called diagonal disorder. Numerically, we generate N random numbers W_i in the interval $[-W/2,\ +W/2]$ and we replace the coupling matrix D defined in Sec.1.1 of Part.II by $D \to D - \imath I_N W_d$, where I_N is the identity matrix of size $N \times N$ and $W_d = (W_1, W_2, \cdots W_N)$. The name of *diagonal disorder* comes from the fact that we add a term on the diagonal of the coupling matrix D. In Sec.9.3 of the previous Part.IV, we showed that the best direction to look for the Anderson localization phase transition in the intensity fluctuations in the transmission direction but out of the forward lobe, and so, we shall compute the intensity in the direction, for instance, $\theta = 75°$ or $\theta = \pi/6$. Moreover, the statistics of the intensity are realized over many realizations. For each realization, the positions $(\mathbf{r}_j)$ and the detuning (W_j) of all atoms are randomly generated, for a low-density configuration. Thus, the statistics are realized on two variables that are the positions and the detunings of the atoms. We saw in the previous Part.IV, by doing statistics on the positions, that there is no localization at low density. Therefore, we do not expect that the statistics over the position of the atoms will play a role in the results presented in this part.

In the first chapter Ch.12 we show how the diagonal disorder modifies the spectrum of the coupling matrix. Ch.13 concerns the incoherent transmitted intensity; here we study the influence of the diagonal disorder on the Ohm's law and on the fluctuations of the intensity. Finally, in Ch.14 we bring our attention to the radiated intensity decay dynamic, and we compare the statistical analysis with the results presented in the paper.[20]

12 SPECTRA ANALYSIS

Let us first look at how the diagonal disorder modifies the set of eigenvalues of the coupling matrix D introduced in Sec.1.1 of Part.II. We plot in Fig.39 the spectrum of the coupling matrix D for different values of the diagonal disorder W. We see that increasing the diagonal disorder squeezes the decay rate range (γ_n) and widens the energy shift range (ω_n). In the paper,[20] similar results were shown. The increase of the subradiant

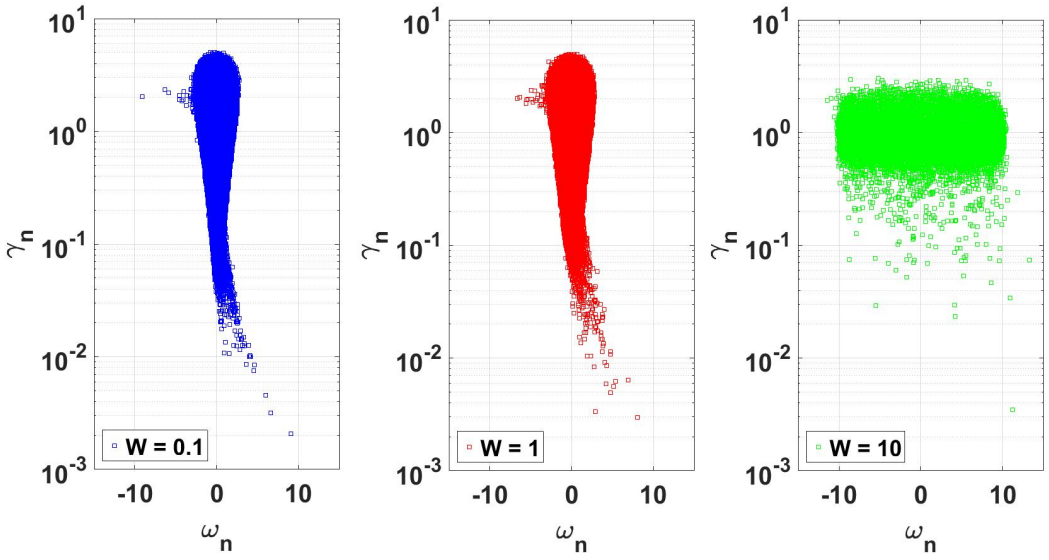

Figure 39 – Eigenvalues of the coupling matrix computed for $N = 2000$ atoms uniformly distributed in a cube of length L with a detuning of $\delta = 0$ and a resonant optical thickness of $b_0 = 10$. 10 realizations on the distribution of the atoms are performed.

Source: By the author

eigenvalues with the introduction of a diagonal disorder W modifies the behaviour of the decaying intensity at longer times and more precisely, the subradiant rate that we extensively discussed in Sec.3.3 (illustrated in Fig.16). The question is: is the increase of the subradiant rate due to the new physics introduced by the diagonal disorder (like localization), or is it simply an effect of the increasing subradiant eigenvalues' decay rate? This question is important because it has been recently mentioned[88] that the localization regime might change the long lifetime slope of the radiated intensity. At this stage, we cannot answer this question as the subradiant rate has been shown to scale with the resonant optical thickness[18] which is not properly defined with the introduction of the diagonal disorder which we discuss below.

13 STATIONARY REGIME

13.1 Mean intensity

We now look at the mean scattered intensity. Experimentally and numerically (using the radiative transfer equation) it has been shown[60] that the transmission as a function of the detuning follows a Lorentzian law in the single scattering regime ($b(\delta) \ll 1$). Close to resonance, the transmission as a function of the detuning has a saddle shape, where the width depends on the resonant optical thickness b_0. In Fig.40, we draw a $3D$-map of the transmitted intensity in the direction $\theta = 75°$ as a function of the detuning and the diagonal disorder W for two values of the resonant optical thickness. First, we recover that for a large $b_0 = 35$, Fig.40a, we see a saddle shape, whereas it disappears at low $b_0 = 3.5$, Fig.40b. We observe that for a low diagonal disorder, $W < 1$, the *usual* saddle-Lorentzian shape is not modified and the width of the saddle is constant as b_0 is constant. However, for a large diagonal disorder, $W > 100$, the transmission is independent of the detuning and it decreases with W. In the regime, where $W \gg |\delta|$ the diagonal disorder W seems to play the role of the detuning, and the transmitted intensity follows a function of W. For instance, we could imagine an effective optical thickness: $b(\delta, W) = b_0/\left(1 + 4(\delta + W/2)^2\right)$. For a low diagonal disorder $W \ll 1$, and a low detuning $\delta \ll 1$, the quantity $\delta + W/2$ is much lower than one. Thus, the effective optical thickness does not depend on those two parameters (δ and W) but only on b_0. In another regime, where $4(\delta + W/2)^2 > 1$, we can distinguish two cases: when $\delta \gg W$, the diagonal disorder is not strong enough to modify the effective optical thickness, and when $W > \delta$ the diagonal disorder dominate δ and plays the role of the detuning. We apply this interpretation to Fig.40a: at resonance ($\delta = 0$), the saddle-Lorentzian shape breaks for $W \approx 3 > 0$ ($W^2 \approx 9 > 1$), which is consistent with this simple interpretation. However, it remains a phenomenological interpretation.

When introducing a diagonal disorder, the two parameters, the detuning δ and the optical thickness $b(\delta)$, are not well-defined as all atoms have a random effective detuning of $\delta + W_i/2$. Hence, we cannot use the optical thickness for physical interpretations. However, we see in Fig.40 that the shape of the transmission as a function of the detuning stays the same until a given diagonal disorder. It shows two regimes: the weak diagonal disorder regime, where the mean transmission is constant at constant detuning, and the strong diagonal disorder regime where the transmission scales with W. It is interesting to notice that the transition between those two regimes seems, at a first order, independent of the detuning and appears at $W_c \approx 1$ for $b_0 = 35$ and $W_c \approx 2$ for $b_0 = 3.5$. Even though the two extreme regimes are understood, it would be interesting to characterize the transition with δ and W. Indeed, it might help to extract a universal law of this transition which could help understanding the physics involved at the transition. Moreover, this transition

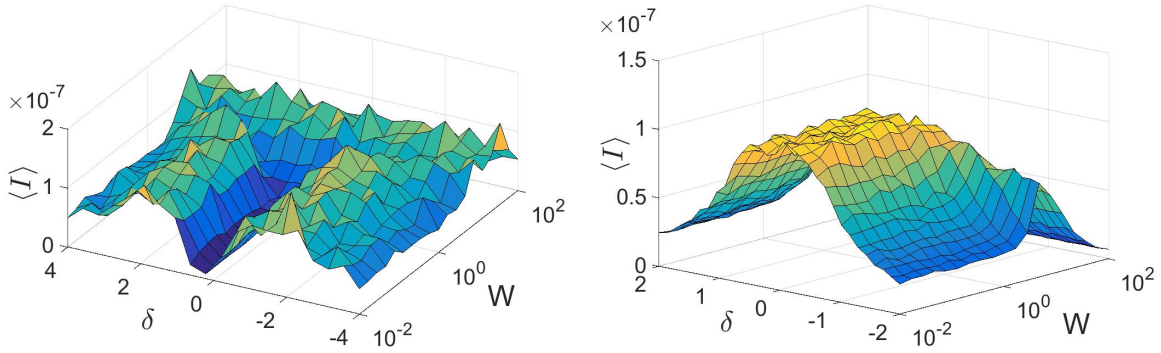

(a) $N = 4800$, $k_0 L = 41.5$, $\rho\lambda^3 = 16.64$ and 50 realizations.

(b) $N = 800$, $k_0 L = 53.6$, $\rho\lambda^3 = 1.29$, $b_0 = 3.5$, 1000 realizations.

Figure 40 – Mean radiated intensity of the steady-state for a cloud of N atoms distributed in a cube of side length $k_0 L$ and with a density of $\rho\lambda^3$. The laser beam is Gaussian of waist $W_0 = L/4$. The intensity is computed in direction $r_o = 250L$, $\theta = 75°$.

Source: By the author

depends on b_0 and W but not at a fixed W/b_0 which is an important remark for what will follow. The large W regime can be interpreted as a simple single scattering regime as all atoms are far detuned from the laser frequency.

In the absence of diagonal disorder, the optical thickness $b(\delta) = b_0/(1 + 4\delta^2)$ is used to distinguished two regimes: the single scattering regime $b \ll 1$ and the multiple scattering regime $b \gg 1$. In addition, the Beer-Lambert law that is defined for the coherent transmission ($\theta = 0$) says that in the stationary regime, $I/I_{laser} = \exp(-b(\delta))$. Unfortunately, those interpretations are not possible any more with the introduction of the diagonal disorder as $b(\delta)$ is not clearly defined as we discussed above. We tried to replace $b(\delta)$ in the Beer-Lambert law by the effective optical thickness $b(\delta, W)$ defined above but without full satisfaction. In order to get rid of the physical interpretation of $b(\delta)$, we will use the coherent transmission $T_c = I(\theta = 0)$ as a measure of the single and multiple scattering. We know that increasing the detuning decreases the multiple scattering, and we expect the diagonal disorder to behave equally. To illustrate this, we present in Fig.41 the incoherent ($\theta = \pi/6$) scattered intensity as a function of the coherent transmission, in the stationary regime, and tuning W and δ. Surprisingly, all the points fall on one *universal* curve. It is a really useful result as it allows to distinguish the single and multiple scattering regime without considering the optical thickness. At fixed detuning, increasing the diagonal disorder always moves the points towards the right which is the single scattering regime. It would be interesting to compare how fast the detuning and the diagonal disorder bring the system in the single scattering regime. It would help to distinguish the role of those two parameters. Indeed, the preliminary results show that the

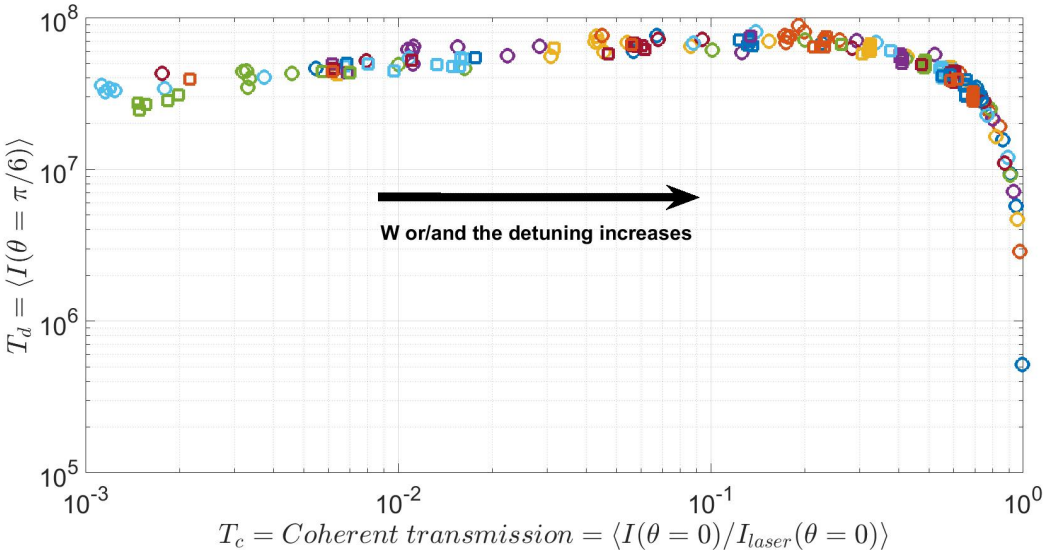

Figure 41 – Mean incoherent radiated intensity, in direction $\mathbf{r_o}$ where $r_o = 250L$, $\theta = \pi/6$ and $\phi = 0$, as a function of the coherent transmission. Atoms are uniformly distributed in a cube of side length L. Intensity is computed over 100 realizations. We use a Gaussian laser beam of waist $W_0 = L/4$. We use 9 values of the diagonal disorder $W \in [0,\ 100]$. There are two sets of data: 1/ circles: fixed size $k_0 L = 60$ and $\delta = 0$, for each value of W the optical thickness is modified by tuning $b_0 \in [0.3,\ 20]$; 2/ squares: fixed number of atoms $N = 4800$ and resonant optical thickness $b_0 = 35$, for each value of W the optical thickness is modified by tuning the detuning $\delta \in [0,\ 5]$.

Source: By the author

diagonal disorder plays a similar role to that of the detuning which cannot be totally true.

13.2 Intensity fluctuations

We bring our attention to the fluctuations of the radiated intensity in the steady-state when tuning the diagonal disorder strength. As we showed in the previous Part.IV, the variance is a good indicator for investigating a change of behaviour in the intensity fluctuations. We show in Fig.42 the variance of the normalized intensity statistics for the same parameters as in Fig.40b and with 1000 realizations. We see that the transition between the two regimes discussed in Sec.13.1 does not impact the variance. According to the results of Part.IV, we would like to affirm that the absence of a transition in Fig.42 means that there is no localization for this set of parameters. However, it is too strong of a statement. We will simply say that the fluctuations of the intensity in the steady-state do not allow for observing localization. Indeed, the stationary regime is dominated by the superradiant modes that have been shown not to be localized modes.[113] Also, even if localized modes exist for some parameters of Fig.42, they are overwritten by the superradiant modes. Hence, the localized modes do not modify significantly the intensity

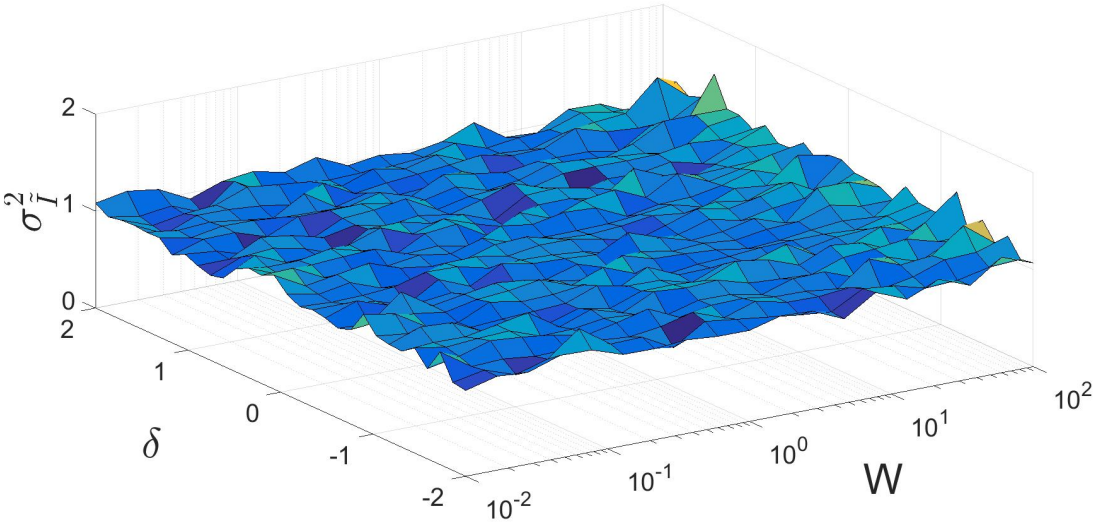

Figure 42 – Variance of the normalized radiated intensity as a function of the detuning and the diagonal disorder for a cloud of $N = 800$ atoms distributed in a cube of side length $k_0 L = 41.5$ and with a density of $\rho\lambda^3 = 1.29$. The laser beam is Gaussian of waist $W_0 = L/4$, $b_0 = 3.5$. The intensity is computed in direction $r_o = 250L$, $\theta = 75°$ and for 1000 realizations.

Source: By the author

fluctuations in the steady-state which does not allow for observation of the localization's transition in the variance. Thus, we want to focus our attention on the long lifetime modes that are more likely to be localized. There exist three kinds of long lifetime modes: the radiation trapping modes, the subradiant modes and the localized modes. We can easily get rid of the radiation trapping by applying a strong detuning or a large diagonal disorder as illustrated in Fig.41. However, it is not trivial to distinguish the subradiant modes from the localized modes. In order to select the long lifetime modes, we bring our attention, in the next Ch.14, to the decaying intensity at a long time. Indeed, at a long time, it would remain only the subradiant, radiation trapping and localized modes, whereas the superradiant modes would have already decayed.

Moreover, we have observed that for a very large diagonal disorder, the variance always increases above one as illustrated in Fig.43. We first thought that it might be a single scattering regime effect as Fig.43a suggests. However, we know that it is not as we showed in the previous Part.IV that, without diagonal disorder and at large detuning, the variance stays equal to one. Hence, this effect is because of the introduction of a diagonal disorder. We now want to understand this effect and why a large diagonal disorder makes the variance of the normalized intensity increase above one.

In order to answer this question let us take the simple example of one atom at position $\mathbf{r} = \mathbf{0}$ with $\delta + W_a$ the detuning of the atom where W_a is the detuning fluctuation

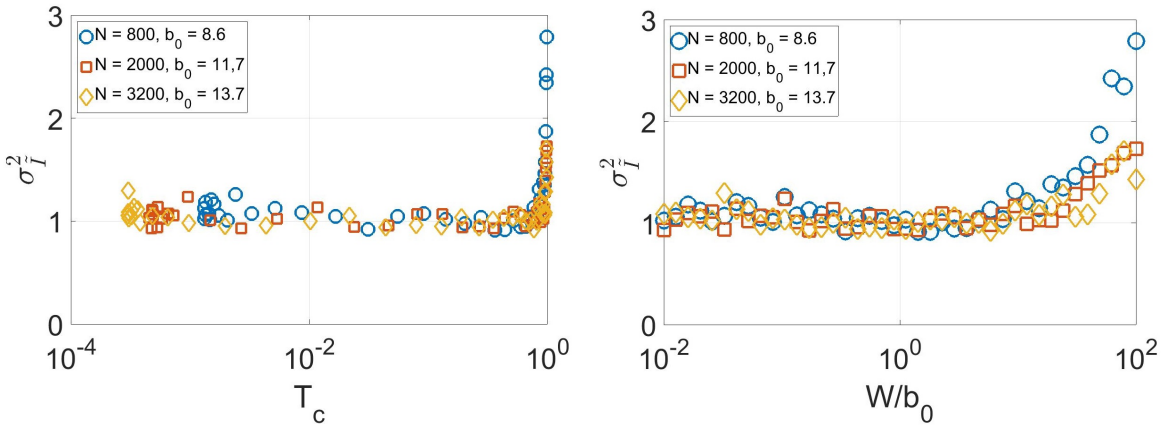

(a) (b)

Figure 43 – Variance of the normalized radiated intensity as a function of the diagonal disorder for a cloud of N atoms distributed in a cube of side length L and with a fixed density of $\rho\lambda^3 = 5$. The laser beam is Gaussian of waist $W_0 = L/4$. The intensity is computed in direction $r_o = 250L$, $\theta = 75°$, $\phi = 0$ and 1000 realizations where used.

Source: By the author

that is randomly chosen in $[-W/2,\ +W/2]$ and where W is the strength of the diagonal disorder. The coupled-dipole model is then described by a simple differential equation:

$$\frac{d\beta(t)}{dt} = \left(\imath\left(\delta + W_a\Gamma\right) - \frac{\Gamma}{2}\right)\beta(t) - \frac{\imath}{2}E_0, \tag{13.1}$$

where we note $E_0 = E_{laser}(0)$, the laser field at position $\mathbf{r} = 0$. In the stationary regime, the dipole is:

$$\beta^{stat} = \frac{\frac{\imath}{2}E_0}{\imath\left(\delta + W_a\Gamma\right) - \frac{\Gamma}{2}}. \tag{13.2}$$

In order to simplify the problem, we use $\delta = 0$, and we normalise by all the constants so, the radiated intensity, in a given direction, is proportional to:

$$I^{stat} \propto \frac{1}{1 + 4W_a^2}. \tag{13.3}$$

The goal of these calculations is to compute the variance of the variable I^{stat} when the statistics are done over W_a. We know that the random variable W_a is uniformly distributed in $[-W/2,\ +W/2]$ and the probability distribution function (PDF) of the variable W_a is $f_W(W_a) = 1/W$. We define a new dimensionless random variable $I_s = \psi(W_a) = 1/(1+4W_a^2)$ that is defined in $I_s \in [1/(1+W^2),\ 1]$ where ψ and ψ^{-1} are differentiable. We introduce this new random variable in order to model the radiated intensity of one atom given in (13.3). The theory of probability says that the PDF of the variable I_s that we note $f_{I_s}(I_s)$ can be expressed as follows,

$$f_{I_s}(I_s) = \frac{1}{\psi'(\psi^{-1}(I_s))} f_W(\psi^{-1}(I_s)), \tag{13.4}$$

which leads to the expression:

$$f_{I_s}(I_s) = \frac{1}{2W I_s^{3/2}(1-I_s)^{1/2}}. \tag{13.5}$$

We have used this expression to compute the first and second momentum of the random variable I:

$$\mathbb{E}(I_s) = \int_{1/(1+W^2)}^{1} I_s f_{I_s}(I_s)\, dI_s = \int_{1/(1+W^2)}^{1} I_s \frac{1}{2W I_s^{3/2}(1-I_s)^{1/2}}\, dI_s \tag{13.6}$$

$$= \frac{\imath\left(\log(1+W^2) - 2\log(1+\imath W)\right)}{2W}, \tag{13.7}$$

and

$$\mathbb{E}(I_s^2) = \int_{1/(1+W^2)}^{1} I_s^2 f_{I_s}(I_s)\, dI_s = \int_{1/(1+W^2)}^{1} I_s^2 \frac{1}{2W I_s^{3/2}(1-I_s)^{1/2}}\, dI_s = \frac{\frac{W}{1+W^2} + \arctan(W)}{2W}. \tag{13.8}$$

We discuss the behaviour of the variance in the two extreme regimes of $W = 0$ and $W \to \infty$. In the limit of no diagonal disorder, *i.e.* $W \to 0$, we have $\mathbb{E}(I_s) \to 1$ and $\mathbb{E}(I_s^2) \to 1$ so, $var(I_s)/\langle I_s\rangle^2 = \sigma^2_{\tilde{I}_s} = \mathbb{E}(I^2)/\mathbb{E}^2(I) - 1 \to 0$ (we remind that $var(I_s) = \mathbb{E}(I_s^2) - \mathbb{E}(I_s)^2$ and the normalized intensity is $\tilde{I}_s = I_s/\langle I_s\rangle$). We recover the fact that when there is no diagonal disorder $W = 0$ (for a given configuration of atoms positions), there is no randomness in the computation of the intensity, so the random variable I_s is constant and its variance is zero.
Finally, the variance of the variable I_s is:

$$\frac{\mathbb{E}(I_s^2)}{\mathbb{E}(I_s)^2} - 1 = \frac{\frac{W}{1+W^2} + \arctan(W)}{\left(\log(1+W^2) - 2\log(1+\imath W)\right)^2/(2W)} - 1. \tag{13.9}$$

In the limit of a strong diagonal disorder, $W \to \infty$, the numerator of the fraction in (13.9) is finite and is equal to $0 + \pi/2$ whereas the denominator goes to zero. Finally, in the strong diagonal disorder limit, the variance divided by the square of the mean goes to infinity. In Fig.44, we plot the equation (13.9).

In the analytical calculations done above, we studied the radiated intensity of one fixed atom where the detuning of this atom is randomly chosen in the range of $[-W/2,\ +W/2]$. We performed a statistical analysis of the scattered intensity from one fixed atom where the detuning is the only random variable. These analytical calculations, summarized in Fig.44, show that the variance of the normalized scattered intensity of one atom is zero in the absence of randomness $W = 0$ and increases to infinity with increasing W. The interest of looking at the behaviour of one atom is to understand the behaviour of a system with N independent atoms. Indeed, when the diagonal disorder is too strong, all atoms are decoupled and the radiated intensity of N atoms can be model by N times the radiation of one atom. Hence, the increase of the quantity $\sigma^2_{\tilde{I}}$, that we observe in Fig.43, for a really large diagonal disorder, can be explained as a consequence of a single atom regime.

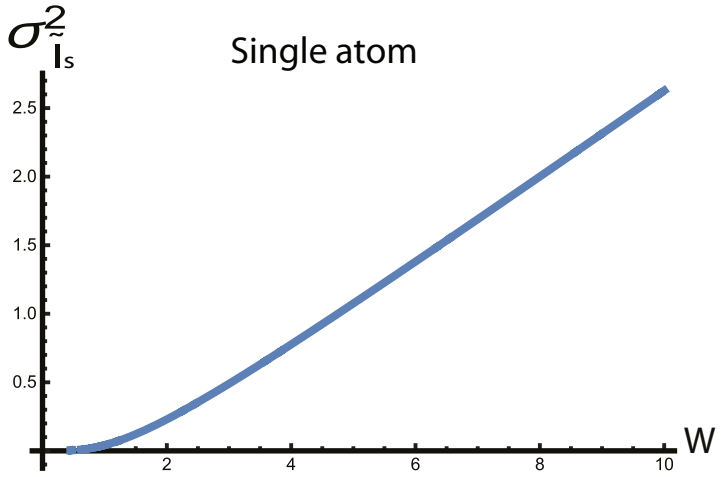

Figure 44 – Variance of the normalized intensity radiated by one atom as a function of the diagonal disorder. Equation (13.9).

Source: By the author

This single atom regime has to be carefully distinguished from the localized regime that we discussed in Part.IV. Indeed, we now know that in both regimes, the localized regime and the single atom regime, the variance of the intensity statistics in the steady-states diverges from one.

14 TEMPORAL BEHAVIOUR

In the previous Ch.12, we have explored the statistics of the radiated intensity in the stationary regime through, for instance, the variance. We here bring our attention to the dynamical regime, *i.e.* we study the statistics of the radiated intensity after the laser had been on for $\delta t = 50\Gamma^{-1}$, in the dilute regime and when increasing the diagonal disorder. The interest of looking at the radiated intensity at a long time is that the superradiant modes have already decayed and only the long lifetime modes remain (radiation trapping, subradiant and localized modes). Indeed, the superradiant modes have been shown not to be localized whereas the localized modes have a long lifetime. It is, however, important to distinguish the physics of the three long lifetime modes. The radiation trapping is perfectly described by a random walk model so we do not expect the radiation trapping modes to modify the fluctuations of the intensity. Moreover, the results presented in this chapter have been recovered by introducing a large detuning where there are no radiation trapping modes. Hence, we focus our interpretations on the subradiant and localized modes. Moreover, we stay in the dilute regime $\rho\lambda^3 \ll 22$, where we ensure that, in the absence of diagonal disorder, we are in the non-localized regime which we learned from the previous Part.IV.

We will compare the results of this part with the results of a recent publication.[20] Indeed, in this paper, Anderson localization of light in 3D is investigated at low density by introducing a diagonal disorder. The average participation ratio (PR) of a well-selected set of subradiant and superradiant eigenvalues is studied and was used to show that, for the subradiant modes, a transition in the PR appears. They link this transition to an Anderson localization phase transition. There are two results of this paper that we will discuss in this chapter. First, we see in Fig.45, extracted from,[20] that the average PR of a set of subradiant eigenvalues contains a transition that scales with the strength of the diagonal disorder divided with the resonant optical thickness and for a value of $W/b_0 \approx 0.2$. In order to recover these results, we will discuss in Sec.14.2 the variance of the radiated intensity in the subradiant regime. Moreover, we see in Fig.45, that there is no phase transition for the PR of the superradiant eigenvalues which is consistent with the fact that in Sec.13.2 we did not observe any transition because the stationary regime is dominated by superradiant modes.

The second result of this paper, that we recover in Sec.14.3, is the linear scaling of the normalised diagonal disorder W/b_0 with the critical decay rate Γ_{cr}: $W_c/b_0 \approx 1.61\Gamma_{cr} + 0.053$. It is illustrated in Fig.46.

In this chapter, we perform a statistical study of $I(t)$ that is the far-field intensity (presented in Sec.3.1) after the laser has been on for $50\Gamma^{-1}$ seconds. We remark that $I(0)$

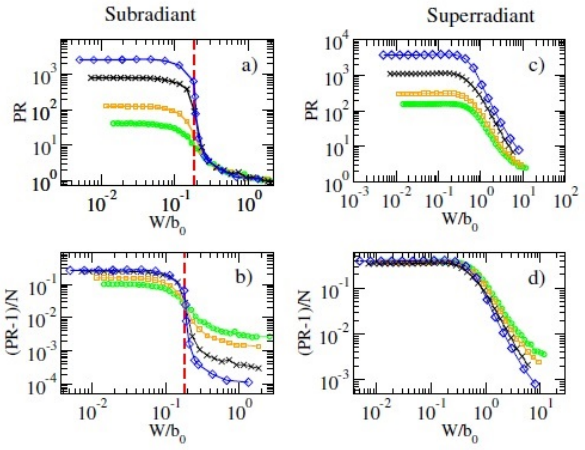

FIG. 2: (Color online) Average participation ratio Eq.(3) for subradiant states (left panels) and superradiant states (right panels) as a function of the rescaled disorder W/b_0 and different system sizes as indicated below. Above a critical disorder indicated by the red vertical dashed line, the participation ratio of the subradiant states become independent of N (upper left panel), whereas the participation ratio of superradiant states keep increasing with N (upper right panel). The normalized participation ratio shows the critical disorder separating the extended from the localized regime for the subradiant states (lower left panel), whereas no clear transition occurs for the superradiant states (lower right panel). The average was done over disorder and different eigenvalues in the interval $-0.1 < E < 0.25$ (the real part of the eigenvalue). The interval of widths is $0.046 < \Gamma < 0.1$ for the subradiant states (left panels) and $1 < \Gamma < 2.15$ for the superradiant states. The density is $\rho\lambda^3 = 5$ in all panels. Note that for each N we have different values of b_0 = 6.8 ($N = 400$, green circles), 8.6 ($N = 800$, orange squares), 13.7 ($N = 3200$, black crosses), 19.8 ($N = 9600$, blue rombs).

Figure 45 – Study of the average participation ratio of a set of sub- and superradiant eigenvalues.

Source: Adapted from CELARDO et al.[20]

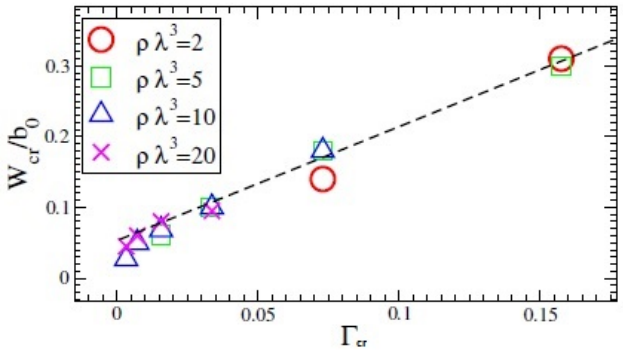

FIG. 3: (Color online) Critical disorder for localization: W_{cr} rescaled by b_0 is plotted vs the mean Γ for different densities, see figure. The black dashed line shows a fit given in Eq. (4).

Figure 46 – Diagonal disorder divided by the resonant optical thickness as a function of a transition's decay rate. The Eq.(4) mentioned in the caption is $W_{cr}/b_0 \sim 1.61\Gamma_{cr} + 0.053$

Source: Adapted from CELARDO et al.[20]

essentially corresponds to the stationary regime. The intensity is computed for a large number of realizations where, for each realization, we generate a random position and a random detuning $\delta+W_a$ for each atom, with $W_a \in [-W/2,\ +W/2]$, and W is the strength of the diagonal disorder. Then, we compute the variance in time $var(\tilde{I}(t)) = \langle\Big(\tilde{I}(t) - \langle\tilde{I}(t)\rangle\Big)^2\rangle$ where $\tilde{I}(t) = I(t)/\langle I(t)\rangle$.

14.1 Variance in time without diagonal disorder

First, we examine the variance of the radiated intensity in time without including a diagonal disorder and in the dilute regime, where no localization is expected. In Fig.47 we plot $var(\tilde{I}(t))$ at fixed $b_0 = 10$, for different number of atoms N but staying in the non-localized regime. Surprisingly, we observe that the variance diverges from one at a long times. The divergence starts at a longer time as the number of atom increases. According to Part.IV, we expected the variance to stay equal to one in the absence of localization. One interpretation might be the low statistics of the subradiant eigenvalues due to a low number of atoms. At a fixed time t, we consider that all the modes with the decay rate $\Gamma\gamma_n t > 3$ have discharged. Indeed, the mode n exponentially decays with the form $\psi_n(t) = \psi_n^0 \exp\left(-\frac{\Gamma}{2}\lambda_n t\right)$, so we know that at the time $t = 3/(\Gamma\gamma_n)$, 95% of the mode n would have decayed. Thus, at a long time, only few modes will remain populated, until only the most subradiant $(\min(\Re(\lambda_n)))$ stays populated. Hence, the statistics of the intensity a long time are strongly impacted by the number of modes that remain populated. If only few modes remain populated at time t for every realization, the statistics will not be good. In order to increase the statistics, and therefore, the number of modes populated, we can either increase the number of atoms or we compute the variance of the intensity at a shorter time. Indeed, increasing the number of atoms will increase the number of modes that satisfy the condition $\Gamma\gamma_n t > 3$ and thus, it will increase the probability to have excited modes at time t. We observe in Fig.47 that increasing the number of atoms put further the time of divergence of the variance of the intensity. However, in our simulations, we are limited by the number of atoms that we can use due to computational time. Hence, we will perform our statistical analysis of the radiated intensity at short time, between $10\Gamma^{-1}$ and $30\Gamma^{-1}$, but at a sufficiently long time to be sure that the superradiant modes have already decayed.

We conclude that the increase of $var(\tilde{I}(t))$ at long time is a subradiant eigenvalues statistics effect and should disappear for a very large number of atoms. Unfortunately, we saw in Ch.12 that introducing a diagonal disorder increases the decay rate of the subradiant eigenvalues. Ergo, we have to make sure that the increase in the variance of the intensity at a long time is not due to subradiant eigenvalues statistics but a real localization effect. It is not easy to deal with this contradiction.

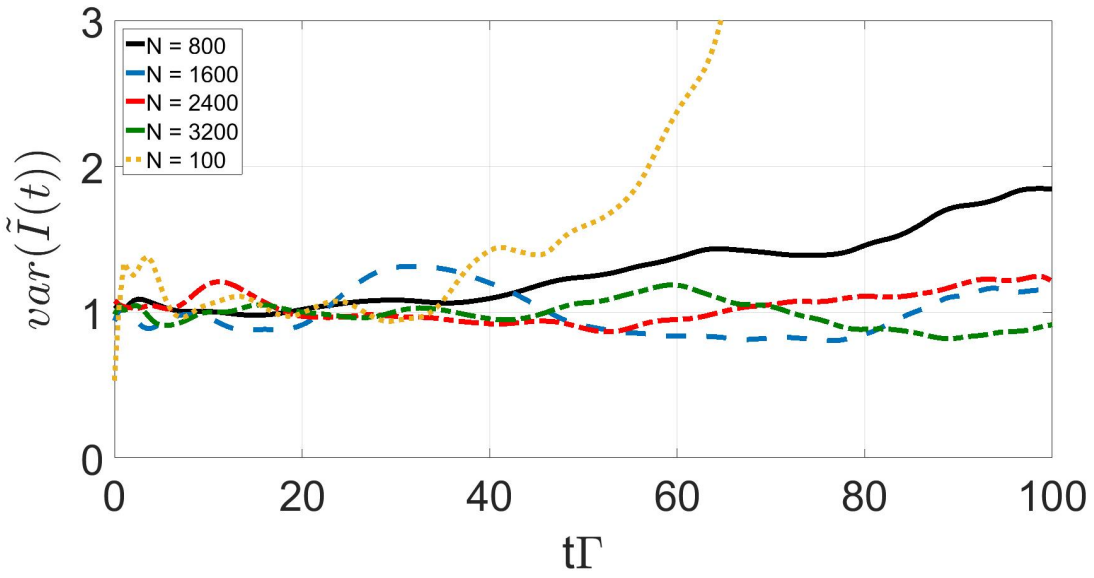

Figure 47 – Variance of the normalized radiated intensity in time. Atoms are distributed in a cylinder of side length L and radius $L/2$, we use a Gaussian laser of waist $W_0 = L/4$ and detuning $\delta = 0$. The resonant optical thickness is $b_0 = 10$, and the density is $\rho\lambda^3 = 4$. The intensity is computed in direction $r_o = 250L$, $\phi = 0$ and $\theta = \pi/5$. There is no diagonal disorder $W = 0$.

Source: By the author

14.2 Intensity fluctuations

We use a similar geometry, a uniform cube distribution, and the same parameters, as in Fig.45 and we show in Fig.48, the variance of the normalized radiated intensity at time $t = 30\Gamma^{-1}$ as a function of W/b_0. It is a really interesting result as it exhibits a transition between a *weak diagonal disorder* regime $W/b_0 \ll 0.2$ and a *strong diagonal disorder* regime, $W/b_0 \gg 0.2$. Moreover, the value of $W/b_0 \approx 0.2$, where this transition appears, is comparable with the one in Fig.45. Hence, we observe a similar transition into the variance of the radiated intensity as the one observed in the PR in.[20]

14.3 Scaling of the critical diagonal disorder

In the previous section we showed a transition, at a critical diagonal disorder $W/b_0 \approx 0.2$, in the variance of the radiated intensity computed at time $t = 30\Gamma^{-1}$; see in Fig.48. In this section, we generalize this study for different times. We plot, in Fig.49, the critical diagonal disorder at the transition as a function of the inverse time when the radiated intensity statistics are performed. The critical diagonal disorder at the transition is computed as follows: we use the same parameters as for every point of Fig.48 and, we plot $var(\tilde{I}(t))$ and we record the time t where the curve $var(\tilde{I}(t))$ crosses 1.5. We exclude in Fig.49 the extreme values. Another procedure would have consisted in extracting the

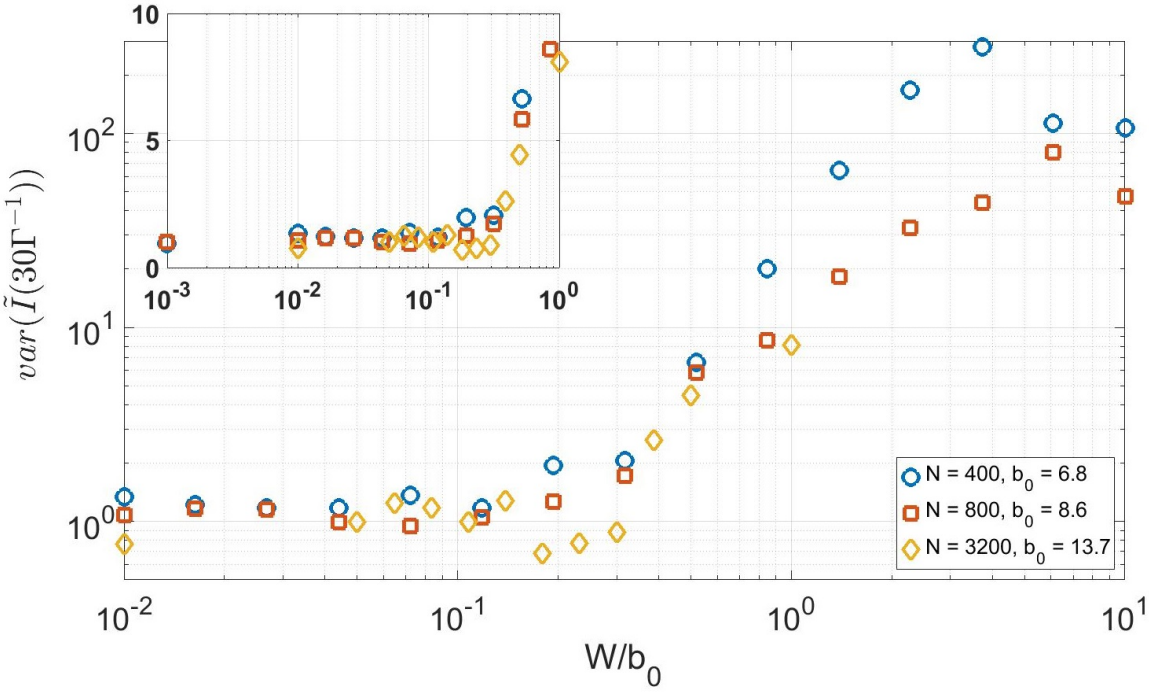

Figure 48 – Variance of the normalized radiated intensity at time $t = 30\Gamma^{-1}$ as a function of the diagonal disorder divided by resonant optical thickness. Atoms are uniformly distributed in a cube of side length L. Intensity is computed over 50 realizations in direction $\mathbf{r_o}$ where $r_o = 250L$, $\theta = 75°$ and $\phi = 0$. We use a Gaussian laser of waist $W_0 = L/4$ and detuning $\delta = 0$.

Source: By the author

critical diagonal disorder from Fig.48 where the variance diverges from one and so forth at different times.

The critical decay rate Γ_{cr} in Fig.46 distinguishes between the non-localized mode ($\gamma_n > \Gamma_{cr}$) and the localized modes ($\gamma_n < \Gamma_{cr}$). Similarly, computing the radiated intensity at time t allows selecting the eigenmodes n with a decay rate γ_n that satisfies $\Gamma\gamma_n t < 3$, whereas the modes with a decay rate $\Gamma\gamma_n t > 3$ have already decayed, as we have discussed previously. It is another way to select the modes according to their decay rate. Hence, we can draw a parallel between the normalized decay rate Γ_{cr} in Fig.46 and the normalized inverse time $1/(t\Gamma)$ where the radiated intensity statistics analysis is performed. We see in Fig.49 that the linear scaling of W/b_0 with $1/(t\Gamma)$ is recovered. However, the slopes of the linear scalings are different. This difference might be due to the procedure we have used to extract the critical diagonal disorder. The linear scaling of Fig.49 is the second confirmation that the transition observed in Fig.48 is consistent with the results of.[20]

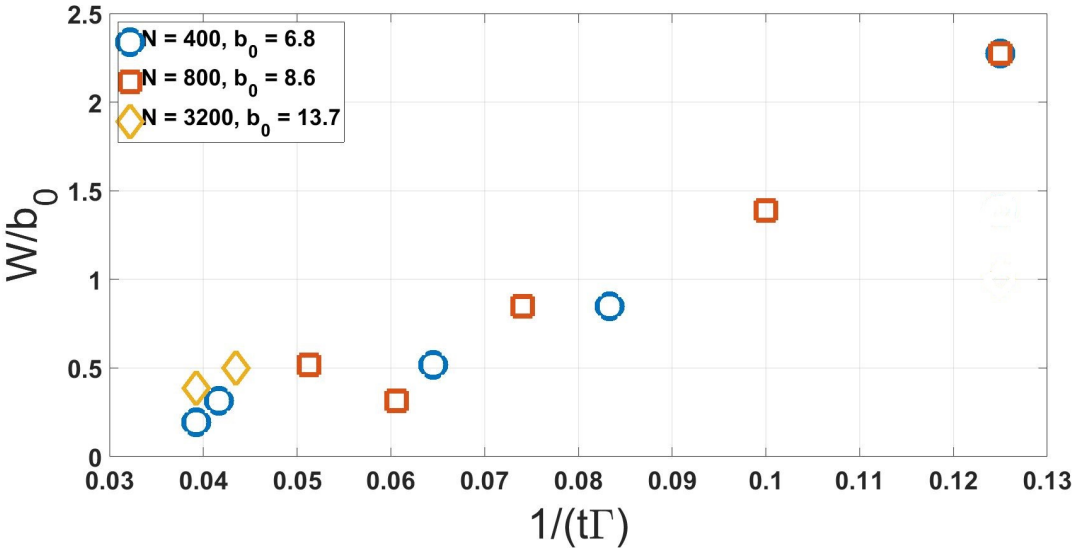

Figure 49 – The system is the same as in Fig.48. t is the time when $var(\tilde{I}(t))$ crosses 1.5.

Source: By the author

15 CONCLUSION

In this part, we have used the diagonal disorder as a way to reach a localized regime. We studied the variance of the radiated intensity in time in order to exhibit a transition between a low diagonal disorder to a strong diagonal disorder regime. Indeed, we have shown that the intensity fluctuations exhibit a phase transition. This transition has been observed in the variance of the long lifetime decay of the intensity where only long lifetime modes remain. We showed that this transition depends on the quantity W/b_0. We also showed that the diagonal disorder at the transition linearly scales with the inverse time when the intensity statistics are performed. It means that there is a linear dependence between the diagonal disorder needed to reach the localized regime and the decay rate of the localized modes. Those two results are consistent with a recent publication.[20] Let us put together the three following results: first, we showed in the Part.IV, that the intensity statistics exhibit an AL phase transition, second, we showed in Part.V a phase transition in the variance of the intensity statistics by increasing the diagonal disorder, and finally, the results of Part.V match with the publication.[20] They are strong arguments in favour of the diagonal disorder as a way to observe Anderson localization. Finally, unlike the PR, the intensity fluctuations is an observable that can be experimentally measured.

The diagonal disorder as a way to reach the localized regime has many advantages. The localized regime can be reached without high densities and the diagonal disorder can be introduced by an external speckle field which gives a good control of the strength of the diagonal disorder. However, there are still open questions like the impact of the temperature on the stability of localized modes, the influence of the cloud geometry (we have used a cube), and the distribution of the diagonal disorder (we have considered only a uniform distribution whereas a speckle pattern is Gaussian).

Part VI

General conclusion

This thesis investigated the light-matter interaction in the context of the coupling between a laser and a cloud of two-level cold atoms. In the first part, we addressed the question of the role of the disorder for super- and subradiance.[40] We developed a model that does not contain disorder, based on a mean-field approach, that we compared with the coupled-dipole microscopic model. We showed that the two models contain super- and subradiant modes. In particular, the superradiant decay rate scales with the resonant optical thickness and cooperative effects still exist at large detuning for the two models.[18,35] It shows that subradiance does not require disorder. We also confirmed, with the mean-field model, that the subradiance is related to modes with inhomogeneous phase profile modes whereas the superradiant modes present a relatively homogeneous phase profile.[38]

In the second part of this thesis, we have used the mean-field model to perform a scaling analysis. As expected, we showed that this model does not exhibit a localization transition as it does not include disorder. The presence of subradiance but the absence of localization in the mean-field approach show that subradiance in not automatically associated to localization. It is an important result in the search of Anderson localization of light. Indeed, in the first experiments on localization, the time decay of the intensity was measured and a deviation was observed from the usual diffusion theory, which was interpreted as a localization effect. Moreover, a recent theoretical work[88] made a link between light trapping and the long lifetime decaying slope of the intensity, which can be understood as a subradiance effect rather than a localization one. Hence, the knowledge we now have on subradiant and the fact that it has been recently experimentally observed[18] give a better understanding of the connection between localization and long lifetime modes.

Most recent theoretical work on Anderson localization of light in 3D is based on increasing the density, to increase disorder.[34,40,47,48,66] Even though theoretical works have shown that the Anderson localization phase transition depends on the detuning and the density, they have not exhibited an experimental observable that might be used to observe this transition. In the third part of this thesis, we first showed that the mean transmitted intensity is not a good observable to detect localization, yet the *fluctuations* of the intensity are. We indeed showed that the variance of the intensity presents a transition as the density and the detuning are tuned. We validated that this transition is an AL phase transition by showing that it has the same characteristics as the AL phase transition presented in the recent literature. The transition is present in the variance for a scalar description of the light but not when the vectorial behaviour of light is considered. Yet, applying a strong magnetic field restores the observation of the transition, as expected.[87] Moreover, we extracted a conductance and recovered the scaling law of the conductance with the variance. We showed that the conductance increases to the infinity in the non-localized regime whereas it decreases to zero in the localized regime. Finally, we showed that the intensity statistics and the computation of the variance can be experimentally obtained by a measurement of the autocorrelation function.

Those are important results for the localization of light community, especially for experimentalist since it provides an observable that exhibits localization. However, many limitations remain on an experimental point of view. The localized regime is reached for high densities what introduces experimental complications: the system is sensitive to the temperature (which is not considered in our study), the small size of the cloud is difficult to stabilize and the focus of the laser beam inside the medium needs a low power (in particular to avoid nonlinear effects), which generates few scattered photons. From a numerical point of view, the introduction of the temperature in the model makes the simulations much more challenging.

In the final part of this thesis, we have presented another method to reach the localized regime: introducing a diagonal disorder. First, we showed that the diagonal disorder modifies the set of eigenvalues of the coupling matrix by squeezing their decay rate. Like in the previous part, we studied the variance of the radiated intensity statistics in the dilute regime, to search for a transition at large diagonal disorder. The statistics are performed over the atom's positions (off-diagonal disorder) and transition frequency (diagonal disorder). First, we looked at the stationary regime and we did not observe any transition as the steady-state regime is dominated by superradiant modes that are not expected to be localized. Then, we computed the variance of the radiated intensity in time after the cloud been charged for a long time. It allowed us to select the long lifetime modes that are more likely to be localized. We showed a transition in the variance that scales with the diagonal disorder divided by the resonant optical thickness and we found that the diagonal disorder at the transition linearly scales with the inverse time of computation of the intensity. Those results are in agreement with a recent publication.[20]

This work on the diagonal disorder is promising in the search of AL of light. Indeed, experimentally, the diagonal disorder is easier than the density method to implement. The main strong advantage is that we do not need to have high densities to reach the localized regime. Moreover, the diagonal disorder can be well controlled by applying a speckle field, the temperature has a weaker impact than at high densities and we can work with a larger cloud of atoms. There are still several issues to address such as the geometry of the cloud (we have used a cube) and the distribution of the diagonal disorder, we have used a uniform distribution whereas the speckle is Gaussian.

REFERENCES

1 MAIMAN, T. H. Optical and microwave-optical experiments in ruby. *Physical Review Letters*, v. 4, n. 11, p. 564–566, 1960.

2 ARECCHI, F. T.; BERNÉ, A.; BULAMACCHI, P. High-order fluctuations in a single-mode laser field. *Physical Review Letters*, v. 16, n. 1, p. 32–35, 1966.

3 LABEYRIE, G. et al. Observation of coherent backscattering of light by cold atoms. *Journal of Optics B:* quantum and semiclassical optics, v. 2, n. 5, p. 672–685, 2000.

4 CHANDRASEKHAR, S. *Radiative transfer*. New York: Dove, 1960.

5 LANGMUIR, R. V. Scattering of laser light. *Applied Physics Letters*, v. 2, n. 2, p. 29–30, 1963.

6 WOLF, P.-E.; MARET, G. Weak localization and coherent backscattering of photons in disordered media. *Physical Review Letters*, v. 55, p. 2696–2699, 1985.

7 WEISS, P. et al. Subradiance and radiation trapping in cold atoms. *New Journal of Physics*, v. 20, n. 6, p. 063024, 2018.

8 PRASAD, S.; GLAUBER, R. Coherent radiation by a spherical medium of resonant atoms. *Physical Review A*, v. 82, p. 063805, 2010.

9 BACHELARD, R. et al. Resonances in mie scattering by an inhomogeneous atomic cloud. *EPL (Europhysics Letters)*, v. 97, n. 1, p. 14004, 2012.

10 DICKE, R. H. Coherence in spontaneous radiation processes. *Physical Review*, v. 93, n. 1, p. 99–110, 1954.

11 ANDERSON, P. W. Absence of diffusion in certain random lattices. *Physical Review*, v. 109, p. 1492, 1958.

12 BOUGUER, P. Essai d'optique sur la gradation de la lumière. *Journal of the Röntgen Society*, v. 18, n. 71, p. 93–93, 1922.

13 GROSS, M.; HAROCHE, S. Superradiance: an essay on the theory of collective spontaneous emission. *Physics Reports*, v. 93, n. 5, p. 301–396, 1982.

14 HAROCHE, S. Rydberg atoms and radiation. In: PRIOR Y.; BEN-REUVEN, A. R. (Ed.). *Methods of Laser Spectroscopy*. New York: Springer, 1986. p. 25–32.

15 SCULLY, M. O. et al. Directed spontaneous emission from an extended ensemble ofNAtoms: timing is everything. *Physical Review Letters*, v. 96, n. 1, 2006.

16 SVIDZINSKY, A.; CHANG, J.-T. Cooperative spontaneous emission as a many-body eigenvalue problem. *Physical Review A*, v. 77, n. 4, 2008.

17 SVIDZINSKY, A. A.; CHANG, J.-T.; SCULLY, M. O. Dynamical evolution of correlated spontaneous emission of a single photon from a uniformly excited cloud of n atoms. *Physical Review Letters*, v. 100, n. 16, 2008.

18 GUERIN, W.; ARAÚJO, M. O.; KAISER, R. Subradiance in a large cloud of cold atoms. *Physical Review Letters*, v. 116, n. 8, 2016.

19 STÖRZER, M. et al. Observation of the critical regime near anderson localization of light. *Physical Review Letters*, v. 96, n. 6, 2006.

20 CELARDO, G. L.; ANGELI, M.; KAISER, R. *Localization of light in subradiant Dicke states*. 2017. Accessible at: Nov. 8, 2018. Disponível em: <https://arxiv.org/abs/1702.04506>.

21 AKKERMANS, E.; MONTAMBAUX, G. *Mesoscopic physics of electrons and phtons*. Cambridge: University Press, 2007.

22 MIE, G. Beiträge zur optik trüber medien, speziell kolloidaler metallösungen. *Annalen der Physik*, v. 330, n. 3, p. 377–445, 1908.

23 HULST, H. C. van de. *Light scattering by small particles*. New York: John Wiley, 1957.

24 LEHMBERG, R. H. Radiation from an n-atom system. i. general formalism. *Physical Review A*, v. 2, n. 3, p. 883–888, 1970.

25 CASTRO, L. B. D. *Localisation de la lumière et effets coopératifs dans des nuages d'atomes froids*. 2017. Tese (Thesis) — Université de Nice Sophia Antipolis, 2017.

26 BIENAIMÉ, T. *Cooperative effects in cold atom clouds*. 2011. Tese (Thesis) — Université Nice Sophia Antipolis, 2011.

27 LABEYRIE, G. et al. Multiple scattering of light in a resonant medium. *Optics Communications*, v. 243, n. 1-6, p. 157–164, 2004.

28 AKKERMANS, E.; WOLF, P. E.; MAYNARD, R. Coherent backscattering of light by disordered media: analysis of the peak line shape. *Physical Review Letters*, v. 56, n. 14, p. 1471–1474, 1986.

29 GERO, A.; AKKERMANS, E. Superradiance and multiple scattering of photons in atomic gases. *Physical Review A*, v. 75, n. 5, 2007.

30 _____. Effect of superradiance on transport of diffusing photons in cold atomic gases. *Physical Review Letters*, v. 96, n. 9, 2006.

31 MÉZARD, M.; PARISI, G.; ZEE, A. Spectra of euclidean random matrices. *Nuclear Physics B*, v. 559, n. 3, p. 689–701, 1999.

32 ZEE, A. Law of addition in random matrix theory. *Nuclear Physics B*, v. 474, n. 3, p. 726–744, 1996.

33 GRIGERA, T. S. et al. Vibrations in glasses and euclidean random matrix theory. *Journal of Physics:* condensed matter, v. 14, n. 9, p. 2167, 2002.

34 BELLANDO, L. et al. Cooperative effects and disorder: a scaling analysis of the spectrum of the effective atomic hamiltonian. *Physical Review A*, v. 90, n. 6, 2014.

35 ARAÚJO, M. O. et al. Superradiance in a large and dilute cloud of cold atoms in the linear-optics regime. *Physical Review Letters*, v. 117, n. 7, 2016.

36 CHOMAZ, L. et al. Absorption imaging of a quasi-two-dimensional gas: a multiple scattering analysis. *New Journal of Physics*, v. 14, n. 5, p. 055001, 2012.

37 MORICE, O.; CASTIN, Y.; DALIBARD, J. Refractive index of a dilute bose gas. *Physical Review A*, v. 51, n. 5, p. 3896–3901, 1995.

38 ARAÚJO, M. O.; GUERIN, W.; KAISER, R. Decay dynamics in the coupled-dipole model. *Journal of Modern Optics*, v. 65, n. 11, p. 1345–1354, 2017.

39 GUERIN, W.; ROUABAH, M.; KAISER, R. Light interacting with atomic ensembles: collective, cooperative and mesoscopic effects. *Journal of Modern Optics*, p. 1–13, 2016.

40 COTTIER, F.; KAISER, R.; BACHELARD, R. Role of disorder in super- and subradiance of cold atomic clouds. *Physical Review A*, v. 98, n. 1, 2018.

41 COURTEILLE, P. et al. Modification of radiation pressure due to cooperative scattering of light. *The European Physical Journal D*, v. 58, p. 69, 2010.

42 ROUABAH, M. T. *Effets de cohérence en diffusion multiple de la lumière et intrication des états cohérents*. 2015. Tese (Thesis) — Université Nice Sophia Antipolis, 2015.

43 BORN, M.; WOLF, E. *Principles of optics: electromagnetic theory of propagation, interference and diffraction of light*. Cambridge: Cambridge University Press, 1999.

44 BONS, P. et al. Quantum enhancement of the index of refraction in a bose-einstein condensate. *Physical Review Letters*, v. 116, n. 17, 2016.

45 SVIDZINSKY, A. A.; CHANG, J.-T.; SCULLY, M. O. Cooperative spontaneous emission of N atoms: many-body eigenstates, the effect of virtual lamb shift processes, and analogy with radiation of N classical oscillators. *Physical Review A*, v. 81, n. 5, p. 053821, 2010.

46 SCULLY, M.; ZUBAIRY, M. *Quantum optics*. Cambridge: Cambridge University Press, 1997.

47 SKIPETROV, S.; SOKOLOV, I. Absence of anderson localization of light in a random ensemble of point scatterers. *Physical Review Letters*, v. 112, n. 2, 2014.

48 _____. Ioffe-regel criterion of anderson localization in the model of resonant point scatterers. *Physical Review B*, v. 112, n. 2, 2018.

49 SKIPETROV, S. Localization transition for light scattering by cold atoms in an external magnetic field. *Physical Review Letters*, v. 121, n. 9, 2018.

50 MÁXIMO, C. E. et al. Spatial and temporal localization of light in two dimensions. *Physical Review A*, v. 92, n. 6, 2015.

51 LABEYRIE, G. et al. Coherent backscattering of light by cold atoms. *Physical Review Letters*, v. 83, n. 25, p. 5266–5269, 1999.

52 BALIK, S. et al. Strong-field coherent backscattering of light in ultracold atomic 85rb. *Journal of Modern Optics*, v. 52, n. 16, p. 2269–2278, 2005.

53 MISHCHENKO, M. I.; TRAVIS, L. D.; LACIS, A. A. *Multiple scattering of light by particles: radiative transfer and coherent backscattering*. Cambridge: Cambridge University Press, 2006.

54 CHANELIÈRE, T. et al. Saturation-induced coherence loss in coherent backscattering of light. *Physical Review E*, v. 70, n. 3, 2004.

55 YOO, K. M.; TANG, G. C.; ALFANO, R. R. Coherent backscattering of light from biological tissues. *Applied Optics*, v. 29, n. 22, p. 3237, 1990.

56 TOURIN, A. et al. Time-dependent coherent backscattering of acoustic waves. *Physical Review Letters*, v. 79, n. 19, p. 3637–3639, 1997.

57 KUPRIYANOV, D. V. et al. Coherent backscattering of light in atomic systems: application to weak localization in an ensemble of cold alkali-metal atoms. *Physical Review A*, v. 67, n. 1, 2003.

58 _____. Coherent backscattering of light from ultracold and optically dense atomic ensembles. *Laser Physics Letters*, v. 3, n. 5, p. 223–243, 2006.

59 WELLENS, T. et al. Coherent backscattering of light by two atoms in the saturated regime. *Physical Review A*, v. 70, n. 2, 2004.

60 LABEYRIE, G.; KAISER, R.; DELANDE, D. Radiation trapping in a cold atomic gas. *Applied Physics B*, v. 81, n. 7, p. 1001–1008, 2005.

61 BAUDOUIN, Q.; MERCADIER, N.; KAISER, R. Steady-state signatures of radiation trapping by cold multilevel atoms. *Physical Review A*, v. 87, n. 1, 2013.

62 MATSKO, A. B. et al. Radiation trapping in coherent media. *Physical Review Letters*, v. 87, n. 13, 2001.

63 GRADSHTEYN, I.; RYZHIK, I. *Table of integrals, series, and products*. 7. ed. New York: Academic Press, 2007.

64 MARčENKO, V. A.; PASTUR, L. A. Distribution of eigenvalues for some sets of random matrices. *Mathematics of the USSR-Sbornik*, v. 1, n. 4, p. 457, 1967.

65 BIENAIMÉ, T.; PIOVELLA, N.; KAISER, R. Controlled Dicke Subradiance from a large cloud of two-level systems. *Physical Review Letters*, v. 108, n. 12, 2012.

66 SKIPETROV, S. E. Finite-size scaling analysis of localization transition for scalar waves in a three-dimensional ensemble of resonant point scatterers. *Physical Review B*, v. 94, n. 6, 2016.

67 GUERIN, W.; KAISER, R. Population of collective modes in light scattering by many atoms. *Physical Review A*, v. 95, n. 5, 2017.

68 OLIVEIRA, R. A. de et al. Single-photon superradiance in cold atoms. *Physical Review A*, v. 90, n. 2, 2014.

69 ROOF, S. et al. Observation of single-photon superradiance and the cooperative lamb shift in an extended sample of cold atoms. *Physical Review Letters*, v. 117, n. 7, 2016.

70 HULST, H. C. V. D. *Light scattering by small particles*. New York: John Wiley, 1958, v. 84, p. 198–199.

71 JOHN, S. Electromagnetic absorption in a disordered medium near a photon mobility edge. *Physical Review Letters*, v. 53, n. 22, p. 2169–2172, 1984.

72 RIO, R. del et al. What is localization? *Physical Review Letters*, v. 75, n. 1, p. 117–119, 1995.

73 HU, H. et al. Localization of ultrasound in a three-dimensional elastic network. *Nature Physics*, v. 4, n. 12, p. 945–948, 2008.

74 BILLY, J. et al. Direct observation of anderson localization of matter waves in a controlled disorder. *Nature*, v. 453, n. 7197, p. 891–894, 2008.

75 SEMEGHINI, G. et al. Measurement of the mobility edge for 3d anderson localization. *Nature Physics*, v. 11, n. 7, p. 554–559, 2015.

76 CHABANOV, A. A.; STOYTCHEV, M.; GENACK, A. Z. Statistical signatures of photon localization. *Nature*, v. 404, n. 6780, p. 850–853, 2000.

77 GENACK, A. Z.; GARCIA, N. Observation of photon localization in a three-dimensional disordered system. *Physical Review Letters*, v. 66, n. 16, p. 2064–2067, 1991.

78 WIERSMA, D. S. et al. Localization of light in a disordered medium. *Nature*, v. 390, n. 6661, p. 671–673, 1997.

79 SCHUURMANS, F. J. P. et al. Light scattering near the localization transition in macroporous GaP networks. *Physical Review Letters*, v. 83, n. 11, p. 2183–2186, 1999.

80 AEGERTER, C. M.; STÖRZER, M.; MARET, G. Experimental determination of critical exponents in anderson localisation of light. *Europhysics Letters (EPL)*, v. 75, n. 4, p. 562–568, 2006.

81 ALBADA, M. P. van et al. Speed of propagation of classical waves in strongly scattering media. *Physical Review Letters*, v. 66, n. 24, p. 3132–3135, 1991.

82 IOFFE, A. F.; REGEL, A. R. Non-crystalline, amorphous, and liquid electronic semiconductors. *Progress in Semiconductors*, v. 4, p. 237–291, 1960.

83 ABRAHAMS, E. et al. Scaling theory of localization: absence of quantum diffusion in two dimensions. *Physical Review Letters*, v. 42, n. 10, p. 673–676, 1979.

84 EDWARDS, J. T.; THOULESS, D. J. Numerical studies of localization in disordered systems. *Journal of Physics C:* solid state physics, v. 5, n. 8, p. 807, 1972.

85 LICCIARDELLO, D. C.; THOULESS, D. J. Conductivity and mobility edges for two-dimensional disordered systems. *Journal of Physics C:* solid state physics, v. 8, n. 24, p. 4157, 1975.

86 THOULESS, D. J. Maximum metallic resistance in thin wires. *Physical Review Letters*, v. 39, n. 18, p. 1167–1169, 1977.

87 SKIPETROV, S.; SOKOLOV, I. Magnetic-field-driven localization of light in a cold-atom gas. *Physical Review Letters*, v. 114, n. 5, 2015.

88 SKIPETROV, S. E.; SOKOLOV, I. M.; HAVEY, M. D. Control of light trapping in a large atomic system by a static magnetic field. *Physical Review A*, v. 94, n. 1, 2016.

89 NIEUWENHUIZEN, T. M.; ROSSUM, M. C. W. van. Intensity distributions of waves transmitted through a multiple scattering medium. *Physical Review Letters*, v. 74, n. 14, p. 2674–2677, 1995.

90 BOER, J. F. de et al. Probability distribution of multiple scattered light measured in total transmission. *Physical Review Letters*, v. 73, n. 19, p. 2567–2570, 1994.

91 KOGAN, E.; KAVEH, M. Random-matrix-theory approach to the intensity distributions of waves propagating in a random medium. *Physical Review B*, v. 52, n. 6, p. R3813–R3815, 1995.

92 STOYTCHEV, M.; GENACK, A. Z. Measurement of the probability distribution of total transmission in random waveguides. *Physical Review Letters*, v. 79, n. 2, p. 309–312, 1997.

93 _____. Observations of non-rayleigh statistics in the approach to photon localization. *Optics Letters*, v. 24, n. 4, p. 262, 1999.

94 ROSSUM, M. C. W. van; NIEUWENHUIZEN, T. M. Multiple scattering of classical waves: microscopy, mesoscopy, and diffusion. *Reviews of Modern Physics*, v. 71, n. 1, p. 313–371, 1999.

95 RUOSTEKOSKI, J.; JAVANAINEN, J. Quantum field theory of cooperative atom response: low light intensity. *Physical Review A*, v. 55, n. 1, p. 513–526, 1997.

96 SCULLY, M. O. Collective lamb shift in single photon dicke superradiance. *Physical Review Letters*, v. 102, n. 14, 2009.

97 BIDEL, Y. et al. Coherent light transport in a cold strontium cloud. *Physical Review Letters*, v. 88, n. 20, 2002.

98 GOODMAN, J. F. B. et al. Rules in industrial relations theory: a discussion. *Industrial Relations Journal*, v. 6, n. 1, p. 14–30, 1975.

99 GARCIA, N.; GENACK, A. Z. Crossover to strong intensity correlation for microwave radiation in random media. *Physical Review Letters*, v. 63, n. 16, p. 1678–1681, 1989.

100 GARCIA, N. et al. Intensity correlation in waveguides. *Physics Letters A*, v. 176, n. 6, p. 458–461, 1993.

101 SHNERB, N.; KAVEH, M. Non-rayleigh statistics of waves in random systems. *Physical Review B*, v. 43, n. 1, p. 1279–1282, 1991.

102 KOGAN, E. et al. Statistics of waves propagating in a random medium. *Physical Review B*, v. 48, n. 13, p. 9404–9410, 1993.

103 _____. Distribution function of the intensity of optical waves in random systems. *Physica A:* statistical mechanics and its applications, v. 200, n. 1-4, p. 469–475, 1993.

104 GRÉMAUD, B.; WELLENS, T. Speckle instability: coherent effects in nonlinear disordered media. *Physical Review Letters*, v. 104, n. 13, 2010.

105 GOODMAN, J. J. W. *Speckle phenomena in optics:* theory and applications. Greenwood Village: Roberts & Company Publishers, 2006.

106 BERKOVITS, R.; FENG, S. Correlations in coherent multiple scattering. *Physics Reports*, v. 238, n. 3, p. 135–172, 1994.

107 GOODMAN, J. W. *Statistical optics*. New York: Wiley-interscience, 1985.

108 GENACK, A. Z. Optical transmission in disordered media. *Physical Review Letters*, v. 58, n. 20, p. 2043–2046, 1987.

109 ELOY, A. et al. Diffusing-wave spectroscopy of cold atoms in ballistic motion. *Physical Review A*, v. 97, n. 1, 2018.

110 KOGAN, E.; KAVEH, M. Statistics of waves propagating in a random medium. *Foundations of Physics*, v. 26, n. 5, p. 679–690, 1996.

111 SHAPIRO, B. Large intensity fluctuations for wave propagation in random media. *Physical Review Letters*, v. 57, n. 17, p. 2168–2171, 1986.

112 GITTERMAN, M. *Phase transitions*. Singapore: World Scientific, 2013.

113 BIELLA, A. et al. Subradiant hybrid states in the open 3d Anderson-Dicke model. *EPL (Europhysics Letters)*, v. 103, n. 5, p. 57009, 2013.

114 CELARDO, G. et al. Interplay of superradiance and disorder in the anderson model. *Fortschritte der Physik*, v. 61, n. 2-3, p. 250–260, 2012.

115 CELARDO, G. L.; GIUSTERI, G. G.; BORGONOVI, F. Cooperative robustness to static disorder: superradiance and localization in a nanoscale ring to model light-harvesting systems found in nature. *Physical Review B*, v. 90, n. 7, 2014.

116 GIUSTERI, G. G.; MATTIOTTI, F.; CELARDO, G. L. Non-hermitian hamiltonian approach to quantum transport in disordered networks with sinks: validity and effectiveness. *Physical Review B*, v. 91, n. 9, 2015.